National Library of Canada

Acquisitions and Bibliographic Services Branch

395 Wellington Street
Ottawa, Ontario
K1A 0N4

Bibliothèque nationale du Canada

Direction des acquisitions et des services bibliographiques

395, rue Wellington
Ottawa (Ontario)
K1A 0N4

Your file Votre référence

Our file Notre référence

NOTICE

The quality of this microform is heavily dependent upon the quality of the original thesis submitted for microfilming. Every effort has been made to ensure the highest quality of reproduction possible.

If pages are missing, contact the university which granted the degree.

Some pages may have indistinct print especially if the original pages were typed with a poor typewriter ribbon or if the university sent us an inferior photocopy.

Reproduction in full or in part of this microform is governed by the Canadian Copyright Act, R.S.C. 1970, c. C-30, and subsequent amendments.

AVIS

La qualité de cette microforme dépend grandement de la qualité de la thèse soumise au microfilmage. Nous avons tout fait pour assurer une qualité supérieure de reproduction.

S'il manque des pages, veuillez communiquer avec l'université qui a conféré le grade.

La qualité d'impression de certaines pages peut laisser à désirer, surtout si les pages originales ont été dactylographiées à l'aide d'un ruban usé ou si l'université nous a fait parvenir une photocopie de qualité inférieure.

La reproduction, même partielle, de cette microforme est soumise à la Loi canadienne sur le droit d'auteur, SRC 1970, c. C-30, et ses amendements subséquents.

Canada

UNIVERSITY OF ALBERTA

A SIMULATION AND EXPERIMENTAL STUDY OF WATER PROTON RELAXATION IN A WHITE MATTER MODEL

BY

FRANCES ROSE ERNA FENRICH

A thesis submitted to the Faculty of Graduate Studies and Research in partial fulfillment of the requirements for the degree of
MASTER OF SCIENCE.

IN

MEDICAL PHYSICS

DEPARTMENT OF PHYSICS

Edmonton, Alberta
FALL 1992

National Library of Canada
Bibliothèque nationale du Canada

Canadian Theses Service
Service des thèses canadiennes

Ottawa, Canada
K1A 0N4

The author has granted an irrevocable non-exclusive licence allowing the National Library of Canada to reproduce, loan, distribute or sell copies of his/her thesis by any means and in any form or format, making this thesis available to interested persons.

L'auteur a accordé une licence irrévocable et non exclusive permettant à la Bibliothèque nationale du Canada de reproduire, prêter, distribuer ou vendre des copies de sa thèse de quelque manière et sous quelque forme que ce soit pour mettre des exemplaires de cette thèse à la disposition des personnes intéressées.

The author retains ownership of the copyright in his/her thesis. Neither the thesis nor substantial extracts from it may be printed or otherwise reproduced without his/her permission.

L'auteur conserve la propriété du droit d'auteur qui protège sa thèse. Ni la thèse ni des extraits substantiels de celle-ci ne doivent être imprimés ou autrement reproduits sans son autorisation.

ISBN 0-315-77078-3

Canada

UNIVERSITY OF ALBERTA

RELEASE FORM

NAME OF AUTHOR: FRANCES ROSE ERNA FENRICH

TITLE OF THESIS: A SIMULATION AND EXPERIMENTAL STUDY OF WATER PROTON RELAXATION IN A WHITE MATTER MODEL

DEGREE: MASTER OF SCIENCE

YEAR THIS DEGREE GRANTED: 1992

Permission is hereby granted to the University of Alberta Library to reproduce single copies of this thesis and to lend or sell such copies for private, scholarly or scientific research purposes only.

The author reserves all other publication and other rights in association with the copyright in the thesis, and except as hereinbefore provided neither the thesis nor any substantial portion thereof may be printed or otherwise reproduced in any material form whatever without the author's prior written permission.

Frances Fenrich

Box 424
Choiceland, Sask.
S0J 0M0

Date: Sept. 16, 1992

UNIVERSITY OF ALBERTA

FACULTY OF GRADUATE STUDIES AND RESEARCH

The undersigned certify that they have read, and recommend to the Faculty of Graduate Studies and Research for acceptance, a thesis entitled A SIMULATION AND EXPERIMENTAL STUDY OF WATER PROTON RELAXATION IN A WHITE MATTER MODEL submitted by FRANCES ROSE ERNA FENRICH in partial fulfillment of the requirements of the degree of MASTER OF SCIENCE.

Dr. P. S. Allen (Co-Supervisor)

Dr. D. G. Hughes (Co-Supervisor)

Dr. R. E. Snyder

Dr. S. F. P. Man

Dr. J. A. Kernahan

Date: Sept. 15, 1992

To my parents, for all their love and support.

ABSTRACT

The heterogeneity of biological tissue is believed to give rise to multiple transverse relaxation time components for water protons as measured by nuclear magnetic resonance. If multiple transverse relaxation time components could be identified in-vivo, the specificity of diagnostic nuclear magnetic resonance imaging would be vastly improved, especially in demyelinating diseases afflicting white matter. However, in-vivo there are numerous experimental limitations, such as restrictions in the signal-to-noise ratio, the number of data points required, and the range of the time domain acquisition window. To evaluate the effects of such limitations upon a particular linear inverse theory technique to recover continuous relaxation time distributions, a simulation study has been done. Signal-to-noise ratio and, to a smaller extent, the minimum time of the data acquisition window proved to be the greatest factors limiting the inverse algorithm's ability to distinguish multiple continuous relaxation time components. To determine the potential of multi-component transverse relaxation in in-vivo white matter, an in-vitro transverse relaxation time study of water protons in a simple white matter tissue model has been carried out. The model consisted of myelinated and nonmyelinated cranial nerves of the spotted garfish (Lepisosteus oculatus). The transverse relaxation time distributions of the myelinated nerves showed an extra short time component which was not present in the nonmyelinated nerve. This short time component has been attributed to water protons in the myelin sheath. Comparison with electron microscopy of the nerves support this assignment as well as the assignment of intracellular and extracellular water to the two long time components present in the transverse relaxation time distributions of each nerve. Viability of the nerves, proven by action potential measurements and electron microscopy lends credence to their use as a white matter model. Sensitivity of the transverse relaxation time distributions to the physiological state of the nerves was observed providing promise for the multi-component transverse relaxation analysis in white matter in-vivo.

ACKNOWLEDGEMENT

I would like to thank Dr. Peter S. Allen for his supervision during the course of my project. Besides providing me with the opportunity to work in his laboratory, he has helped me to gain a good understanding of NMR. When it came to writing this thesis, his advice and comments were invaluable. Thanks are extended as well to the other members of my supervisory committee, Dr. Gwyn Hughes, Dr. Rick Snyder, and Dr. Paul Man, for their participation throughout the project, and to Dr. Tony Kernahan for being a part of my examining committee.

I am especially grateful to my predecessor, Dr. Ravi Menon, not only for his countless hours of instruction on the "nuts and bolts" of NMR, but more importantly for his friendship.

There are numerous people who deserve recognition for their contributions to this work: Elizabeth Mathew for her initial help with the garfish; Rosie Vishram for her skill in sample preparation, fixation, and electron microscopy; Dan Doran and Karim Damji for keeping the Bruker system alive and well; Ivy Ho for maintaining the computing facilities; and Narc Ouellette for developing the action potential system (a portion of which was kindly donated by Dr. Bill Dryden of Pharmacology). These people as well as others in the NMR group and Department of Applied Sciences in Medicine have made my time here very educational and enjoyable.

I would also like to acknowledge Dr. Ming Chen of the Surgical and Medical Research Institute for the use of his electron microscope, and Margot Szalay of the Department of Anatomy and Cell Biology for completing a portion of the excellent electron microscopic work found in this thesis.

Thanks are extended to the Natural Sciences and Engineering Research Council of Canada and The Alberta Heritage Foundation for Medical Research for providing financial support throughout the course of my studies.

Finally, I must give thanks to my close friend, Christian, for all his support ....not to mention his skill at garfish dissection which is second only to mine!

TABLE OF CONTENTS

Chapter				Page
1	Introduction			
	1.1	Introduction to Thesis		1
	1.2	White Matter of the Brain		3
		1.2.1	General Morphology	3
		1.2.2	Axons	4
		1.2.3	Myelin	5
		1.2.4	Glia	6
		1.2.5	Extracellular Space	6
		1.2.6	Nerve Cords of the Peripheral and Central Nervous Systems	7
	1.3	Nuclear Magnetic Resonance Theory		9
		1.3.1	Introduction to NMR	9
		1.3.2	The Macroscopic Magnetization	11
		1.3.3	Two-Spin Relaxation	14
			1.3.3.1 The Hamiltonian and its Eigenstates	14
			1.3.3.2 Equations of Motion of the Macroscopic Magnetization	16
			1.3.3.3 The Dipole-Diplole Interaction	17
		1.3.4	Exchange Between Phases	22
		1.3.5	Transverse Relaxation in Biological Systems	24
	1.4	References and Selected Bibliography		39
2	A Simulation Evaluation of a Linear Inverse Technique for Determining Continuous Relaxation Time Distributions			
	2.1	Introduction		42
	2.2	Theory		47
	2.3	Method		54
		2.3.1	Simulation to Test the Resolving Power of T2LIN	56
		2.3.2	Simulation to Test the Effects of Decreasing the Density of Data Points within a Fixed Time Window	57
		2.3.3	Simulation to Test the Effects upon Fixed Relaxation Time Components of Restricting the Time Window of Data Acquisition	58

2.4 Results and Discussion 59
2.4.1 Simulation to Test Resolving Power of T2LIN 59
2.4.2 Simulation to Test the Effects of Decreasing the Density of Data Points within a Fixed Time Window 61
2.4.3 Simulation to Test the Effects upon Fixed Relaxation Time Components of Restricting the Time Window of Data Acquisition 62
2.5 Conclusion 64
2.6 References and Selected Bibliography 80
3 Water Proton Transverse Relaxation Time Analysis of Myelinated and Nonmyelinated Nerves: A Simple White Matter Model
3.1 Introduction 82
3.2 Gross Anatomy and Microstructure of Garfish Cranial Nerves 85
3.2.1 Olfactory Nerve 85
3.2.2 Trigeminal Nerve 86
3.2.3 Optic Nerve 87
3.3 Water Compartments in the Nerves 88
3.4 Experimental 91
3.4.1 Excision of Nerves 91
3.4.2 Action Potential Measurements on the Nerves 92
3.4.3 NMR Transverse Relaxation Measurements 93
3.4.4 Electron and Optical Microscopy of Nerves 94
3.5 Data analysis 94
3.5.1 Analysis of Transverse Relaxation Measurements 94
3.5.2 Analysis of Electron and Optical Microscopy of Nerves 96
3.6 Results 97
3.7 Discussion 98
3.7.1 Viability of Excised Nerves 98
3.7.1.1 Action Potential Study 98
3.7.1.2 Electron Microscopy 99
3.7.2 Transverse Relaxation in Freshly Excised Nerves 101
3.7.3 Transverse Relaxation of Outer Connective sheath of Optic Nerve 103
3.7.4 Time Dependent Measurements 104
3.8 Conclusion 108

3.9 References and Selected Bibliography 149

4 Conclusion

4.1 Discussion and Conclusions 151

4.2 References and Selected Bibliography 155

LIST OF TABLES

Table		Page
3.1	Volume fractions of water in various types of nerve tissue found in the garfish cranial nerves	110
3.2(a)	Water populations of various anatomical compartments of the olfactory nerve	111
3.2(b)	Water populations of various anatomical compartments of the trigeminal nerve	112
3.2(c)	Water populations of various anatomical compartments of the optic nerve	113
3.3(a)	Summary of populations and relaxation times in 10 freshly excised olfactory nerves	114
3.3(b)	Summary of populations and relaxation times in 12 freshly excised trigeminal nerves	115
3.3(c)	Summary of populations and relaxation times in 6 freshly excised optic nerves	116
3.4	Comparison of NMR populations with those derived from electron and optical microscopy cross-sections	117

LIST OF FIGURES

Figure		Page
1.1	Simplistic diagram of white and grey matter	28
1.2	Fluid mosaic model of membranes	29
1.3	Basic structure of myelin	30
1.4	Nuclear magnetic moment in static magnetic field	31
1.5	Zeeman energy levels for spin 1/2 nuclei	32
1.6	Vector summation of magnetic fields in	
	a) laboratory frame	33
	b) rotating frame	33
1.7	Interaction of equilibrium magnetization with effective magnetic field in rotating frame of reference	34
1.8	Definition of transition probabilities per unit time between the energy eigenstates of the two-spin system	35
1.9	Definition of transition probabilities per unit time between the eigenstates relevant to transverse relaxation in a two-spin system	36
1.10	Magnetic potential due to a magnetic dipole represented by two fictitious magnetic monopoles	37
1.11	Carr-Purcell-Meiboom-Gill spin-echo sequence	38
2.1	Frequency distribution of the chi-square statistic	66
2.2	Simulated continuous relaxation time distribution	67
2.3	Magnetization decay data set from simulated relaxation time distribution	68
2.4	Typical partially resolved relaxation time spectrum defining resolution	69
2.5	The resolution of two closely spaced components versus component separation and signal-to-noise ratio	70
2.6	T2LIN spectra at a signal-to-noise ratio of 1000 as relative peak separation is increased	71
2.7	T2LIN spectra corresponding to fixed relative peak separations as signal-to-noise ratio is varied through the transition region	72
2.8	Comparison of threshold signal-to-noise ratio versus relative peak separation as determined by three different groups	73
2.9	Variations in T2LIN spectra caused by changing the representations	74

	of the noise	
2.10	a) Resolution, b) precision , and c) accuracy of peak relaxation times versus the number of data points	75
2.11	Resolution versus the number of data points	76
2.12(a)	Precision of a single relaxation time component at various signal-to-noise ratio as the upper boundary of the data acquisition window is brought into close proximity with the relaxation time of that component	77
2.12(b)	Precision of a single relaxation time component at various signal-to-noise ratio as the lower boundary of the data acquisition window is brought into close proximity with the relaxation time of that component	78
2.13	Examples of degeneration of output components brought about by the proximity of	
	a) the lower boundary of the data window	79
	b) the upper boundary of the data window	79
3.1	Spotted garfish	118
3.2(a)	Light microscopic section of olfactory nerve	119
3.2(b)	Olfactory nerve EM	120
3.2(c)	Olfactory nerve EM	121
3.3(a)	Light microscopic section of trigeminal nerve	122
3.3(b)	EM of trigeminal nerve	123
3.4(a)	Light microscopic section of optic nerve	124
3.4(b)	Outer and inner connective tissue sheath of the optic nerve	125
3.4(c)	Connective tissue channel of the optic nerve	126
3.4(d)	Axon field of optic nerve	127
3.5	Bloch diagram of biphasic stimulating and recording electrode system used for measuring action potentials in nerve	128
3.6	Transverse magnetization decay from a typical T_2 experiment	129
3.7	Sample T2LIN spectra plotted	
	a) as a line graph on a log scale	130
	b) as a line graph on a linear scale	130
	c) as a bar graph on a log scale	130
3.8	Action potential voltage measurements for the	

	a) olfactory at 3 hours	131
	b) olfactory at 11 hours	131
	c) trigeminal at 3 hours	131
	c) trigeminal at 30 hours	131
3.9(a)	EM of olfactory nerve at 1 hour post excision	132
3.9(b)	EM of trigeminal nerve at 2 hour post excision	133
3.9(c)	EM of optic nerve at 2 hour post excision	134
3.10(a)	EM of olfactory nerve at 8 hour post excision	135
3.10(b)	EM of trigeminal nerve at 8 hour post excision	136
3.10(c)	EM of optic nerve at 8 hour post excision	137
3.11(a)	Typical olfactory nerve T_2 spectrum	138
3.11(b)	Typical trigeminal nerve T_2 spectrum	139
3.11(c)	Typical optic nerve T_2 spectrum	140
3.12	T_2 spectrum of optic nerve sheath	141
3.13(a)	Time variation of the olfactory nerve T_2 spectra over a period of 3 days	142
3.13(b)	Olfactory nerve T_2 component populations versus time	143
3.14(a)	Time variation of the trigeminal nerve T_2 spectra over a period of 13 days	144
3.14(b)	Trigeminal nerve T_2 component populations versus time	145
3.15(a)	Time variation of the optic nerve T_2 spectra over a period of 7 days	146
3.15(b)	Optic nerve T_2 component populations versus time	147
3.16	Variation of buffer solution T_2 as a function of time from excision for all nerve types	148

LIST OF SYMBOLS AND ABBREVIATIONS

A	kernel of integral defining multiexponential magnetization decay
A/B	ratio of component amplitudes in Kroeker and Henkelman's simulation test
A_k	function of spin operators
b	magnetic field of single dipole
B	magnetic field
B_{eff}	effective magnetic field
B_{loc}	local magnetic field
B_o	static magnetic field
B_1	rf magnetic field
CNS	central nervous system
CONTIN	linear inverse method of Provencher
CPMG	Carr-Purcell-Meiboom-Gill pulse sequence
D	diffusion constant (Chapter 3)
	dip height between unresolved components (Chapter 2)
E	energy
EM	electron microscopy
E_2	least maximum absolute error in Brown's formalism
EAE	experimental allergic encephalomyelitis
F	ratio of relaxation times
F_k	function of spatial coordintes
$F(\chi^2)$	frequency distribution of chi-squared
FWHM	full width at half maximum
G	magnetic field gradient
G_k	correlation function
$\mathcal{H}$	Hamiltonian
$\mathcal{H}_D$	dipolar Hamiltonian
$\mathbf{H}$	constraint matrix
H_{avg}	average of peak heights
$\hbar$	Planck's constant divided by 2π
I	spin quantum number
$\mathbf{I}$	spin angular momentum operator

I_z, I_y, I_x	spin operators
I_+	raising operator for spin states
J_k	spectral density functions
k	Boltzmann's constant
LMAE	least maximum absolute error in Brown's formalism
m	magnetic quantum number
M	net magnetization
MRI	magnetic resonance imaging
MS	multiple sclerosis
M_o	equilibrium magnetization
M_x, M_y	transverse magnetization components
M_z	longitudinal magnetization
NMR	nuclear magnetic resonance
N	number of spins (Chapter.1)
	number of data points (Chapter. 2)
N_{++}, N_{+-}	
N_{-+}, N_{--}	occupancies of energy eigenstates
N_{aa}, N_{ab}	
N_{ba}, N_{bb}	occupancies of transverse eigenstates
NNLS	non-negative least squares algorithm of Lawson and Hanson
P	precision
p_i	water population in compartment i
PNS	peripheral nervous system
r	radial distance
rf	radio frequency
$R_i^{\pm}$	observed relaxation rates in Zimmerman and Brittin model
R_1	longitudinal relaxation rate
R_2	transverse relaxation rate
S	relative peak separation
S(T)	Fractional amplitudes of the magnetization decay relaxing with time constant T
S_j	discrete amplitudes in the spectrum of relaxation times
SNR	signal-to-noise ratio
T	absolute temperature

T_1	longitudinal relaxation time
T_2	transverse relaxation time
T_2^*	time constant characterizing the decay of an FID in an inhomogeneous static magnetic field
$T_{1\rho}$	longitudinal relaxation time in the rotating frame
T_g	grid points at which simulated T_2 spectra are defined
T_A, T_B, T_C	Mean relaxation times of simulated Gaussian relaxation time components
t_N	maximum time in the time domain data window
t_o	minimum time in the time domain data window
τ_c	correlation time
τ_i	lifetime of water molecule in compartment i
2τ	echo time in CPMG sequence
U_i, U_i'	transition probabilities per unit time between transverse eigenstates
W_i, W_i'	transition probabilities per unit time between energy eigenstates
ω	angular frequency
ω_o	Larmor frequency
μ_o	permeability of free space
μ	regularizer
ϕ	magnetic potential
θ	polar angle
ψ	azimuthal angle
Φ_i	observed magnetization in Zimmerman and Brittin model
$\lambda^{\pm}$	observed population in Zimmerman and Brittin model
γ	gyromagnetic ratio
χ_o	magnetic susceptibility
χ^2	chi-squared misfit
σ_i	standard deviation of the noise associated with the i^{th} data point
σ_n	standard deviation of the noise
σ^2	rigid lattice constant
σ_l	standard deviation of l^{th} Gaussian component in simulated T_2 distribution
Γ	gamma function

Chapter 1

Introduction

1.1 Introduction to the Thesis

Nuclear magnetic resonance, NMR, was discovered and developed by physicists and chemists in their search for a complete understanding of the nuclear system. The NMR phenomenon is a result of the magnetic interaction between one of various magnetic nuclei, such as ^{1}H, ^{13}C or ^{31}P, and a set of applied magnetic fields. It is the large abundance of ^{1}H, in the form of water protons, in the human body which make NMR such such a powerful tool in diagnostic medicine. Other nuclei are also detectable in-vivo but the water proton is the most common. NMR allows clinicians to probe the human body non-invasively for pathologies which are difficult or impossible to detect by other conventional methods. Imaging is the most common clinical application of NMR. The various kinds of tissue contrast achievable in images are based upon the relaxation characteristics of the water protons in the tissue. Unfortunately relaxation mechanisms in biological tissue are not fully understood. Thus, in the past, the majority of NMR imaging studies characterize normal and pathological tissue by single relaxation times (1, 2) which are not unique to any particular pathology. This limits the diagnostic capabilities of the NMR image. A potential improvement to the diagnostic capability of NMR may lie in the extraction of multi-component relaxation distributions.

Biological tissue is a heterogeneous system consisting of numerous spatially distinct anatomical compartments, each having a unique relationship between the NMR visible water protons and their macromolecular environment. Relaxation theory, which will be discussed later in this chapter, indicates that such a system should be characterized by multiple relaxation components. Previous NMR relaxation time studies of biological tissues in-vitro (3-6) have demonstrated multiple component transverse relaxation where the longitudinal relaxation shows only a broad unimodal distribution. The ability to distinguish multiple relaxation components in-vivo would improve diagnostic capabilities immensely. Different anatomical compartments, such as intracellular and extracellular spaces, could then be characterized by individual NMR

relaxation times and populations. In the course of disease these times and populations would vary indicating the type of pathology.

White matter of the human brain is plagued by numerous pathologies including edema and demyelinating diseases such as multiple sclerosis (MS). These diseases have a profound effect upon the function of the human body sometimes causing death. Therefore it is important to diagnose these diseases quickly and correctly. Our hypothesis is that multi-component NMR relaxation techniques will eventually provide improved diagnostic specificity in white matter disease. Initial attempts at utilizing multi-component relaxation in-vivo in experimental animal models of edema have shown inconsistent results. One group (7) observed multi-component transverse relaxation in both normal and edematous white matter, another (8) found longitudinal and transverse relaxation monoexponential in normal white matter but biexponential in edematous regions, and yet another (9) observed only biexponentiality for transverse relaxation in the edematous white matter. A recent in-vivo study (10) of multi-component transverse relaxation in normal and MS patients has shown biexponentiality in both the normal and diseased white matter, with a decrease in amplitude of the short time component in the MS lesions. This study is promising for the use of multi-component transverse relaxation in the determination of myelin content in-vivo.

In going from the in-vitro to the in-vivo situation there are many obstacles to overcome, the most difficult and unavoidable one being the reduction in SNR achievable. For example, SNR is reduced by the noise associated with eddy currents induced in the body tissue as well as the large displacement of the localized area from the excitation and receiver coils. Limitations in SNR, as well as other data acquisition parameters, affect the ability to derive multi-component relaxation data. In order to determine the full potential of this NMR relaxation technique in-vivo, it is necessary to determine the extent to which in-vivo limitations restrict the multi-component relaxation analysis. Therefore, Chapter 2 of this thesis is devoted to a simulation study of the effects of the in-vivo limitations upon the linear inverse technique (11) used to determine the continuous relaxation time distributions.

Furthermore, to evaluate the promise of multi-component transverse relaxation in in-vivo white matter, a better understanding of transverse relaxation mechanisms in this tissue type is required. In Chapter 3 then, we use a white matter tissue model, namely excised cranial nerves of the spotted garfish, to establish the multi-component transverse relaxation characteristics of white matter. Our confidence in the resulting NMR transverse relaxation time distributions is based upon the simulation results of Chapter

2. Identification of specific anatomical compartments with NMR transverse relaxation components is made through comparisons with anatomical water populations determined from electron and optical microscopy as well as comparisons between the NMR results of the various nerves.

The concluding chapter, Chapter 4, of this thesis, ties together and summarizes the results of Chapters 2 and 3. The future potential of multi-component NMR relaxation in-vivo is also discussed.

Since this thesis is concerned with transverse relaxation in a white matter model, the remainder of this introduction chapter includes a basic description of white matter tissue and nerves of the peripheral and central nervous system, followed by a discussion of NMR relaxation theory.

1.2 White Matter of the Brain

1.2.1 General Morphology

The primary function of the nervous system is to transmit and receive information via electrical nerve impulses or action potentials. Thus the neurons are specialized for this transmission process. Approximately 75% (or 1.12 billion) of all neurons in the human body are concentrated in the outermost layer of the cerebral cortex of the brain. This dense layer of nerve cell bodies is referred to as grey matter because of its dark appearance. Each neuron has extending from it two types of cytoplasmic processes, dendrites and an axon. The numerous short dendrites provide the receptive surface area of the nerve cell, while the single axon, which is much longer and thinner than the dendrites, conducts impulses away from the cell body. The axons of most nerve cells are ensheathed by numerous layers of cellular membrane wrapped in a spiral fashion about the axon. The function of this wrapping or myelin sheath as it is called, is to increase the speed of transmission of the nerve impulses through its electrical insulation effect. In myelinated nerve, the conduction velocity of an action potential is directly proportional to the axon diameter, D, whereas in nonmyelinated nerve it is proportional to $\sqrt{D}$. Thus the inner portion of the brain is composed of the numerous tracts of myelinated axons, ~2 μm in diameter, extending from the nerve cell bodies of the grey matter. The large proportion of myelin within this central tissue lends it a pale color and therefore it is appropriately called white matter. In addition to

myelinated axons, white matter also contains numerous supportive glial cells and some extracellular space. Fig. 1.1 is a simplistic diagram of the white matter system. The following is a brief description of the major constituents of white matter. For more detail we defer to the various textbooks on the subject (12-15).

1.2.2 Axons

Approximately 40% of white matter tissue water is contained in the intracellular cytoplasm (axoplasm) of the axons. Therefore, the axons will provide a major contribution to the overall water proton NMR relaxation characteristics of white matter tissue. In order to gain insight into the form of the contribution that axonal water will make, knowledge of the internal structure of the axons is required.

The major structural constituents of the axoplasm are neurofilaments and microtubules which are fibrous protein structures running parallel to the length of the axon. Microtubules which are ~25 nm in diameter are more prominent in smaller axons whereas neurofilaments, ~10 nm diameter, are most abundant in the larger axons. The neurofilaments and microtubules are interconnected by thin filamentous structures creating a longitudinally oriented cytoskeletal backbone for the axon. These cytoskeletal components are involved in the maintenance of cell shape and axonal transport. Also present in the axoplasm are mitochondria, endoplasmic reticulum and multi-vesicular bodies. The complex cytoskeleton and the numerous membranous systems such as the mitochondria and endoplasmic reticulum provide for a large, slow moving macromolecular environment for the axon's water protons to adhere to. This is very important when considering the transverse relaxation times since transverse relaxation is enhanced by slow motions.

The axon is bounded by a cellular membrane, called the axolemma, which is a typical plasma membrane characteristic of all cells. The structure of a plasma membrane is shown in Fig. 1.2. It is basically a phospholipid bilayer with embedded proteins. The protein composition varies along the surface of the membrane as well as between different cell types. Each phospholipid molecule consists of a hydrophilic phosphate head group attached to two hydrophobic fatty acid chains. The hydrophilic ends of the molecules face the watery environment external and internal to the cell while the fatty acid chains meet to form the hydrophobic interior of the bilayer. Each half of the bilayer constitutes a leaflet. The many different associated proteins embed their

hydrophobic portions within the hydrophobic interior of the membrane. Some of these integral proteins extend completely through the membrane. Other proteins do not integrate with the membrane but remain on the surface. These are the peripheral proteins. The various proteins serve many different functions. In addition to providing structure, they function as active and passive channels for ion transport. They may also function as neurotransmitter and hormone receptors as well as act as enzymes catalyzing reactions at the membrane surface. Some of the hydrophilic protein and lipid head groups have attached carbohydrates and are therefore referred to as glycoproteins and glycolipids. Because the lipids and proteins of membrane systems are free to move laterally, this model is often termed the fluid mosaic model of membranes. The presence of cholesterol droplets within the bilayer restricts the fluidity of the membrane. A single plasma membrane provides a small diffusional barrier to axonal water. However, the numerous layers of cellular membrane present in the myelin sheath provide a very large barrier to diffusion. The diffusive exchange of axonal water with its surroundings is another important consideration for relaxation of the water protons.

1.2.3 Myelin

Myelin is the insulating layer around axons formed by concentric wrappings of flattened cytoplasmic processes extending from an oligodendrocyte in the CNS or from a Schwann cell in the peripheral nervous system (PNS). The basic structure of myelin is shown in Fig. 1.3. As the flattened cytoplasmic process wraps around the axon, the inner membrane surfaces of the process fuse together squeezing out the cytoplasm, forming what is called the major dense line. The close apposition of the outer membrane leaflets, creates the less dense intraperiod line. The radial periodicity of myelin is ~16 nm in the CNS and ~18 nm in the PNS.

The myelin sheath created by a single cytoplasmic process extends ~1 mm along the length of an axon and is referred to as an internode. Numerous successive internodes exist along the length of a myelinated axon and are separated by the nodes of Ranvier. These nodes, which are ~1 μm long, are the locations of membrane depolarization during an action potential. Thus the nerve impulse jumps from node to node rather than traversing the entire axonal surface. This greatly increases the speed of conduction of the action potential.

Since myelin is a series of cellular membranes sandwiched together, its basic structure and composition is identical to that defined in the fluid mosaic model of cellular membranes (Fig. 1.2). Its major constituents then, are lipid and protein, which make up 70% and 30% of the dry weight of myelin, respectively (14). Myelin also has a substantial proportion of water, ~40% by volume determined by x-ray diffraction studies(14), which makes up ~15% of the total water in white matter (16). Thus myelin should also make a significant contribution to the water proton NMR signal.

1.2.4 Glia

Glial cells provide a complex, three-dimensional supporting network of cells in which the neurons are embedded. There are three types of glial cells: astrocytes, oligodendrocytes and microglia. The cytoplasmic processes of astrocytes fill most of the space between the capillaries and neurons. There are two types of astrocytes: protoplasmic and fibrous with the fibrous astrocytes containing more fibrils of protein. Protoplasmic astrocytes are found in grey matter whereas the fibrous type are present in white matter. Astrocytes can be identified by their cytoplasm which is less dense than other glial cell types. Oligodendrocytes are identified by their electron dense cytoplasm and round dense nucleus. These cells play the important role of myelinating the nerve axons of the central nervous system (CNS). Numerous cytoplasmic processes from a single oligodendrocyte contribute myelin to several axons. Microglia are wandering macrophages which migrate to the CNS along the blood vessels. They have a dense cytoplasm as well but few cytoplasmic processes. All three types of glial cells contain the typical cellular organelles such as endoplasmic reticulum, golgi apparatus, mitochondria and multivesicular bodies. As in all eukaryotic (nucleated) cells, glial cells contain a cytoskeleton composed of protein filaments and microtubules. Thus glial cells, like axons, have a large population of macromolecules within an aqueous environment and therefore should have similar water proton relaxation characteristics.

1.2.5 Extracellular Space

The volume of extracellular space in the vertebrate central nervous system has been the subject of some controversy. Different methods of estimation have indicated a

volume of about 12 to 24% (17). The location and content of extracellular space is not well characterized either. Small extracellular spaces, composed mainly of water, most likely exist between neurons and the supportive glial cell processes. In white matter, there is a straighter and more orderly arrangement of extracellular channels as opposed to the dense jungle of cellular structures present in grey matter. Thus in brain edema, whether it originates in grey or white matter, the edema fluid accumulates in the extracellular space of the white matter. In normal white matter, differences between the compositions of plasma and the extracellular fluid are maintained by the vascular endothelium lining the blood vessels and by the ependymal cells which line the cerebrospinal fluid chambers. Thus the extracellular spaces are devoid of the large macromolecular proteins found in blood, such as albumin. The extracellular spaces also do not contain any of the complex structures and macromolecules present intracellularly. Therefore, the extracellular spaces should have water proton NMR relaxation charcteristics similar to bulk water. However, exchange across single cellular membranes will complicate this relaxation.

1.2.6 Nerve cords of the Peripheral and Central Nervous Systems

In both the PNS and CNS, nerve cords are surrounded and invested by connective tissue which is composed of an extracellular matrix with embedded fibrils of collagen and flattened connective tissue cells. The amount of collagen and the type of connective tissue cells present varies from nerve to nerve and between different regions of the same nerve. In the peripheral nervous system, connective tissues are subdivided into three types: epineurium, perineurium and endoneurium. The epineurium is the loose outer connective tissue sheath binding nerve fascicles together. The perineurium is a multi-layered sheath of dense connective tissue surrounding a single nerve bundle. The layers consist of flattened squamous cells bounded on either side by a basement membrane and separated by fibrils of collagen. The endoneurium, which contains collagen and fibroblasts is distributed around individual myelinated fibres and groups of unmyelinated axons. Endoneurium is the predominant type of connective tissue present in peripheral nerves, while in nerves of the CNS, a connective tissue similar to the perineurium of the PNS is most abundant. Since perineurium is a much denser connective tissue with more collagen than endoneurium, its water proton NMR relaxation characteristics may be distinguishable from that of the endoneurium. Unlike

the PNS, CNS nerves do not have a connective tissue matrix separating individual nerve fibres. Instead, the spaces between myelinated and unmyelinated axons are filled completely with glial cell cytoplasm which is identical to the situation in white matter. Thus CNS nerves and white matter have ~1/2 of the extracellular space that PNS nerves do. Therefore, the contribution of the extracellular water protons to the proton NMR signal in PNS nerves should be greater than that in the CNS.

Another feature distinguishing the PNS from the CNS is the fact that the Schwann cell is the only glial-type cell present in peripheral nerves. It is, therefore, the Schwann cell which myelinates the axons and which surrounds and groups unmyelinated axons together. The molecular composition of Schwann cell myelin is almost identical to that of CNS myelin except that the major protein is glycoprotein rather than myelin basic protein. Although the myelin wrapping process is the same in both the CNS and PNS, there are several structural differences between mature myelin of the two nerve types. The Schwann cell myelinates only one internode unlike the oligodendrocyte which can myelinate up to 50 internodes . It is therefore common in EM sections to see the Schwann cell body associated with the myelin whereas CNS myelin is rarely seen attached to the oligodendrocyte. Schwann cell cytoplasm is present in both the inner and outer layers of the myelin wrapping as well as in Schmidt - Lanterman incisures, which are periodic regions of the major dense line which separate and fill with cytoplasm providing a direct cytoplasmic channel connecting the cell body to the inner cytoplasmic layer and therefore to the axons as well. The cytoplasm of the oligodendrocyte sheath is restricted to inner and outer tongues. The entire Schwann cell-myelin system is bounded by a basement membrane which is continuous with adjacent internodes. In the CNS there is no basement membrane and the myelin sheaths commonly abut. In addition, the intraperiod distance is ~2 nm greater in the PNS than in the CNS(see Fig. 1.3) and the overall PNS myelin thickness is proportional to the axon diameter, a relation not seen in the CNS.

The differences between PNS and CNS myelin may have some consequences for the water proton NMR. The larger intraperiod distance and the presence of the Schmidt-Lanterman incisures may result in a larger water content for PNS myelin . The presence of a basement membrane in the PNS and thicker myelin sheaths, up to 10 times thicker in the case of large PNS axons, also provides a much greater diffusive barrier to water. These factors may have an affect upon measured water proton relaxation times since these times are dependent upon water fractions and exchange rates between anatomical compartments.

1.3 Nuclear Magnetic Resonance (NMR) Theory

1.3.1 Introduction to NMR

All nuclei possess mass and charge. In addition some nuclei also possess finite spin angular momentum denoted by $\mathbf{I}\hbar$, where $\hbar$ is Planck's constant divided by 2π and $\mathbf{I}$ is the spin operator. Basic principles of quantum mechanics tell us that spin angular momentum is quantized and therefore the spin quantum number, I, can only take integral or half integral values. As well, for a given nucleus with spin I, the component of the spin angular momentum vector along any magnetic field axis can only take 2I+1 possible values . These nuclear spin states are characterized by a set of magnetic quantum numbers m=-I, -I+1, ... ,I-1, I. According to the nuclear shell model (18), the spin, I, of a nucleus is determined by the vectoral summation of the individual nucleon spins and orbital angular momenta. In the case of the hydrogen proton, with which we are most interested, I=1/2.

The magnetic moment μ and the spin vector $\mathbf{I}$ are related by

$$\gamma = \frac{\mu}{\mathbf{I}\hbar} \tag{1.1}$$

where γ, the magnetogyric ratio, is determined by the above summation and is unique to each nuclear species.

Classically, when a nuclear magnetic moment is placed in a magnetic field $\mathbf{B_o}$ defining the z-direction, the magnetic moment vector, μ, precesses about the field direction, as shown in Fig. 1.4. The angular frequency, ω_o, of this precession is known as the Larmor frequency and is given by

$$\omega_o = \gamma B_o \tag{1.2}$$

If the magnetic moment is subjected to no other magnetic field interactions, it will continue to precess at this same frequency and at the same orientation, θ, with respect to $\mathbf{B_o}$, indefinitely. However, if a small rotating magnetic field, $\mathbf{B_1}$, is applied perpendicular to $\mathbf{B_o}$ and is caused to rotate at the Larmor frequency and in the same sense as the nuclear precession, then the z-component of the spin magnetic moment will precess about $\mathbf{B_1}$ taking on new orientations with respect to $\mathbf{B_o}$. In the case of I = 1/2 there are only two orientations allowed: one with I_z parallel to $\mathbf{B_o}$, or the spin up state, and one with I_z antiparallel to $\mathbf{B_o}$, or the spin down state.

From a quantum mechanical perspective, consider a nucleus of spin 1/2 in the static magnetic field $\mathbf{B_o}$. The interaction energy between the nuclear magnetic moment and $\mathbf{B_o}$ gives a Hamiltonian of the form

$$\begin{aligned} \mathcal{H} &= -\boldsymbol{\mu} \cdot \mathbf{B_o} \\ &= -\gamma\hbar \mathbf{I} \cdot \mathbf{B_o} \\ &= -\gamma\hbar I_z B_o \ . \end{aligned} \tag{1.3}$$

Thus the eigenvalues of this Hamiltonian are simply the eigenvalues of the I_z spin operator multiplied by ($\gamma\hbar B_o$). Since I=1/2, the eigenvalues of I_z are $\pm 1/2$, and therefore the energy eigenvalues are

$$E = \pm \frac{\gamma\hbar B_o}{2} \ . \tag{1.4}$$

The effect, then, of placing a magnetic moment in a static magnetic field is to split the energy of the two energy eigenstates, |+> and |->, as shown in Fig. 1.5. These levels are often referred to as the Zeeman energy levels and have an energy separation of $\gamma\hbar B_o$.

Nuclear magnetic resonance is produced by the interaction of the nuclear spins with a negatively rotating magnetic field applied perpendicular to the static field. This oscillating field can be written as

$$\mathbf{B_1}(t) = B_1 (\cos\omega t\, \hat{\mathbf{i}} \ - \ \sin\omega t\, \hat{\mathbf{j}}) \tag{1.5}$$

where $\hat{\mathbf{i}}$ and $\hat{\mathbf{j}}$ are the unit vectors in the x and y directions of the laboratory frame. The perturbing Hamiltonian is then given by

$$\begin{aligned} \mathcal{H}_{B_1} &= \gamma\hbar \mathbf{I} \cdot \mathbf{B_1} (\cos\omega t\, \hat{\mathbf{i}} \ - \ \sin\omega t\, \hat{\mathbf{j}}) \\ &= \gamma\hbar B_1 (I_x \cos\omega t \ - \ I_y \sin\omega t) \end{aligned} \tag{1.6}$$

Since the spin operators I_x and I_y have matrix elements between states m and m', where $m' = m \pm 1$, the application of $B_1(t)$ will modify the probability of finding the spin in either of the adjacent levels. To satisfy the conservation of energy the angular frequency of interaction, ω, must be such that

$$\hbar\omega = \Delta E = \gamma\hbar B_0 \quad \text{or}$$
$$\omega = \gamma B_0 = \omega_0 \tag{1.7}$$

Thus the B_1 field must oscillate at the Larmor frequency, ω_0, in order to completely modify the probabilities and allow a transition between adjacent energy eigenstates.

The discovery of this resonance phenomenon was first reported in 1946, simultaneously but independently by the groups of Bloch and Purcell (19, 20). Many different methods of excitation and detection have since been developed, the basics of which can be found in several textbooks (21, 22, 23). Today NMR is an indispensable tool not only for the physicist and chemist, but also for the biochemist in the search for a better understanding of biological macromolecules and proteins, as well as for the medical community in their search for a better diagnosis and an improved understanding of disease. The wide applicability of NMR to medicine is due to the fact that the most abundant nucleus in biological tissue, the water proton, is the most NMR visible stable nucleus (except for ^{3}He) with the simplest spin 1/2. The NMR characteristics of these water protons are very sensitive to the tissue type and to the pathophysiological state of the tissue.

In this thesis we are concerned only with the NMR relaxation characteristics, specifically transverse relaxation, of water protons in nerve tissue. Therefore, the remainder of this section is devoted to a discussion of relaxation specific to a homogeneous population of spin 1/2 nuclei within the heterogeneous system of biological tissue. We begin with a discussion of the macroscopic magnetization.

1.3.2 The Macroscopic Magnetization

For an ensemble of spins in thermal equilibrium, an excess of spins will occupy the lower energy eigenstate, i.e. $|+\rangle$, leading to a net macroscopic magnetization oriented parallel to the static field. It is an experimentally established fact that in thermal equilibrium there is no net magnetization in any direction perpendicular to the static field, the explanation being that the spins precessing about B_0 are out of phase with each other and therefore all magnetization components in the perpendicular direction cancel out. The excess of spins in the lower energy state arises from the equilibration of the spin system with the thermal energy of the lattice. The term "lattice" refers to the many vibrational and rotational energy states occupied by the molecules, atoms and ions of the

entire system. According to the fundamental Boltzmann law of statistical mechanics, which applies to identical but distinguishable particles, the populations of the various energy states of the lattice are proportional to

$$\exp\{-E_i/(kT)\} \tag{1.8}$$

where E_i is the energy corresponding to the i^{th} energy level. This type of energy distribution gives the lattice a unique temperature, T. Since the energy of the spin system is insignificant compared to that of the entire lattice, its temperature must equilibrate to that of the lattice. The system of N identical spins, each occupying a discrete energy level at the lattice temperature T, can only populate the energy states in one way with respect to the total number of spins occupying each energy level. That way must follow a Boltzmann distribution as well, where the lower energy states are more largely populated. Thus for a nuclear spin system of N spins in thermal equilibrium, the net magnetization, $\mathbf{M_o}$, is given to first order by (22)

$$\mathbf{M_o} = N\gamma^2\hbar^2 I(I+1)\frac{\mathbf{B_o}}{3kT} = \chi_o \mathbf{B_o} \quad , \tag{1.9}$$

where χ_o is called the bulk susceptibility and k is Boltzmann's constant.

The spin system can be perturbed from this thermal equilibrium by applying a small, negatively rotating rf magnetic field, $\mathbf{B_1}$, as defined by Eq. 1.5. Thus the total magnetic field, B_{eff}, interacting with the spin system is the vector sum of $\mathbf{B_o}$ and $\mathbf{B_1}$. This vector summation in the laboratory frame is shown in Fig. 1.6(a). The interaction between the macroscopic magnetic moment $\mathbf{M_o}$ and $\mathbf{B_{eff}}$ is simplified if the reference frame is transformed to one rotating at the $\mathbf{B_1}$ frequency ω. The vector summation in this rotating frame is shown in Fig. 1.6(b). This transformation essentially reduces the static field along the z_ρ-direction (ρ denoting the rotating frame of reference) to $\mathbf{B_o} - \omega/\gamma$. Thus when the resonance condition is satisfied, i.e. $\omega = \omega_o$, $\mathbf{B_o}$ is completely transformed away leaving $\mathbf{B_{eff}} = \mathbf{B_1}$. On resonance the equilibrium macroscopic magnetization vector, aligned along z_ρ begins to rotate about $\mathbf{B_1}$ at a frequency $\omega_1 = \gamma B_1$, as shown in Fig. 1.7. If $\mathbf{B_1}$ is applied for the proper duration, then $\mathbf{M_o}$ will come to lie completely in the x-y plane oriented along the y_ρ axis. This is termed a 90° pulse. If the time of this pulse is doubled then $\mathbf{M_o}$ will be inverted 180° and will be completely oriented along the negative z_ρ direction. This type of rf pulse is referred to as a 180°

pulse. If $\omega \neq \omega_0$, perturbation of the macroscopic magnetization can still take place but inversion never occurs. Once perturbed, the spin system is restored to its thermal equilibrium state through interactions between the nuclear spins themselves and between the nuclei and the lattice. The equations of motion of the macroscopic magnetization under the influence of externally applied magnetic fields and internal spin-spin (transverse) and spin-lattice (longitudinal) relaxation interactions are given by the phenomenological equations of Bloch which can be written as

$$\frac{dM}{dt} = \gamma MxB - \frac{(\hat{i}\,M_x + \hat{j}\,M_y)}{T_2} - \frac{\hat{k}(M_z - M_0)}{T_1} \qquad (1.10)$$

where $M_{x,y,z}$ are the components of the macroscopic magnetization in the $\hat{i}, \hat{j}$ and $\hat{k}$ directions, i.e. the unit vectors in the x, y and z directions. These equations, which describe liquid-like systems but do not, in general, describe nuclei in solids, indicate that the transverse magnetization decays exponentially with time constant T_2, while the longitudinal component of the magnetization recovers exponentially with time constant T_1. The longitudinal relaxation involves the exchange of energy between the spin system and the lattice and therefore T_1 characterizes the time required for the spin system to re-establish a Boltzmann population distribution. The transverse relaxation involves the exchange of energy between the spins themselves and therefore T_2 describes the time taken for the spin system to reach an internal equilibrium.

In the late 1940's to mid 50's several authors (24 - 27) developed the theory of nuclear spin relaxation in liquids, the first of these being the "BPP theory" presented by Bloombergen, Purcell, and Pound (24). This theory is very complex, requiring an extensive quantum mechanical treatment, the fundamentals of which can be found in numerous textbooks (28, 29). There are many mechanisms which may contribute to relaxation. These include nuclear dipole-dipole interactions, quadrupole interactions, relaxation due to paramagnetic centers, as well as chemical shift anisotropy. In a given spin system, only one of those mechanisms will usually dominate. In the case of a diamagnetic liquid system of protons ($I = 1/2$), it is the nuclear dipole-dipole interaction which dominates spin-lattice and spin-spin relaxation. In dipole-dipole interaction theory the derivation of the expressions for the relaxation rates is greatly simplified by the rapid motions which occur in a liquid system. The motional averaging greatly reduces the dipolar coupling between nuclear spins and therefore groups of spins can be treated as separate systems coupled independently to the lattice. In this thesis we treat

water proton relaxation in biological systems as being very similar to that in bulk water. Therefore we are concerned only with the dipolar interaction between water protons. The following development of the expressions for relaxation follows that given by Solomon (26) for a two-spin system of like nuclei.

1.3.3 Two-Spin Relaxation

1.3.3.1 The Hamiltonian and its Eigenstates

Consider two like spins (i.e. they have the same γ), I=1/2 and I'=1/2. When placed in a static magnetic field $\mathbf{B_o}$ along the z-direction this system of two spins possesses a Hamiltonian of the form

$$\mathcal{H} = -\gamma\hbar(I_z + I_z') + \mathcal{H}_D \qquad (1.11)$$

where the first term represents the Zeeman energy of the spins with I_z and I_z' being the z-components of the individual spin angular momentum operators. The second term represents the small dipolar interaction between the two spins. The small strength of $\mathcal{H}_D$ relative to the Zeeman energy allows $\mathcal{H}_D$ to be considered as a small perturbation. Thus, according to first order perturbation theory, the eigenstates of the unperturbed Hamiltonian are sufficient for calculation purposes. These eigenstates can be written as |++>, |+->, |-+> and |--> which are all the possible combinations of the individual spin states, i.e. |+> and |-> for each spin. The transitions between these states, as shown in Fig. 1.8, are the mechanisms of longitudinal relaxation. The transition probabilities per unit time, W_o, W_1, W_1' and W_2 are determined by

$$W_{ij} = \frac{1}{\hbar^2}\left| \int_0^t \langle m_j|\, \mathcal{H}_D(t')\, |m_i\rangle \exp\{-i\omega_{ij}t'\}\, dt' \right|^2 \qquad (1.12)$$

where $\omega_{ij} = \dfrac{E_j - E_i}{\hbar}$.

E_i and E_j are the Zeeman energies corresponding to the eigenstates $|m_i\rangle$ and $|m_j\rangle$ of the unperturbed Hamiltonian.

Transverse magnetization, on the other hand, does not involve transitions between the energy eigenstates defined in Fig. 1.8, but instead it involves transitions between the eigenstates of the transverse components of the spin angular momentum operators, I_x (or I_y) and I_x' (or I_y'). These transitions conserve energy within the spin system. The two eigenstates and eigenvalues for each spin are defined by (26)

$$\begin{aligned} I_x |a\rangle_1 &= 1/2\, |a\rangle_1 \\ I_x |b\rangle_1 &= -1/2\, |b\rangle_1 \\ I_x' |a\rangle_2 &= 1/2\, |a\rangle_2 \\ I_x' |b\rangle_2 &= -1/2\, |b\rangle_2 \end{aligned} \qquad (1.13)$$

and therefore the four eigenstates of the two spin system are $|aa\rangle$, $|ab\rangle$, $|ba\rangle$ and $|bb\rangle$ which are not eigenstates of the energy, but are orthogonal. The transition probabilities between these states, U_0, U_1, U_1' and U_2, are defined in Fig. 1.9 (26). In order to calculate each of these transition probabilities, the initial and final states, denoted by $|u\rangle$ and $|v\rangle$ respectively, can be written as linear combinations of the energy eigenstates, i.e.

$$\begin{aligned} |u\rangle &= \sum_{i=1}^{4} u_i |m_i\rangle \\ |v\rangle &= \sum_{i=1}^{4} v_i |m_i\rangle \quad . \end{aligned} \qquad (1.14)$$

Using this expansion and the orthogonality of $|u\rangle$ and $|v\rangle$, Eq. 1.12 can be generalized and used to give the transition probability per unit time between these two transverse eigenstates as follows (26):

$$U_{uv} = \frac{1}{\hbar^2} \left| \int_0^t \sum_{ij} \langle m_j | \mathcal{H}_D(t') | m_i \rangle\, u_i v_j \exp\{-i\omega_{ij} t'\}\, dt' \right|^2 . \qquad (1.15)$$

1.3.3.2 Equations of Motion of the Macroscopic Magnetization

Since the spin system is a sum of the many individual two spin systems coupled independently to the lattice, the energy eigenstates, as well as the eigenstates of the transverse angular momentum, take on various occupation numbers. For the energy eigenstates these are defined as N_{++}, N_{+-}, N_{-+}, N_{--} and for the transverse eigenstates as N_{aa}, N_{ab}, N_{ba} and N_{bb}.

Experimentally it is the ensemble average of $(I_z + I_z')$, defined by $< I_z + I'_z >$, which is observable. This ensemble average is proportional to the occupancy of the states, i.e.

$$< I_z + I'_z > \propto 2(N_{++} - N_{--}) \tag{1.16}$$

Using the definition of the W's, the variation in the populations are given by

$$\begin{aligned}
\frac{dN_{++}}{dt} &= -(W_1 + W_1' + W_2)N_{++} + W_1'N_{+-} + W_1N_{-+} + W_2N_{--} + \text{constant}, \\
\frac{dN_{--}}{dt} &= W_2N_{++} + W_1N_{+-} + W_1'N_{-+} - (W_1 + W_1' + W_2)N_{--} + \text{constant}, \qquad (1.17)
\end{aligned}$$

where $W_1 = W_1'$ because the spins have the same γ.

Taking the derivative with respect to time of Eq. 1.16, substituting Eq. 1.17, and making similar calculations for the transverse components yields the equations of motion for the two observables of the macroscopic magnetization:

$$\begin{aligned}
\frac{d}{dt}(< I_z + I'_z >) &= -2(W_1 + W_2)[< I_z + I'_z > - < I_0 - I'_0 >] \\
\frac{d}{dt}(< I_+ + I'_+ >) &= -2(U_1 + U_2)[< I_+ + I'_+ >] \qquad (1.18)
\end{aligned}$$

where I_0 and I_0' are the equilibrium values of the magnetization. Note that the observable associated with the transverse magnetization is $I_+ = I_x + iI_y$ and not I_x or I_y. Associating $(< I_z + I'_z >)$ with the longitudinal magnetization and $(< I_+ + I'_+ >)$ with the transverse magnetization and comparing Eq. 1.18 with Eq. 1.10 yields

$$\frac{1}{T_1} = 2(W_1 + W_2)$$
$$\frac{1}{T_2} = 2(U_1 + U_2) \quad . \tag{1.19}$$

1.3.3.3 The Dipole-Dipole Interaction

The computation of the transition probabilities per unit time requires the form of the perturbing dipolar Hamiltonian to be known. Consider two dipoles separated by a distance **r**. The magnetic field produced by the first dipole at the position of the second dipole can be calculated by assuming the first dipole is equivalent to two fictitious magnetic monopoles, m, separated by a distance s as shown in Fig. 1.10. Then the scalar potential and the magnetic field can be calculated in a similar manner to that done for the electric dipole (30). At a point, P, the scalar potential ϕ is given by

$$\phi = \frac{\mu_o}{4\pi} m\{\frac{1}{r_a} - \frac{1}{r_b}\} \tag{1.20}$$

where μ_o is the permeability of free space. Using geometry r_a and r_b can be replaced by functions of r, s and θ. Then with $\mu = ms$ and assuming $r >> s$, the expression for potential can be written as

$$\phi = \frac{\mu_o}{4\pi} \frac{(\mu \cdot \hat{r})}{r^2} \tag{1.21}$$

where $\hat{r}$ defines a unit vector in the direction of **r**. The magnetic field of the dipole is then given by

$$b = -\nabla\phi \tag{1.22}$$

which in terms of polar coordinates yields the following

$$b_r = -\frac{\partial\phi}{\partial r} = \frac{\mu_o}{4\pi} 2\mu \frac{\cos\theta}{r^3}$$
$$b_\theta = -\frac{1}{r}\frac{\partial\phi}{\partial\theta} = \frac{\mu_o}{4\pi} \mu \frac{\sin\theta}{r^3}$$
$$b_\psi = -\frac{1}{r\sin\theta}\frac{\partial\phi}{\partial\psi} = 0 \quad , \tag{1.23}$$

or in terms of Cartesian coordinates

$$\mathbf{b} = \frac{\mu_o}{4\pi r^3}\mu\,(3\cos\theta\sin\theta\,\hat{\mathbf{i}}, 0\,\hat{\mathbf{j}}, (3\cos^2\theta - 1)\hat{\mathbf{k}}). \tag{1.24}$$

Splitting this into two terms,

$$\mathbf{b} = \frac{\mu_o}{4\pi r^3}(3\mu\cos\theta)(\sin\theta\,\hat{\mathbf{i}}, 0\,\hat{\mathbf{j}}, \cos\theta\,\hat{\mathbf{k}}) - \frac{\mu_o}{4\pi r^3}\mu \tag{1.25}$$

and substituting

$$\begin{aligned}(\boldsymbol{\mu}\cdot\hat{\mathbf{r}}) &= \mu\cos\theta \\ \hat{\mathbf{r}} &= (\sin\theta\,\hat{\mathbf{i}}, 0\,\hat{\mathbf{j}}, \cos\theta\,\hat{\mathbf{k}}),\end{aligned} \tag{1.26}$$

yields

$$\mathbf{b} = \frac{\mu_o}{4\pi r^3}[3(\boldsymbol{\mu}\cdot\hat{\mathbf{r}})\cdot\hat{\mathbf{r}} - \boldsymbol{\mu}]. \tag{1.27}$$

This is the magnetic field at a point P due to the magnetic moment μ of the first dipole. The interaction energy between the second dipole with magnetic moment μ' and the magnetic field due to μ is given by

$$\begin{aligned}E &= -\boldsymbol{\mu}'\cdot\mathbf{b} \\ &= \frac{\mu_o}{4\pi r^3}[\boldsymbol{\mu}\cdot\boldsymbol{\mu}' - 3(\boldsymbol{\mu}\cdot\hat{\mathbf{r}})(\boldsymbol{\mu}'\cdot\hat{\mathbf{r}})],\end{aligned} \tag{1.28}$$

and substituting $\boldsymbol{\mu} = \gamma\hbar\mathbf{I}$ and $\boldsymbol{\mu}' = \gamma\hbar\mathbf{I}'$ yields

$$E = \frac{\mu_o}{4\pi}\frac{\gamma^2\hbar^2}{r^3}[\mathbf{I}\cdot\mathbf{I}' - 3(\mathbf{I}\cdot\hat{\mathbf{r}})(\mathbf{I}'\cdot\hat{\mathbf{r}})] \tag{1.29}$$

Note that the constant $\mu_o/4\pi$ vanishes if one is working in cgs units. The interaction energy defined by Eq.1.29 is just one form of the perturbing dipolar Hamiltonian, $\mathcal{H}_D$, which for all practical purposes is not used in NMR. Instead, it is transformed to

spherical polar coordinates, with polar angle θ between $\mathbf{r}$ and $\mathbf{B_o}$, and azimuthal angle, ψ. It can then be written in the form (24)

$$\begin{aligned}\mathcal{H}_D = &[\, I_z\Gamma_z - \tfrac{1}{4}(\, I_+\Gamma_- + I_-\Gamma_+ \,)]F_0 \\ &+ [\, I_+\Gamma_z + I_z\Gamma_+ \,]F_1 + [\, I_-\Gamma_z + I_z\Gamma_- \,]F_1^* \\ &+ [\, I_+\Gamma_+ \,]F_2 + [\, I_-\Gamma_- \,]F_2^* \end{aligned} \tag{1.30}$$

where

$$\begin{aligned} F_0(t) &= C[\, 1 - 3\cos^2\theta(t)] \\ F_1(t) &= -\tfrac{3}{2} C \sin\theta(t) \cos\theta(t)\, e^{i\psi(t)} \\ F_2(t) &= -\tfrac{3}{4} C \sin^2\theta(t)\, e^{2i\psi(t)} \\ C &= \frac{\hbar^2\gamma^2}{r^3(t)} \,. \end{aligned} \tag{1.31}$$

and the $F_k^*(t)$ are the complex conjugates of the $F_k(t)$. This type of expansion breaks down the dipolar Hamiltonian into a sum of terms which are products of a spin operator component and a spatial component. The spatial functions, $F_k(t)$, are time dependent due to the motions of the spins, whereas the spin operator terms are time independent. It is the time dependent modulations of the dipolar interaction which induces the transitions between the states of the two-spin system. The integrals defining the transition probabilities per unit time, Eqs. 1.12 and 1.15 can now be solved using the method of Abragam and Pound (25). As an example of this method, the calculation of the W's will be summarized.

Since only the $F_k(t)$ are time dependent, W_{ij} will be of the form

$$W_{ij} = \frac{1}{\hbar^2}\sum_k |\langle m_j| A_K |m_i\rangle|^2 \int_{-t''}^{t''} F_k(t)\, F_k^*(t')\, \exp\{-i\omega_{ij}(t' - t)\}\, dt' \tag{1.32}$$

where the A_k represent the time independent spin operator terms of $\mathcal{H}_D$. Taking the ensemble average over all pairs of interacting spins and evaluating W_{ij} at $t'' >> (t'-t)$ yields

$$W_{ij} = \frac{1}{\hbar^2}\sum_k |\langle m_j| A_K |m_i\rangle|^2 \int_{-\infty}^{\infty} \langle F_k(t)\, F_k^*(t')\rangle \exp\{-i\omega_{ij}\tau\}\, dt' \tag{1.33}$$

where $\tau = (t' - t)$. Since the $F_k(t)$ are random functions of time, then

$$G_k(\tau) = \langle F_k(t)\, F_k^*(t') \rangle \tag{1.34}$$

where $G_k(\tau)$ represents an autocorrelation function. It is well known from statistics that the Fourier transform of an autocorrelation function is the spectral density, J_k, defined as

$$J_k(\omega_{ij}) = \int_{-\infty}^{\infty} G_k(\tau) \exp\{-i\omega_{ij}\tau\}\, d\tau \tag{1.35}$$

Comparing the definition of $J_k(\omega_{ij})$ to the integral in Eq. 1.33 one can see that they are identical yielding

$$W_{ij} = \frac{1}{\hbar^2} \sum_k |\langle m_j | A_K | m_i \rangle|^2 \, J_k(\omega_{ij}) \tag{1.36}$$

To determine the form of the spectral density functions, J_k, it is assumed that the autocorrelation function is exponential with a characteristic time τ_c (the correlation time).

$$\text{i.e.} \qquad G_k(\tau) = G_k(0) \exp\{-\tau/\tau_c\} \tag{1.37}$$

This assumption is based on the continuous rotational diffusion model of Debye. Substituting Eq. 1.37 into 1.35 yields

$$\begin{aligned} J_k(w_{ij}) &= G_k(0) \int_{-\infty}^{\infty} \exp\{-\tau/\tau_c\} \exp\{-i\omega_{ij}\tau\}\, d\tau \\ &= G_k(0)\, \frac{2\tau_c}{1 + \omega_{ij}^2 \tau_c^2} \end{aligned} \tag{1.38}$$

The $G_k(0) = \langle F_k(t)\, F_k^*(t) \rangle$ have been calculated assuming that only the angular coordinates of the F_k are variable and that this variation is random in time (24). This calculation yields:

$$G_0(0) = \frac{4}{5} C^2$$
$$G_1(0) = \frac{3}{10} C^2$$
$$G_2(0) = \frac{3}{10} C^2 \qquad (1.39)$$

Combining equations 1.39, 1.38 and 1.36 and evaluating the spin operator terms yields the following values for the transition probabilities per unit time between the energy eigenstates:

$$W_0 = \frac{1}{10} \frac{C^2}{\hbar^2} \tau_c$$
$$W_1 = \frac{3}{20} \frac{C^2}{\hbar^2} \frac{\tau_c}{1 + \omega_0^2 \tau_c^2}$$
$$W_2 = \frac{3}{10} \frac{C^2}{\hbar^2} \frac{2\tau_c}{1 + 4\omega_0^2 \tau_c^2} \qquad (1.40)$$

Similar calculations for the transverse transition probabilities yield (26)

$$U_0 = \frac{1}{40} \frac{C^2}{\hbar^2} \left[\tau_c + \frac{3\tau_c}{1 + 4\omega_0^2 \tau_c^2} \right]$$
$$U_1 = \frac{1}{40} \frac{C^2}{\hbar^2} \left[\frac{3\tau_c}{1 + \omega_0^2 \tau_c^2} + \frac{3\tau_c}{1 + 4\omega_0^2 \tau_c^2} \right]$$
$$U_2 = \frac{1}{40} \frac{C^2}{\hbar^2} \left[9\tau_c + \frac{12\tau_c}{1 + \omega_0^2 \tau_c^2} + \frac{3\tau_c}{1 + 4\omega_0^2 \tau_c^2} \right] \qquad (1.41)$$

Substituting Eqs. 1.41 and 1.40 into Eqs. 1.19 yields the relaxation rate equations:

$$R_1 = \frac{1}{T_1} = \frac{2}{3} \sigma^2 \left\{ \frac{\tau_c}{1 + \omega_0^2 \tau_c^2} + \frac{4\tau_c}{1 + 4\omega_0^2 \tau_c^2} \right\}$$
$$R_2 = \frac{1}{T_2} = \frac{1}{3} \sigma^2 \left\{ 3\tau_c + \frac{5\tau_c}{1 + \omega_0^2 \tau_c^2} + \frac{2\tau_c}{1 + 4\omega_0^2 \tau_c^2} \right\}. \qquad (1.42)$$

where $\sigma^2 = \frac{9}{20} \frac{\gamma^4 \hbar^2}{r^6}$ is the so-called rigid lattice constant whose value is $2.1 \times 10^{10}\ s^{-2}$ for water molecules where the inter-proton distance, r, is 0.152 nm. The dispersive Lorentzian terms $\tau_c/(1 + \omega_0^2 \tau_c^2)$ and $\tau_c/(1 + 4\omega_0^2 \tau_c^2)$ result in a frequency dependence of the measured relaxation times.

1.3.4 Exchange Between Phases

In a heterogeneous system such as biological tissue, water protons exist in a variety of phases. The term "phase" is used here to denote any homogeneous population of spins having the same intrinsic relaxation parameters. On the smallest scale then, there are the bound-water and free-water phases, while on a larger scale, intracellular water, extracellular water, and myelin water (in the case of myelinated nerve) constitute different water phases as well. The dominant exchange mechanisms affecting transverse relaxation are chemical exchange and translational diffusion between neighboring phases. Chemical exchange involves the physical exchange of water molecules or protons from one phase to another by the breaking and forming of chemical bonds. This type of exchange occurs between the bound and free-water phases. Translational diffusion is the random translational motion of the individual molecules brought about by thermal interactions. Such diffusion causes exchange of water between the larger phases. The exchange between phases caused by either of these mechanisms affects the observed relaxation rates in the tissue. For a two-phase system, Zimmerman and Brittin (31) derived the following expression for the observed magnetization, normalized to unity at time t = 0.

$$\Phi_i(t) = \lambda^+ \exp(-t / T_i^+) + \lambda^- \exp(-t / T_i^-) \qquad (1.43)$$

with

$$\lambda^+ + \lambda^- = 1$$

$$\lambda^\pm = \pm \left\{ \left(\frac{1}{T_i^o} - \frac{1}{T_i^\pm}\right) \Big/ \left(\frac{1}{T_i^+} - \frac{1}{T_i^-}\right) \right\}$$

$$\frac{1}{T_i^\pm} = (1/2)\left\{ \left(\frac{1}{T_{ia}} + \frac{1}{T_{ib}} + \frac{1}{\tau_a} + \frac{1}{\tau_b}\right) \pm \left[\left(\frac{1}{T_{ib}} - \frac{1}{T_{ia}} + \frac{1}{\tau_b} - \frac{1}{\tau_a}\right)^2 + \frac{4}{\tau_a \tau_b} \right]^{1/2} \right\}$$

$$\frac{1}{T_i^o} = \frac{p_a}{T_{ia}} + \frac{p_b}{T_{ib}}$$

$$i=1 \text{ or } 2 \qquad (1.44)$$

where the $\lambda^\pm$ and $T_i^\pm$ are the measured fractional populations and relaxation times, respectively. These will not, in general, be equal to the actual fractional populations of the spins in the two phases, p_a and p_b ($p_a + p_b = 1$), and the intrinsic relaxation times in the two phases, which are T_{ia} and T_{ib}. The lifetime of a water molecule in phase a is

denoted by τ_a while τ_b denotes the lifetime of a water molecule in phase b. Detailed balance dictates that $\frac{p_a}{\tau_a} = \frac{p_b}{\tau_b}$.

There are two cases where the form of Eqs. 1.43 and 1.44 is greatly simplified. If the exchange of water molecules between phases is very fast, such that $\tau_a, \tau_b << T_{ia}, T_{ib}$, then the observed magnetization decay is given by

$$\Phi_i(t) = \exp\left\{-t\left(\frac{p_a}{T_{ia}} + \frac{p_b}{T_{ib}}\right)\right\}, \qquad (1.45)$$

where the magnetization consists of a single exponentially decaying component whose relaxation rate is given by the weighted sum of the individual relaxation rates. This specific case is often referred to as the two-site rapid exchange model. Eq. 1.45 can be generalized to a fast exchange between more than two phases, in which case the characteristic rate of the exponential magnetization decay is a weighted sum of all relaxation rates intrinsic to each phase. Fast exchange is usually the case when considering exchange between bound and free-water phases. Therefore the larger phases, such as intracellular water, have an intrinsic relaxation time which is a fast exchange average of the water bound to intracellular macromolecules and the bulk cytoplasmic water.

If, on the other hand, the exchange between phases is very slow such that $\tau_a, \tau_b >> T_{ia}, T_{ib}$ then Eq. 1.43 reduces to

$$\Phi_i(t) = p_a \exp(-t / T_{ia}) + p_b \exp(-t / T_{ib}), \qquad (1.46)$$

which can also be generalized to a system of J homogeneous phases.

$$\text{i.e.} \quad \Phi_i(t) = \sum_j p_j \exp(-t/T_{ij}). \qquad (1.47)$$

In this so called slow-exchange limit, the observed magnetization decay is the sum of J discrete exponential functions weighted by their fractional populations. In such a system, mathematical inverse techniques can be used to decompose the observed magnetization decay and extract the intrinsic parameters p_j and T_{ij}, which in this case will reflect true populations and relaxation times. The interpretation of the NMR

relaxation measurements made in this thesis are based upon this slow-exchange model. Justification for using the slow exchange limit is given the next section, 1.3.5.

There is an additional spin exchange mechanism, spin diffusion, which predominantly affects longitudinal relaxation but also plays a part in transverse relaxation. This magnetic interaction, which involves a transfer of energy via a mutual flip-flop of spins, only occurs between phases that have intrinsically different relaxation rates and which are very close spatially. Thus spin diffusion is thought to play an important role in the relaxation of hydration water which is believed to cross relax with the protons of the macromolecule.

1.3.5 Transverse Relaxation in Biological Systems

In biological tissue, the chemical exchange between various water phases usually tends towards a fast exchange situation between all phases on a T_1 time scale. On a T_2 time scale the exchange between the larger phases tends to the slow limit. For example, consider the exchange across a single myelin sheath. It has been estimated from permeability measurements on sphingomyelin-cholesterol membranes (32) that a time of ~64 ms is required for the mixing of water in the 10^{th} myelin layer with axonal water. Since the myelin sheaths usually have 15 or more layers, exchange times across the myelin are on the order of 100ms or more. Given that the intrinsic T_1 of myelin water is ~200 ms (33) and the T_1 of axoplasm is of the order of 1 s, the exchange of axonal, myelin, and extra-myelin water approaches the fast exchange limit. The transverse relaxation times of myelin and axoplasm, on the other hand, are much shorter, ~50 ms and ~200 ms respectively. This results in an exchange of water across the myelin which tends towards the slow exchange limit. In the slow exchange limit the decay of the transverse magnetization is multiexponential, as defined by Eq. 1.47. This allows populations and relaxation times in the slow exchanging water phases to be derived. Thus transverse relaxation is a more incisive measure of the state of water in biological tissue than longitudinal relaxation, and therefore, it is the transverse relaxation properties of the white matter tissue model which will be studied in this thesis.

Up to this point, transverse relaxation has only been described in terms of a complicated equation, Eq. 1.42, derived solely from the dipole-dipole interaction. The meaning of this equation is understood as follows. Transverse relaxation is essentially brought about by a gradual dephasing of the transverse components of the individual

nuclear magnetic moments. Because of the dipole-dipole interaction between pairs of spins, each spin sees a slightly different net magnetic field from that seen by its neighbors. This net magnetic field can be represented by $\mathbf{B_o} + \mathbf{B_{Loc}}$, where $\mathbf{B_{Loc}}$ represents the local magnetic field due to neighboring spins. B_{Loc} is a function of r, the distance between spins, and θ, the angle between the line joining the spins and the direction of $\mathbf{B_0}$. Since r and θ vary from one pair of spins to another, and since r and θ also vary in time for each pair of spins, the spins will precess at different frequencies given by $\omega = \gamma(B_0 + B_{Loc})$, resulting in a loss of phase between spins and therefore a loss of transverse magnetization as well. Since B_{Loc} is time dependent, the dephasing which results is irreversible. If the spins are in fast motion as in the case of bulk water, the local magnetic fields are averaged out and dephasing is slow yielding a long T_2. On the other hand, if the spins are moving slowly, as in the case of water protons bound to slowly moving macromolecules, then the local magnetic fields are not averaged out nearly so much and dephasing is fast resulting in a short T_2. This slow motion or zero frequency mechanism for transverse relaxation is represented by the first term in Eq. 1.42. It is the slower motion in biological systems relative to pure water which makes transverse relaxation much more efficient than longitudinal relaxation in biological systems.

Besides creating variations in the local magnetic field, the dipole-dipole interaction also induces transitions between the energy eigenstates of the two-spin system. These transitions include a mutual flip-flop of spins with no overall change in energy of the system, as well as transitions at ω_0 and $2\omega_0$ where energy is exchanged with the lattice. Although the latter two transitions directly affect longitudinal relaxation, all of these transitions shorten the lifetime of the transverse magnetization. These transition mechanisms are represented in Eq. 1.42 by the Debye spectral density terms at the corresponding frequency. Referring to Eq. 1.42, one can see that the dipole-dipole interaction mechanisms for transverse relaxation are most efficient when the motions of the spins are slow , i.e. $\tau_c >> 1/\omega_0$. In this case the zero-frequency interactions, which include the dipolar dephasing and the spin-exchange transitions, dominate transverse relaxation.

In addition to the dipole-dipole interaction, there are other mechanisms affecting transverse relaxation in the two-spin system, which must be addressed. Inhomogeneities in the laboratory magnetic field as well as local field gradients due to inhomogeneities in magnetic susceptibility also cause dephasing of the transverse

magnetization. If the variations in the static magnetic field are represented by δB_o, then the experimental value of the spin-spin relaxation time, defined by T_2^* is (34)

$$\frac{1}{T_2^*} = \frac{1}{T_2} + \frac{\gamma \delta B_o}{2} \tag{1.48}$$

where T_2 is defined by the dipole-dipole interaction, Eq. 1.42. In biological tissue inhomogeneities in magnetic susceptibility occur at the boundaries of major cell structures such as the cell membranes. Structures such as these remain fixed on an NMR time scale and therefore the local field gradients brought about by these magnetic susceptibilities are time independent as are the inhomogeneities of the laboratory magnetic field.

The effects of these static magnetic field variations upon the measured transverse relaxation time can be removed by using a Carr-Purcell-Meiboom-Gill (CPMG) (35, 36) spin echo sequence as shown in Fig. 1.11. This method employs an initial 90° pulse followed by a sequence of equally spaced 180° pulses, which are phase shifted by 90° from the initial pulse, in order to continually refocus the dephasing brought about by the static magnetic field inhomogeneities. However, diffusion across the static local field gradients will cause irreversible dephasing and a loss of transverse magnetization. The extent of this loss is dependent upon the magnitude of the field inhomogeneity and the time period over which the dephasing due to diffusion is allowed to occur. In a CPMG sequence this time period is the time between successive 180° pulses, the echo time (2τ), and is chosen to make the effects of diffusion negligible. For example, in our CPMG experiments the echo time is ~2 ms. With a maximum diffusion coefficient, D, of 2.3×10^{-5} cm^2/s (the diffusion coefficient for pure water at 25 °C) and a field gradient, G, on the order of 10^{-3} gauss/cm, the diffusion term given by (23)

$$-D (\gamma G)^2 \frac{2}{3} \tau^3 \tag{1.49}$$

is negligible. Thus, using the CPMG sequence, the experimentally measured transverse magnetization decay is due solely to the time dependent variations in the local magnetic fields. These time dependent local magnetic field variations are dominated by the dipole-dipole interaction.

In summary the measurement of water proton transverse relaxation times in biological tissue yields a relaxation time, T_2, determined predominantly by the dipole-dipole interaction. The form of this interaction indicates that transverse relaxation is

most efficient when the motions of the water molecules are slow. This is a very important point when considering transverse relaxation in biological tissue. Biological tissue is a heterogeneous system consisting of different types of anatomical compartments such as intracellular and extracellular space. Each of these compartments contains a different population of biological macromolecules and a different relationship between the hydration and bulk water phases. Therefore, each type of compartment will have a characteristic transverse relaxation time, T_2, which is the fast exchange average of the hydration and bulk water phases. The compartment with the larger macromolecular concentration, such as intracellular space will have the shorter transverse relaxation time, T_2. If the exchange of water between these compartments is slow on the time scale of the transverse relaxation, then measurement of the transverse magnetization yields a multiexponential decay, Eq. 1.47, from which compartment populations and relaxation times can be derived.

The ability to decompose the muti-exponential transverse magnetization decay into intrinsic compartment populations and transverse relaxation times may hold great promise for the application of NMR to the study of normal and pathological tissue. As mentioned above, transverse relaxation is sensitive to the state of water in the various anatomical compartments of tissue. The state of water in tissue can change drastically when disease is introduced. For example, in Multiple Sclerosis, white matter myelin breaks down. The decrease in myelin results in a decrease in myelin associated water as well as a decrease in the diffusional barrier between the axonal and extra-axonal spaces. Such changes should have a drastic effect upon the multi-component transverse relaxation time characteristics of the white matter tissue. A recent study (10) of multi-component transverse relaxation in in-vivo white matter of the human brain has shown a decrease in a short T_2 component, attributed to myelin, in regions containing MS lesions. Although this is promising, most in-vivo imaging studies do not have the capability to analyze the transverse magnetization decay in terms of multiple components since their data acquisition and signal-to-noise ratio are too limited. Thus the full potential of multi-component transverse relaxation in-vivo is not yet known. In order to establish this potential, the studies described in the following chapters have been carried out. The first is an evaluation of the effects of in-vivo limitations on this NMR technique, while the second analyzes the transverse relaxation time characteristics of a white matter tissue model.

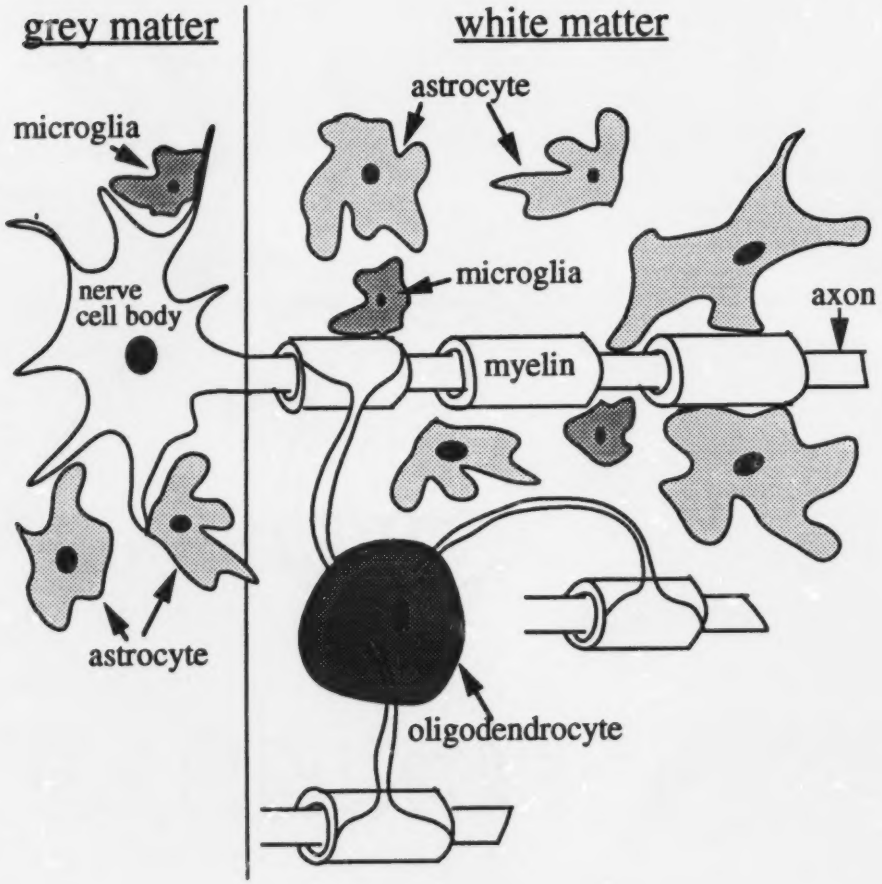

Figure 1.1 Simplistic diagram of white and grey matter of the brain. Grey matter contains the nerve cell bodies surrounded by glial cells, predominantly astrocytes. White matter contains tracts of myelinated nerve axons surrounded by supportive glial cells. The oligodendrocyte is the glial cell type which myelinates the nerve axons.

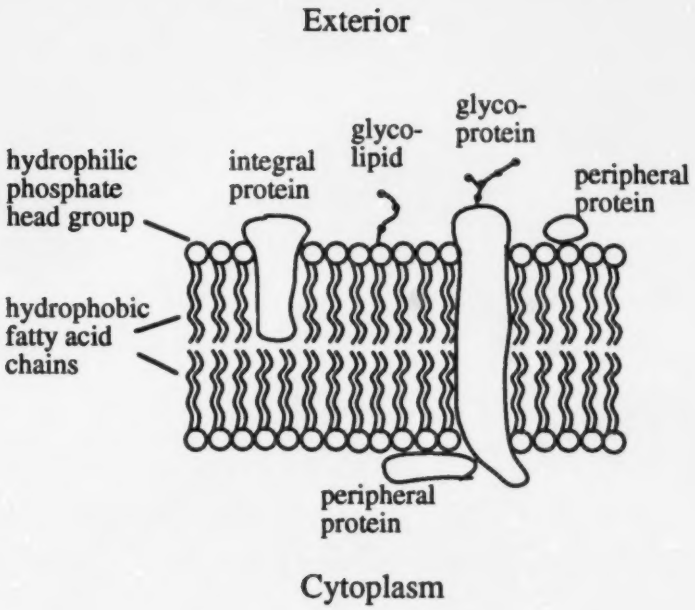

Figure 1.2 Fluid mosaic model of membranes. A phospholipid bilayer constitutes the basic structure. The hydrophobic fatty acid tails form the middle of the bilayer, while the polar, hydrophilic heads of the phospholipids line both surfaces. Integral proteins have a hydrophobic portion which is embedded in the bilayer. Peripheral proteins do not integrate with the membrane but remain on the surface. Oligosaccharides bind to membrane proteins, forming glycoproteins, and to lipids, forming glycolipids. The lipids and proteins of the membrane are believed to be free to move laterally creating a fluid system.

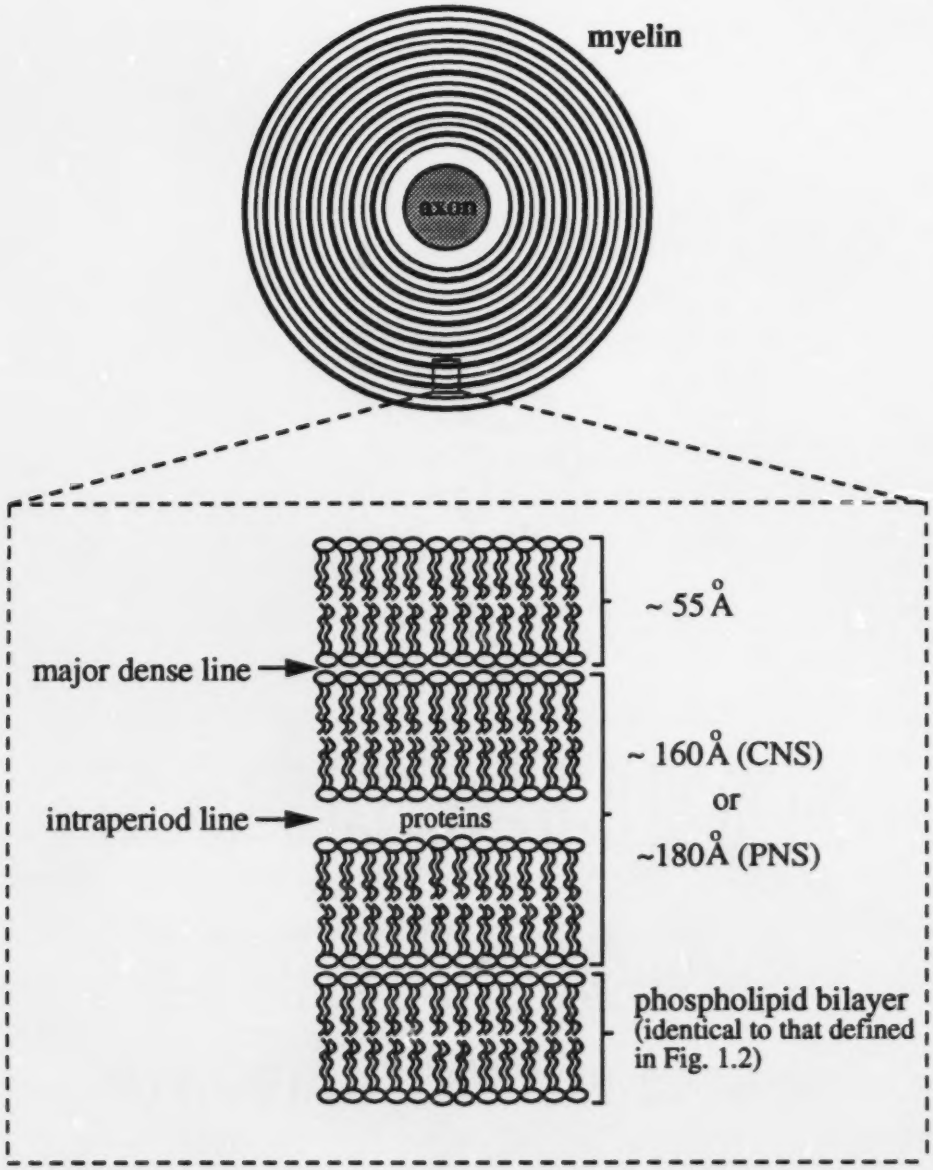

Figure 1.3 Basic structure of myelin. Myelin consists of numerous wrappings of a glial cell process; oligodendrocyte processes in the CNS and Schwann cell processes in the PNS. As the cellular process wraps about the axon, the inner surfaces of the cellular membranes fuse to form the major dense line while the close apposition of the outer membrane surfaces form the intraperiod line.

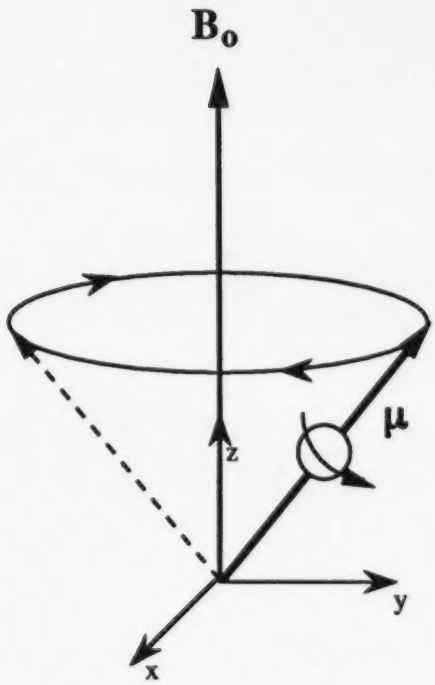

Figure 1.4 Nuclear magnetic moment μ in magnetic field B_o.

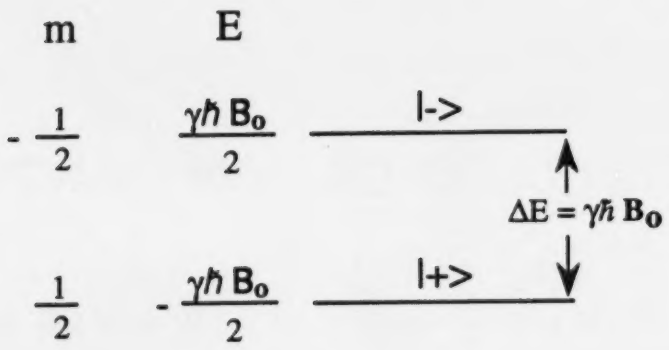

Figure 1.5 Zeeman energy levels for nuclei of spin 1/2 in a magnetic field $\mathbf{B}_o$. The eigenstates corresponding to these levels are defined as |-> and |+> for the spin down (m=-1/2) and the spin up (m=1/2) states, respectively.

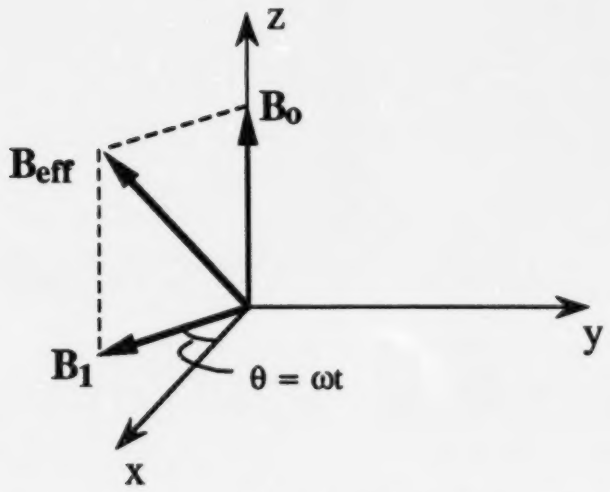

a) Laboratory Frame

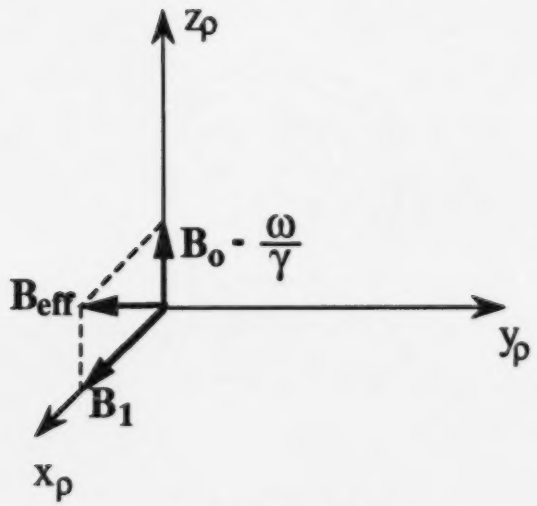

b) Rotating Frame

Figure 1.6 Vector summation of magnetic fields $\mathbf{B_o}$ and $\mathbf{B_1}$ in a) the laboratory reference frame, b) the rotating reference frame.

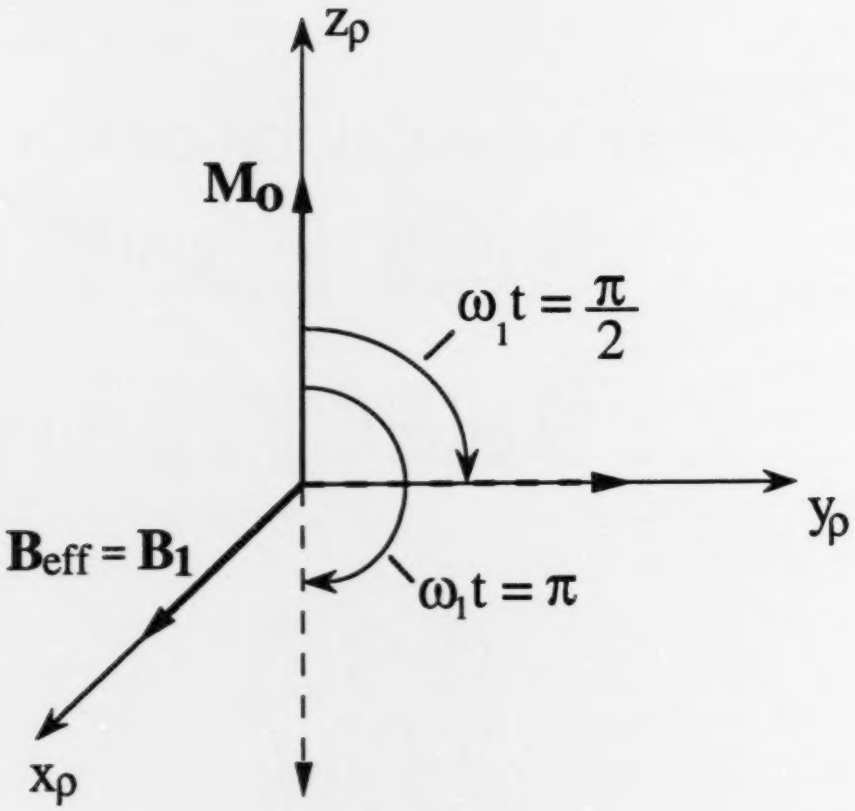

Figure 1.7 Interaction of M_o with $B_{eff} = B_1$ in the rotating frame of reference. M_o precesses about B_1 with angular frequency ω_1. If B_1 is applied for a time t such that the net magnetization lies along the y_ρ axis then the pulse is referred to as a 90^ρ or $\pi/2$ pulse. If this time is doubled, M_o will lie along the $-z_\rho$ axis resulting in a 180^ρ or π pulse.

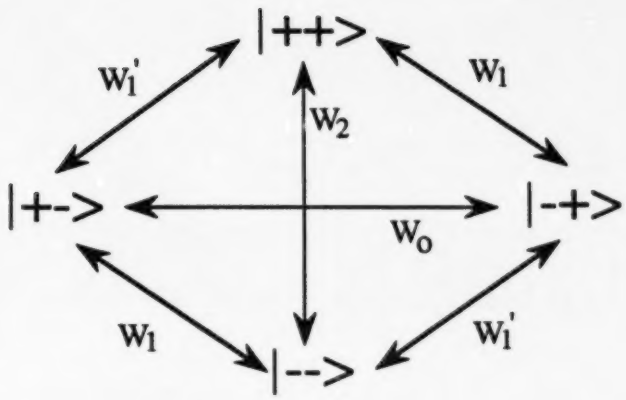

Figure 1.8 Definition of the transition probabilities per unit time between the energy eigenstates of the two-spin system. These transitions are the mechanism of longitudinal relaxation. In the case of water protons the two spins are identical and therefore $W_1 = W_1'$. It has been assumed that the dipolar interaction is a small perturbation and thus the eigenstates shown here, and used in the calculations of the transition probabilities, are the eigenstates of the unperturbed Hamiltonian. Therefore all the W_1's are equivalent.

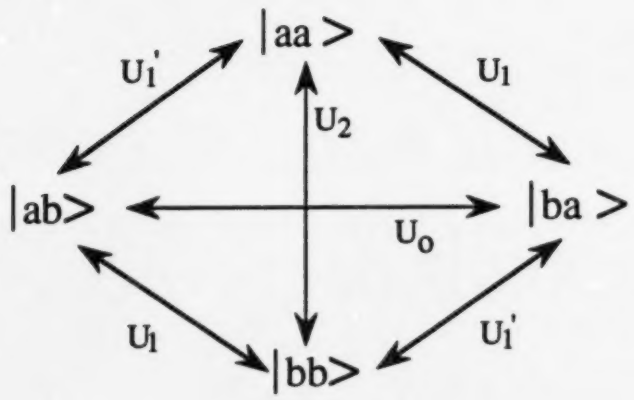

Figure 1.9 Definition of the transition probabilities per unit time between the eigenstates relevant to transverse relaxation in a two-spin system. These states do not commute with I_z and therefore are not energy eigenstates. $U_1 = U_1'$ since the spins are identical.

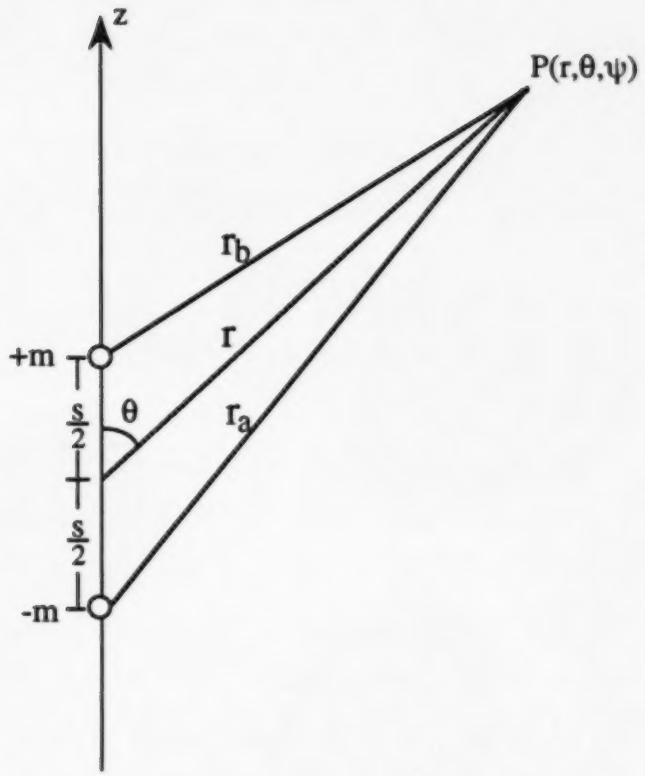

Figure 1.10 Two fictitious magnetic monopoles, m and -m, sepated by a distance s are equivalent to a magnetic dipole with magnetic moment μ = ms. The magnetic potential at a point P is calculated by summing the potentials due to the two monopoles.

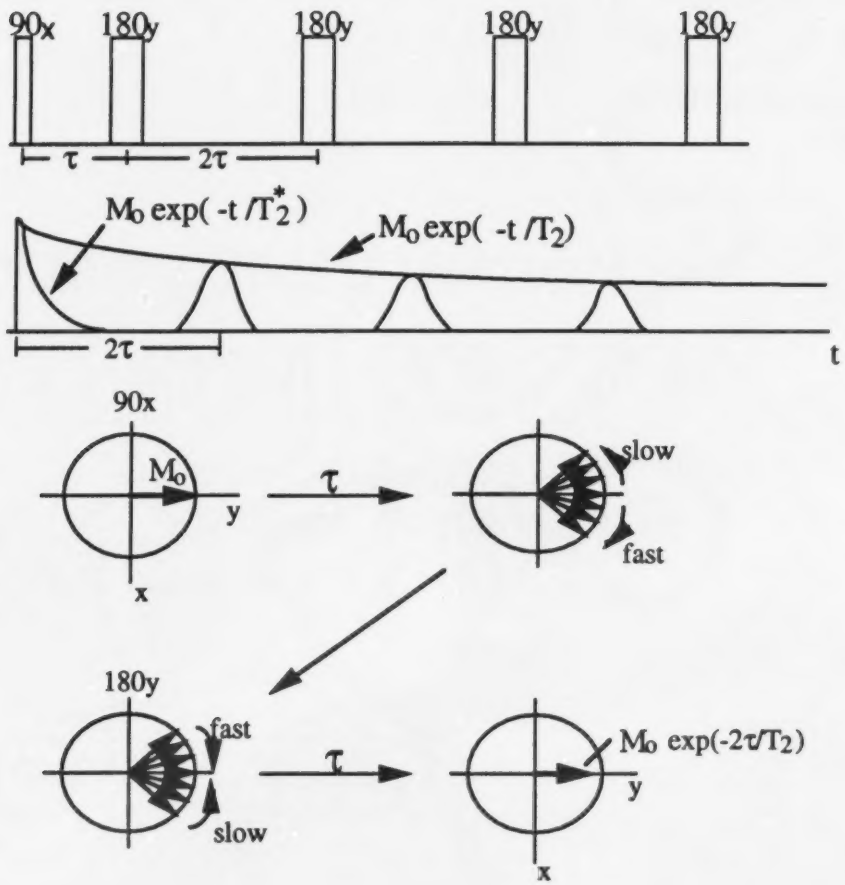

Figure 1.11 CPMG spin-echo sequence. A sequence of 180° pulses produces a train of echoes whose amplitudes decay with time constant T_2. At a time τ after the initial 90° pulse, the individual spins are dephased due to inhomogeneities in the local magnetic fields. The first 180° pulse inverts all spins 180° about the y-axis, and therefore, in another time interval τ the spins are rephased producing the first echo. The decrease in amplitude of the echo from its initial value M_0 is due to the time varying local fields. Successive 180° pulses, thereafter, continually rephase the dephasing brought about by the static field variations.

1.4 References and Selected Bibliography

1. P. A. Bottomley, T. H. Foster, R. E. Argersinger, and L. M. Pfeifer, A review of normal tissue hydrogen NMR relaxation times and relaxation mechanisms from 1-100MHz: Dependence on tissue type, NMR frequency, temperature, species, excision,and age., *Med. Phys.* **11,** 425 (1984).

2. P. A. Bottomley, C. J. Hardy, R. E. Argersinger, and G. Allen-Moore, A review of ^1H nuclear magnetic relaxation in pathology: are T_1 and T_2 diagnostic?, *Med Phys.* **14,** 1 (1987).

3. C. F. Hazlewood, D. C. Chang, B. L. Nichols, and B. E. Woessner, NMR transverse relaxation times of water protons in skeletal muscle, *Biophys. Jour.* **14**, 583 (1974).

4. V. Vasilescu, Eva Katona, V. Simpaceanu, and D. Demco, Water compartments in the myelinated nerve.III Pulsed NMR results, *Experientia* **34**, 1443 (1978).

5. R. S. Menon, M. S. Rusinko, and P. S. Allen, Multiexponential proton relaxation in a model cellular system, *Magn. Reson. Med.* **20**(2), 196 (1991).

6. R. S. Menon, M. S. Rusinko, and P. S. Allen, Proton relaxation studies of water compartmentalization in a model neurological system, *Magn. Reson. Med.* in press.

7. L. Backay, R. J. Kurland, R. G. Parish, J. D. Lee, R. J. Peng and H. M. Bartkowski, Nuclear magnetic resonance studies in normal and edematious brain tissue, water in brain edema, *Exp. Brain. Res.* **23**, 241 (1975).

8. S. Naruse, Y. Horikawa, T. Chuzo, K. Hirakawa, N. Nishikawa and K. Yoshizakai, Proton nuclear magnetic resonance studies on brain edema, *J. Neurosurg.* **56**, 747 (1982).

9. M. E. Castro, "Experimental brain edema studied with proton NMR", Ph.D. Thesis: University of Alberta (1986).

10. A. L. MacKay, K. P. Whittall, K. S. Cover, D. K. B. Li, D. W. Paty, Invivo T_2 relaxation measurements of brain may provide myelin concentration, 10^{th} SMRM, 917, (1991).

11. K. P. Whittall and A. L. Mackay, Quantitative interpretation of NMR relaxation data, *J. Magn. Reson.* **84**, 134 (1989).

12. D. Jensen, "The Human Nervous System", Prentice-Hall Inc., New York (1980).

13. G. H. Bourne, Ed., "The Structrue and Function of Nervous Tissue", Vol 1, Academic Press, New York (1968).

14. P. Morell, Ed., "Myelin", Plenum Press, New York (1984).

15. D. H. Patton, J. W. Sundsten, W. E. Crill, P. D. Swanson, "Introduction to Basic Neurology", W. B. Saunders Company, Toronto (1976).

16. H. W. Fischer, Y. V. Haverbeke, I. Schmitz-Feuerhake, and R. N. Muller, The uncommon longitudinal relaxation dispersion of human brain white matter, *Magn. Reson. Med.* **9**, 441 (1989).

17. W. E. Watson, "Cell Biology of Brain", John Wiley and Sons, Inc., New York (1976).

18. R. M. Eisberg, "Fundamentals of Modern Physics", Wiley, (1961).

19. F. W. Bloch, W. W. Hansen and M. Packard, The nuclear induction experiment, *Phys. Rev.* **69**, 127 (1946).

20. E. M. Purcell, H. C. Torrey and R. V. Pound, Resonance absortion by nuclear magnetic moments in a solid, *Phys. Rev.* **69**, 37 (1946).

21. E. R. Andrew, "Nuclear Magnetic Resonance", Cambridge University Press, Cambridge (1955).

22. A. Abragam, "The Principles of Nuclear Magnetism", Oxford University Press, Oxford (1961).

23. C. P. Slichter, "Principles of Mangnetic Resonance", 3rd Ed., Springer-Verlag, (1980).

24. N. Bloembergen, E. M. Purcell and R. V. Pound, Relaxation effects in NMR absorption, *Phys. Rev.* **73,** 679 (1948).

25. A. Abragam and R. V. Pound, Influence of electric and magnetic fields on angular correlations, *Phys. Rev.* **92,** 943 (1953).

26. I. Solomon, Relaxation process in a system of two spins, *Phys. Rev.* **99**, 579 (1955).

27. R. Kubo and K. Tomita, *J. Phys. Soc. (Japan)* **9**, 888 (1954).

28. E. Merzbacher, "Quantum Mechanics", 2nd Ed., John Wiley and Sons, Toronto (1970).

29. A. Messiah, "Quantum Mechanics", Vol 1 and Vol 2, North Holland (1963).

30. D. P. Corson, P. Lorrain, F. Lorrain, "Electromagnetic Fields and Waves", 3rd Ed., pg. 85, W. H. Freeman and Company, New York (1988).

31. J. R. Zimmerman and W. E. Brittin, Nuclear magnetic resonance studies in multiple phase systems: Lifetime of a water molecule in an adsorbing phase on silica gel, *J. Phys. Chem.* **61**, 1328 (1957).

32. A. Finkelstein, "Water Movement Through Lipid Bilayers, Pores, and Plasma Membranes: Theory and Reality", Wiley, New York, (1987).

33. S. H. Koenig, R. D. Brown, M. Spiller, and N. Lundbom, Relaxometry of brain: why white matter appears bright in MRI, *Magn. Res. Med.* **14**, 482 (1990).

34. F. A. Bovey, "Nuclear Magnetic Resonance Spectroscopy", 2nd Ed., Academic Press, Toronto (1988).

35. H. Y. Carr and E. M. Purcell, Effects of diffusion on free precession in nuclear magnetic resonance experiments, *Phys. Rev.* **94**, 630 (1954).

36. S. Meiboom and C. Gill, Modified spin-echo method for measuring nuclear relaxation times, *Rev. Sci. Instrum.* **29**, 688 (1958).

CHAPTER 2

A Simulation Evaluation of a Linear Inverse Technique for Determining Continuous Relaxation Time Distributions

2.1 Introduction

When interpreting the proton NMR relaxation time characteristics of heterogeneous biological systems, it is logical to assume a continuous distribution of relaxation times. Biological tissue represents a heterogeneous system because water molecules are present in a variety of anatomical compartments, each of which is characterized by a different relationship between the water and the microcellular architecture. Naively, this compartmentalization of water might be thought to give rise to multiple discrete relaxation time components. However, the heterogeneity within each compartment and the various rates of water exchange between compartments can be expected to lead to continuous distributions of relaxation times rather than to discrete components.

The inversion of multicomponent decay data from the transverse magnetization of water protons is an ill-posed problem with non-unique solutions. Because of this non-uniqueness, it has been proposed that the relaxation data be analyzed using a variety of algorithms which construct minimum-structure solutions (1). The variety of solutions can be valuable because features common to several solutions are more likely required by the data and are unlikely to be simply artifacts of the noise or construction algorithm. The most commonly used solution to the multicomponent problem in NMR relaxation is in terms of a predefined number of discrete exponentials. This is a method which is not necessarily minimum structure. Nonetheless, minimum structure solutions can be made up of T_2 spectra composed of a few isolated delta-functions, or of spectra composed of a continuous distribution of relaxation times. We find that any features present in the smoothed solutions are always found in the discrete delta-function solutions, whereas, the converse of this is not always true. For example, a delta-function solution may show two discrete components whereas the smoothed solution will show one broad component spanning the same range of relaxation times. Thus, the continuous distribution solutions seem to give a more conservative indication of which features are necessary to fit the data. Other types of minimum-structure solution can be

obtained by using linear programming methods (1) and lead to histogram like distributions. In view of our preference for continuous distribution solutions as the type of solution most representative of reality in biological tissue, we have chosen to investigate this form of solution through an in depth simulation study.

Algorithms to analyze a multiexponential decay in terms of a continuous distribution of relaxation times have been developed by Provencher (2,3) and by Whittall and MacKay (4). These algorithms have already been used successfully in the study of biological NMR relaxation data (5-10). Modified forms of Whittall and MacKay's technique have also been used to recover distributions of compartment sizes from NMR relaxation data (11), as well as two dimensional NMR time correlation spectra of T_1 and T_2 relaxation in heterogeneous systems (12). All forms of Whittall and MacKay's technique utilize the non-negative least-squares (NNLS) algorithm of Lawson and Hanson (13). Since our interests lie in the determination of continuous distributions of relaxation times, the original form of Whittall and Mackay's algorithm is the inversion method used in the proton transverse relaxation time studies of a white matter model presented in this thesis. For our purposes we have called the algorithm T2LIN.

Due to the limitations of the experimental apparatus used in an NMR experiment, there are constraints imposed upon the measurable precision and completeness of the raw multiexponential decay data. Limitations in signal-to-noise ratio (SNR) for example, as well as limitations in the density and range of the decay time-domain data points are unavoidable. Of course, as one goes from the in-vitro to the in-vivo experimental setting, the seriousness of these constraints increases considerably. Since it is our ultimate goal to apply the continuous distribution technique in-vivo, it is very important to know how such constraints can affect the performance of T2LIN. To our knowledge four previous studies have addressed accuracy and reliability issues for algorithms generating continuous and discrete relaxation time spectra in NMR (1,4,5,14). The work reported by Whittall, Bronskill, and Henkelman (1) was carried out concurrently with our own. Below we summarize the findings in each of the four reports.

Kroeker and Henkelman (5) did two tests of CONTIN, the algorithm developed by Provencher (2,3). First, they tested its accuracy by simulating unimodal Gaussian distributions of relaxation times and measuring the full width at half maximum (FWHM) of the resulting distributions as a function of the signal-to-noise ratio (SNR) of the simulated raw data, as well as by determining the errors in the peak positions.

Four different distribution widths, from 0 to 70% of the distribution's mean relaxation time, were analyzed and zero mean Gaussian noise was added to give SNR values ranging from infinity down to 10. Their results showed that the CONTIN program was able to fit unimodal Gaussian distributions very well. The FWHM of the solution did increase as the SNR decreased but this increase was not significant for SNR greater than 100, and therefore the solution widths reflected the true width of the data, provided the SNR was greater than 100. Secondly, Kroeker and Henkelman also simulated a two component delta-function situation and measured the threshold SNR required to resolve the two components as a function of peak separation and component weightings. The components were considered to be resolved when the solution showed two peaks with the peak positions within 100ms of input times and amplitudes within 10% of the input amplitudes. Therefore at a given peak separation and component weighting, the components were either resolved or not resolved, and no intermediate measures of resolution were made. Curves of threshold SNR versus the ratio of component amplitudes, A/B, were plotted for six equally spaced relaxation time ratios, T_A/T_B, ranging from 0.1 to 0.6. As T_A/T_B was increased, i.e. the short component was moved closer to the long component which remained fixed at 1 s, the curves of threshold SNR versus A/B shifted upwards indicating that larger SNR values were required to resolve the two components. Each increment in T_A/T_B increased the SNR by a factor of approximately 2.5. When the shorter relaxation time component was dominant, i.e. A/B = 4, four times the SNR, as compared to when A/B = 1, was required to resolve the two peaks because the short relaxation times had been relatively under sampled. When the longer relaxation time component dominated, A/B = 0.2, SNR values 1.5 times greater were required for resolution because the longer relaxation time became indistinguishable from the baseline. Thus the curves of threshold SNR versus A/B showed minima for components of approximately equal amplitude, and these minima ranged from SNR values of 40 to 10,000 over the range of relaxation time ratios.

Whittall and MacKay (4) synthesized only two data sets to test their continuous distribution technique. The first set corresponded to a discrete spectrum composed of delta-functions at a few isolated relaxation times. The second corresponded to a continuous distribution of relaxation times which was representative of transverse relaxation of water in wood. One hundred logarithmically spaced data points between 1 ms and 500 ms were generated and zero mean Gaussian noise was added to yield a SNR of 500. The constructed continuous distribution solution was in good agreement with the simulated continuous spectrum, whereas the solution corresponding to the

discrete spectrum was much over-smoothed. This indicates that the continuous distribution technique is much better suited for determining continuous, rather than discrete, distributions of relaxation times.

In a related study, Brown (14) did not analyze any specific data inversion technique, but instead provided guidelines for the amount of detail in a multicomponent relaxation time solution that could be derived from noisy multiexponential decay data. Using rectangular distributions of relaxation times which varied in width, he calculated, what he calls, the least-maximum absolute-errors (LMAE) which arise from the fitting of from one to five discrete exponential components to these rectangular distributions. These LMAE values can be used to calculate the threshold SNR required to distinguish between a given number of discrete components and a single rectangular distribution. For example, Brown generalized his LMAE equation, in the case of two components, to include other types of continuous distributions besides the rectangular type. This generalized equation is of the following form:

$$E_2 \approx \frac{y^2}{6.87 + 15.9y + 7.2y^2} \qquad (2.1)$$

where $y = \frac{1}{12}(\ln Y)^2$, Y being the ratio between the two relaxation times. E_2 is a measure of the data accuracy required to distinguish between two discrete components and a unimodal distribution. In other words, E_2 is the maximum noise level, as a fraction of the initial relaxing amplitude, that can contaminate the data and therefore $1/E_2$ is the threshold SNR required to resolve two components separated by a factor Y. Actually, the SNR required will be somewhat less than $1/E_2$ if there is a number of data points that allows some smoothing. Brown predicted that the threshold SNR would be decreased by a generous factor of $\sqrt{N/8}$, i.e. $SNR=1/(E_2\sqrt{N/8})$. Brown's results can be used to determine whether or not a data inversion algorithm is providing as much information as is allowable by the data. Kroeker and Henkelman's threshold SNR is close to $1/(2E_2)$, except for extreme values of A/B. Comparing this to Brown's estimate of threshold SNR, $1/(5E_2)$ (since N ~ 200), one can conclude that CONTIN is not providing more information, in terms of resolving delta function components, than is allowable by the data. Likewise, we will be able to use Brown's results to determine whether or not T2LIN is providing the proper amount of information given the noisy multiexponential data.

In the study done concurrently with our own, Whittall, Bronskill and Henkelman, WBH, (1) used a method developed by Backus and Gilbert (15) to examine how to choose N, SNR, and the data point acquisition format to maximize the information extractable from multiexponential relaxation data. Their study was not specific to a particular inversion algorithm but had general applicability. With respect to data point acquisition formats, they tested only two data sets: 100 linearly spaced decay curve data points covering the interval from 1 ms to 500 ms, and 100 logarithmically spaced data over the same interval. In the case of the linear sampling, their results showed a degradation of fast relaxing components due to the undersampling of data at short times. This same result had been reported previously by the same authors (5). To determine the effects of various N and SNR on resolution they generated 9 data sets in total. Each data set contained 30, 60, or 120 points spaced logarithmically from 1ms to 500ms and had its SNR set at 250, 125, or 62.5, where the SNR was defined as the ratio of the decay curve maximum at zero time to the standard deviation of the added noise. From their results, they suggest that the resolving power follows the product $SNR\sqrt{N}$ although their actual definition of resolving power is never made clear. The suggestion of a $\sqrt{N}$ relation is consistent with the prediction of Brown (14) that the threshold SNR would decrease by $\sqrt{N/8}$. Hence, to achieve the same resolution at half the SNR it is necessary to measure four times as many data points. To look at the relation another way, increasing the number of data points by say a factor of four is essentially the same as repeating the initial measurements 4 times thereby doubling the SNR.

Neither the previous test of the Whittal and MacKay algorithm by themselves (4) nor that of the Provencher algorithm by Kroeker and Henkelman (5) was able to answer fully questions pertaining to the precision and resolving power of T2LIN which arose from our experimental work. First of all, the resolution of two closely spaced components of a continuous distribution by T2LIN was not known in terms of SNR, their closeness of approach or their widths. Whittall and MacKay (4) did not address the question of the resolution at all and Kroeker and Henkelman (5), who tested the resolving power of the similar, but significantly different algorithm, CONTIN, used only a simulated two-component delta-function data set, not a two-component continuous distribution data set. In section 2.4.1 we report the results of our test which quantifies the continuous variation of a well defined measure of two component resolution in terms of the continuous variation of the SNR and closeness of approach, over ranges that encompass the characteristics of both in-vivo and in-vitro studies. These results are <u>not</u>

superseded by the recent publication of Whittall, Bronskill and Henkelman (1), because in that work, WBH provide no measure of actual resolution, do not vary the closeness of approach and limit the SNR to values typical of in-vivo experiment only. Secondly, a test which is particularly relevant to the application of the T2LIN algorithm under in-vivo conditions, and which to our knowledge had never been carried out, was to relate the resolution of two peaks to the effect of decreasing the number of data points within a fixed time window of the raw data. Although, Brown (14) had previously predicted from general considerations a $\sqrt{N}$ factor governing the threshold SNR for two component resolution, and although WBH(1) have recently derived a similar result, no test of this relationship has been carried out for a specific inversion algorithm. We have not only addressed this point but we also show that even at a constant standard deviation in the noise the resolution is dependent on the particular realization of that noise. Thus, a statistical analysis of the change in variability in resolution, as well as in the resolution itself, as the number of data points is decreased has been carried out at two different SNR values. A third test, which is also very relevant to the application of the T2LIN algorithm under in-vivo conditions and which to our knowledge had never been carried out, was designed to determine the effect of restricting the time window of the raw data at decreasing SNR values. Finally, it was necessary to determine if T2LIN was providing as much information as the data accuracy would allow.

The following chapter is therefore devoted to a discussion of (i) the theoretical basis for T2LIN and its difference from CONTIN, (ii) the methodology for carrying out the above tests, (iii) the results of the tests and (iv) a discussion of their significance in relation to the resolving power and precision of T2LIN in determining continuous distributions of relaxation times when various experimental constraints are imposed, particularly those of in-vivo situations.

2.2 Theory

The general integral equation which can be used to model multiexponential NMR relaxation is given by

$$M(t_i) = \int_0^\infty S(T)\exp(-t_i/T)dT \qquad i = 1, 2, \ldots, N \quad , \qquad (2.2)$$

where $M(t_i)$ represents the magnetization decay amplitude at N discrete times, t_i, and $S(T)$ is the unknown fractional amplitude of the magnetization relaxing with the time constant T, where T can represent a longitudinal relaxation time, T_1, a transverse relaxation time, T_2, or a longitudinal relaxation time in the rotating frame, $T_{1\rho}$. Traditional nonlinear least-squares methods of solving Eq. (2.2) introduce several inherent problems. For example, they require an initial estimate of the solution, i.e. the number of components, and have difficulties converging when that number of components exceeds 4 or 5. These solutions are also sensitive to the time range of the data, becoming unstable if initial data points are removed (5). Linear inverse methods on the other hand, are not hampered by such difficulties, particularly the "a priori" need for the number of components. Provencher (2), Whittall and MacKay (4) and references therein, discuss in detail linear inverse theory solutions to equations similar in form to Eq. (2.2). Moreover, both Provencher, and Whittall and MacKay, developed linear inverse techniques with additional smoothing constraints which give continuous distribution solutions. Provencher created CONTIN which is a very flexible self-contained Fortran program with numerous subprograms to analyze many different types of inversion problems such as photon correlation spectroscopy, Fourier and Laplace transforms, and multicomponent spectra. Whittall and MacKay developed their algorithm specifically for the analysis of NMR relaxation data making it much shorter, easier to program and implement, and less expensive in terms of computation time than CONTIN. Thus, it is Whittall and MacKay's algorithm, which is called T2LIN in the following pages, that provides the continuous relaxation time distribution analysis technique which we require in order to study accurately the transverse relaxation time properties of nervous tissue. Both T2LIN and CONTIN have the same basic methodology, however there are some significant differences. The following is a discussion of the methodology specific to T2LIN. Any major differences with CONTIN will be noted.

T2LIN begins by transforming Eq. (2.2) into a discrete form. This is done by assuming that the spectrum $S(T)$ is a sum of K delta functions, each with unknown weighting $S(T_j)$ at a defined set of relaxation times T_j. Eq. (2.2) can then be written in the form

$$M(t_i) = \sum_{j=1}^{K} \exp(-t_i/T_j) S(T_j) \qquad i = 1, 2, \ldots, N \ . \tag{2.3}$$

Eq. (2.3) is a linear system of equations with general form:

$$M_i = \sum_{j=1}^{K} A_{ij} S_j \qquad i = 1,2,...,N \quad , \tag{2.4}$$

or expressed in matrix form:

$$\begin{bmatrix} M_1 \\ M_2 \\ \cdot \\ \cdot \\ \cdot \\ M_N \end{bmatrix} = \begin{bmatrix} A_{11} & A_{12} & \cdots & A_{1K} \\ A_{21} & A_{22} & & \\ \cdot & & \cdot & \\ \cdot & & & \cdot \\ \cdot & & & \\ A_{N1} & & & A_{NK} \end{bmatrix} \begin{bmatrix} S_1 \\ S_2 \\ \cdot \\ \cdot \\ \cdot \\ S_K \end{bmatrix}$$

where, in the case of Eq. (2.3), **A** is a matrix with elements $\exp(-t_i/T_j)$. In the following work a relaxation time grid T_j was chosen to have K = 200 logarithmically spaced points between 1 ms and 10 s. This range was chosen so as to include only that subset of relaxation times relevant to the ultimate application in biological tissue. The logarithmic spacing is the most appropriate because the range extends over 4 decades of time and this type of spacing allows the short time components to be defined with as many solution points as the long time components.

The linear system of equations, Eq. (2.4) can now be solved for $S(T_j)$ by using a linear inverse technique. The T2LIN algorithm utilizes the non-negative least-squares (NNLS) algorithm of Lawson and Hanson (13) to accomplish this whereas CONTIN has its own computational method for inversion (2). It is the linear inverse nature of these techniques which remove the "a priori" need for the number of components to be specified. Both NNLS and CONTIN solve Eq. (2.4) by using a finite number of stable Householder transformations (13). The resulting solution is essentially the least squares solution with the linear inequality constraint of non-negativity, i.e.

$$\sum_{i=1}^{N} \left| \sum_{j=1}^{K} A_{ij} S_j - M_i \right|^2 \quad \text{is minimized subject to } S_j \geq 0. \tag{2.5}$$

The non-negativity is implicit in the formulations of both NNLS and CONTIN. The least squares solution which minimizes Eq. (2.5) is a discrete delta-function solution. T2LIN uses an average of the delta function residuals around each time domain data point to estimate the standard deviation of the noise, σ_i, associated with each datum, $M(t_i)$. Each data point and its corresponding row of **A** are then divided by this estimate before further fitting, resulting in a weighted solution.

Due to the noise contaminating the data, Eq. (2.5) cannot be minimized to zero. A measure of the goodness of fit can be obtained by defining a misfit variable χ^2, where

$$\chi^2 = \sum_{i=1}^{N} \frac{[\, M_p(t_i) - M(t_i)\,]^2}{\sigma_i^2} = \sum_{i=1}^{N} \frac{[\, M_p(t_i) - M(t_i)]^2}{[\, M_t(t_i) - M(t_i)]^2} \qquad (2.6)$$

provides the measure of misfit between the raw data $M(t_i)$ and the calculated magnetization data point $M_p(t_i)$ corresponding to a particular solution S(T). In Eq. (2.6), $M_t(t_i)$ is the true magnetization data point uncorrupted by noise, and σ_i is the standard deviation of the noise associated with the i^{th} data point. The preferred solution is one which should misfit the noisy data by an amount which is consistent with the noise variations, i.e. one in which $[M_p(t_i) - M(t_i)] \approx [M_t(t_i) - M(t_i)]$. In this case

$$\chi^2_{\text{preferred}} \approx \sum_{i=1}^{N} 1 \approx N\,. \qquad (2.7)$$

The delta-function solution which minimizes Eq. (2.5) is just one member of a large set of possible solutions which fit the data within the error. However, this is not the preferred solution we are seeking, for the following reasons. First, it consists of a small number of isolated delta function components instead of the more plausible continuous distribution model we are looking for; and secondly, it fits the noisy data too closely, i.e. $[M_p(t_i) - M(t_i)] < [M_t(t_i) - M(t_i)]$ yielding $\chi^2 < N$, which could result in noise artifacts in the solution in the form of extra peaks, shifted peaks and incorrect amplitudes. These difficulties can be overcome by adding extra constraints to the minimization function of Eq. (2.5). These extra constraints allow different elements in the set of all possible solutions to be sampled and can be chosen to yield solutions consistent with the system being modelled, continuous distributions of relaxation times

in this case. The extra constraints are incorporated by the addition of a smoothing term to the minimization function of Eq. (2.5), i.e.

$$\sum_{i=1}^{N} \left| \sum_{j=1}^{K} A_{ij} S_j - M_i \right|^2 \quad + \quad \mu \sum_{p=1}^{P} \left| \sum_{j=1}^{K} H_{pj} S_j - f_p \right|^2 \qquad (2.8)$$

where μ is a term referred to as the trade-off parameter or regulariser (2,4,5), **H** is a matrix representing P additional constraints, and f_p is a vector estimating the form of $\mathbf{H} \cdot \mathbf{S}$. The least squares or delta-function solution is obtained when μ=0. The larger the value of μ the more the algorithm attempts to minimize the second term in Eq. (2.8) at the expense of increasing the first term. Note that the first term is identical to the χ^2 misfit, Eq. (2.6), since the elements of the matrix **A** and each data point , M_i , have been divided by their respective noise estimates in order to provide a weighted least squares solution. Thus the χ^2 misfit increases monotonically with μ.

The matrix **H** can take on many forms. However, only that form of **H** which will result in a solution consistent with the continuous distribution model is of interest. Three forms of **H** which meet this requirement are as follows. If **H** is the KxK identity matrix and f_p is the zero vector, then the extra constraints minimize the "energy" in the spectrum:

$$\sum_{j=1}^{K} S_j^2 \ . \qquad (2.9)$$

The term "energy" is used here to describe a sum of squared amplitudes. The two other forms of **H** set the rows equal to finite difference approximations of first order or second order derivatives of S(T). These constraints minimize the energy in the spectrum derivative

$$\sum_{j=1}^{K-1} |S_{j+1} - S_j|^2 \ , \qquad (2.10)$$

or the energy in the spectrum curvature

$$\sum_{j=1}^{K-2} |S_{j+2} - 2S_{j+1} + S_j|^2 \ , \qquad (2.11)$$

respectively, when f_p is again zero. If an initial estimate of the spectrum, its derivative or its curvature is known then it can be entered as the vector f_p and the constraints will minimize the difference between this estimate and the solution. Since initial estimates are not known in this case, f_p is always zero. These three particular forms of **H** have essentially the same effect in that they smooth the solution into a continuous distribution of relaxation times and they increase the misfit. Provencher (2) chose to smooth by minimizing the second derivative function Eq. (2.11), however CONTIN allows for various forms of **H** and f_p to be used. The T2LIN algorithm provides the option of minimizing either the energy in the spectrum, Eq. (2.9), or the spectrum derivative, Eq. (2.10). Whittall and MacKay (4) presented solutions smoothed using the latter equation. In all the experimental and simulation work done for this thesis, Eq. (2.9) was chosen as it was the simplest to implement, and provided good results.

The extra constraints imposed by the addition of the smoothing term in Eq. (2.8) are incorporated by the addition of extra rows in the matrix **A** of Eq. (2.4). Thus in the case of smoothing with Eq. (2.9), the matrix equation takes on the following form:

$$\begin{bmatrix} M_1 \\ M_2 \\ \cdot \\ \cdot \\ \cdot \\ M_N \\ 0 \\ 0 \\ \cdot \\ \cdot \\ \cdot \\ 0 \end{bmatrix} = \begin{bmatrix} A_{11} & A_{12} & \cdot & \cdot & \cdot & A_{1K} \\ A_{21} & A_{22} & \cdot & \cdot & \cdot & A_{2K} \\ \cdot & & \cdot & & & \cdot \\ \cdot & & & \cdot & & \cdot \\ \cdot & & & & & \cdot \\ A_{N1} & \cdot & \cdot & \cdot & & A_{NK} \\ \sqrt{\mu} & 0 & \cdot & \cdot & \cdot & 0 \\ 0 & \sqrt{\mu} & & & & \cdot \\ \cdot & & \sqrt{\mu} & & & \cdot \\ \cdot & & & \sqrt{\mu} & & \cdot \\ \cdot & & & & \sqrt{\mu} & 0 \\ 0 & \cdot & \cdot & \cdot & 0 & \sqrt{\mu} \end{bmatrix} \begin{bmatrix} S_1 \\ S_2 \\ \cdot \\ \cdot \\ \cdot \\ S_K \end{bmatrix}$$

$(N+K)x1$ $\qquad$ $(N+K)xK$ $\qquad$ $Kx1$

This new system of linear equations is again solved for S(T) by the NNLS algorithm resulting in a continuous distribution solution.

The problem which now remains is to determine which value of μ should be used. First, one needs to consider how μ relates to the value of χ^2 for the preferred

solution. If a particular solution is under-smoothed, i.e. μ is too small, the differences $[M_p(t_i) - M(t_i)]$ will be less than $[M_t(t_i) - M(t_i)]$, resulting in $\chi^2 << N$ and the potential for solution structure which is an artifact of the noise is caused. Conversely, if a particular solution is over-smoothed, i.e. μ is too large, then $[M_p(t_i) - M(t_i)]$ is too large, yielding $\chi^2 >> N$ and a broadly smeared solution is obtained which does not truly reflect the information contained in the data. The preferred, optimally smoothed, solution has $\chi^2 \approx N$ (16).

As mentioned previously the standard deviation, σ_i, of each data point due to noise, is estimated for both experimental and simulated data using the average of the delta function residuals around each data point. With this noise estimate it is consistently found that $\chi^2 \approx N$ for the delta function solution, which indicates that we are underestimating the noise somewhat. The preferred solution then, will have $\chi^2 > N$ since it should have a larger misfit than the delta function solution in order to avoid fitting any of the noise. The degree to which χ^2 is allowed to exceed N is determined by the statistics of the χ^2 distribution itself. The frequency distribution of the χ^2 statistic is given by the following equation (17):

$$F(\chi^2) = \frac{1}{2^{N/2}\,\Gamma\left[\frac{N}{2}\right]} \exp\left[\frac{-\chi^2}{2}\right] \chi^{2(N/2)-1} \qquad (2.12)$$

where Γ is the gamma function

$$\Gamma[N] = \int_0^\infty e^{-x}\, x^{N-1}\, dx \qquad (2.13)$$

This frequency distribution of χ^2, illustrated in Fig. (2.1), gives a most probable χ^2 of N-2, a mean χ^2 of N, and a standard deviation of $\sqrt{2N}$. These statistics determine the acceptable upper boundary on χ^2 in relation to the confidence which we have in the solution. The amplitude of the distribution at any given χ^2 represents the probability that a given solution will have that χ^2 value. As χ^2 increases beyond its most probable value, the area under the curve to the left of χ^2 represents the probability that any solution, including the preferred solution, has a χ^2 less than or equal to this value. In other words, this probability represents our percentage confidence that any structure seen in the solution corresponding to this χ^2 is necessary to fit the data and therefore

will also be present in the preferred solution. It gives the percentage confidence one can have that no noise is being fitted. On this basis, a confidence limit of 0.75 on a data set consisting of N=100 points requires the upper boundary of χ^2 to be at 109. In practice we use a confidence limit of 0.99 in order to be 99% sure that the solution structure seen is necessary to fit the data and no noise artifacts are present. To determine this 99% confidence solution the smoothing parameter μ is initially set to a large value and is then decreased until the χ^2 misfit of the solution falls just within the 0.99 confidence limit boundary.

The CONTIN algorithm, on the other hand, determines the smoothing parameter differently. It calculates solutions for approximately 24 different μ values ranging from much under-smoothed to much over-smoothed solutions. An F-test (18) is then done on each solution to determine whether or not it adequately describes the data. The CONTIN algorithm allows all solutions to be viewed and the user then chooses the one he/she feels is best, based on the F-test results. This freedom prevents a fixed confidence limit from being established and if a low confidence solution is chosen some solution structure may not be required by the data but may be due to a fitting of the noise. This method is very user interactive allowing for much human bias.

2.3 Method

In the simulation test programme designed to evaluate T2LIN, the input relaxation time distributions S(T) were constructed so as to contain up to three linear Gaussian shaped components of equal amplitude. A typical simulated continuous relaxation time distribution with three components is shown in Fig. 2.2. The components are at 5 ms, 100 ms, and 500 ms respectively. Each of the Gaussian components was synthesized using the following equation:

$$S_l(T) = \frac{1}{\sigma_l\sqrt{2\pi}} \exp\left(\frac{-(T-T_{lmean})^2}{2\sigma_l^2} \right) \quad \text{with} \quad l = \text{A, B, or C} \quad . \tag{2.14}$$

The standard deviation σ_l of the l^{th} component was defined such that the full width at half maximum (FWHM) was equal to 20% of the component's mean relaxation time. This width proportion was chosen to reflect the findings of experimental transverse relaxation time studies of garfish nerve cords. In order to simulate the raw

magnetization decay data, each component in the distribution was digitized into approximately 100 logarithmically spaced elements whose relaxation times extended from $T_{l\min}$ to $T_{l\max}$ where

$$T_{l\min} = T_{l\mathrm{mean}} - 3.25\,\sigma_l\,, \qquad l = \mathrm{A, B, or C}$$
$$T_{l\max} = T_{l\mathrm{mean}} + 3.25\,\sigma_l\,, \qquad l = \mathrm{A, B, or C} \qquad (2.15)$$

The value of $3.25\,\sigma_l$, takes each component out to 0.5% of its maximum amplitude. This type of digitization was chosen to satisfy the following objectives. First, we wanted to display the input spectra, as well as the resulting spectra calculated using T2LIN, on a logarithmic scale because the relaxation time distribution ranged over three decades of time. Secondly, we wanted to define each component with the same number of digitized elements. To facilitate this digitization, the spacing of the relaxation time grid points, T_g, was set to 0.002 log divisions which is exactly 10 times finer than the relaxation time grid utilized by T2LIN. Thus the amplitude of each component, Amp_l, was defined by the discrete sum

$$Amp_l = \sum_{T_g=T_{l\min}}^{T_{l\max}} S_l(T_g) \qquad \text{with} \qquad l = \mathrm{A, B, or C}\,, \qquad (2.16)$$

with the total spectrum amplitude normalized to 100.

To simulate a transverse relaxation time spin echo experiment, the magnetization decay curve was calculated at 1 ms time intervals from 1 ms to 2 s in the following manner:

$$M(t_i) = \sum_{l=\mathrm{A,B,C}} \sum_{T_g=T_{l\min}}^{T_{l\max}} S_l(T_g)\exp(-t_i/T_g) \qquad i = 1,2,\ldots,2000\,. \qquad (2.17)$$

Zero mean Gaussian noise was added to the entire data set, with the signal-to-noise ratio (SNR) being determined by dividing the magnetization at t_1 = 1 ms by the standard deviation of the noise, σ_n. For all simulations involving variations in SNR, the SNR values were incremented from 30,000 down to 100 in logarithmically spaced intervals.

In all the simulation studies where the number of magnetization decay data points was kept constant, the large set of 2000 decay data points was reduced to a subset

of a more manageable size for T2LIN, by sampling a maximum of 100 linearly spaced points per decade. This gave 100 points from 1 ms to 100 ms spaced at 1 ms intervals, 100 points from 100 ms to 1000 ms spaced at 9 ms intervals, and a final 12 points from 1000 ms to 2000 ms spaced 90 ms apart resulting in a total data set consisting of 212 points. This type of sampling is similar to that done with our experimental transverse relaxation decay data. If instead, 212 points were to be derived from a perfectly linear sampling from 1 ms to 2 s, then the short time components would be relatively under-sampled. On the other hand, a perfectly logarithmic sampling to give ~200 points from 1 ms to 2 s was impossible because magnetization decay data points could not be sampled more densely than every 1 ms at short times. The form of sampling used was chosen as the best compromise since it samples the short time end of the spectrum as densely as possible and still gives adequate sampling at long times. Fig. 2.3 is a plot of the 212 point magnetization decay data set corresponding to the relaxation component distribution in Fig. 2.2. The decay is shown with noise to produce a SNR of 100.

The following is a discussion of the specific methodologies used in each simulation test.

2.3.1 Simulation to Test the Resolving Power of T2LIN.

In order to determine the ability of T2LIN to resolve two closely spaced Gaussian components, the input relaxation time distribution was constructed with three components: one at $T_A = 5$ ms to serve as a control, a second component with a variable mean relaxation time T_B, and a third fixed at $T_C = 500$ ms. The measure chosen to quantify the input peak separation, S, was a relative measure and was defined by

$$S = \frac{(T_C - T_B)}{(T_C + T_B)/2} = 2\frac{(F-1)}{(F+1)} \tag{2.18}$$

where F is the ratio of the longer relaxation time to the variable relaxation time. The measure chosen to quantify the resolution, R, was defined by

$$R = \frac{[(H_B - D) + (H_C - D)]/2}{(H_B + H_C)/2} = 1 - \frac{D}{H_{avg}} \tag{2.19}$$

where D represents the height of the dip between peaks while H_B and H_C are the vertical heights of peaks B and C, respectively. Fig. 2.4 depicts a typical partially resolved spectrum defining these parameters. Thus, a value of R =1 denotes complete resolution whereas R = 0 denotes no resolution at all. The variable component, T_B, was placed at 15 different peak times ranging from an order of magnitude less than 500 ms, to within a factor of 0.7 times 500 ms. The extremes of T_B, namely, 40 ms to 350 ms were chosen because they encompassed the extremes of resolution between the two peaks. For example, with T_B = 40 ms, resolution was complete even for the lowest SNR. With T_B = 350 ms, no resolution was detected even for the highest SNR tested.

2.3.2 Simulation to Test the Effects of Decreasing the Density of Data Points Within a Fixed Time Window.

Because the T2LIN solution became very sensitive to specific noise variations contaminating the data when the number of data points was decreased to small values, it was necessary to test a large number of data sets which differed only in their noise realizations. It therefore became necessary to determine the density of data points at which T2LIN becomes sensitive to different noise realizations and to determine if any consistent effects are present as the density is decreased. This was accomplished by doing a statistical evaluation of the data point density reduction effects with many different representations of the noise. N = 150 different noise representations was chosen as the cutoff for this statistical analysis because mean values of precision, accuracy, and resolution differed by no more than 1% when further data sets were tested.

All 150 magnetization decay data sets in this simulation test were generated from the same simulated relaxation time spectrum, $S(T_g)$, consisting of components at 100 ms and 500 ms, respectively. The standard deviation of the added noise, σ_n, was kept constant to give SNR = 500 for all data sets. This SNR value was chosen because it yielded intermediate resolution values of the two peaks. Thus each data set differed from the others only in the random selection of noise contaminating each data point. Each data set was then sampled logarithmically within a window from 75 ms to 1000 ms to give data sets ranging in numbers of data points from 256 down to 16. The 75 ms to 1000 ms window was chosen because this was the data window range determined by the simulation tests of section 2.3.3 to have a minimal adverse effect on the T2LIN solution.

For data sets with the same number of data points, the corresponding T2LIN distributions were statistically analyzed to give mean and standard deviation values for resolution of peaks, precision of component widths, and accuracy of peak relaxation times. The entire analysis was also repeated for SNR = 250.

2.3.3 Simulation to Test the Effects Upon Fixed Relaxation Time Components of Restricting the Time window of Data Acquisition.

The outcome of the T2LIN analysis can be influenced either by reducing the maximum of the time domain data window, t_N, or by increasing its minimum, t_o. To test for the effects of the first constraint, relaxation time components at T_A = 5 ms (for control) and T_B = 500 ms were simulated and the 212 point magnetization decay data set calculated. This set was then progressively truncated to give decreasing data time window maxima from 2 s down to 50 ms, while the minimum of the data window was held fixed at 1ms. The ratio of the upper boundary of the data window to the longest relaxation time in the input distribution, t_N/T_B, was chosen as the measure of the degree of truncation. Eleven truncation values ranging from 4 down to 0.1 were tested at each of 11 different SNR values from 30000 down to 100. In this test the 5 ms component was included to serve as an indicator of the effects of SNR alone, while the effect of data window truncation and SNR upon the 500ms component were determined. The relaxation time of 500 ms was chosen to represent the typical long T_2 peak in the transverse relaxation time distributions found in tissue.

The effect of increasing the lower boundary of the data window, t_o, was evaluated in a similar manner. However, in this case relaxation time components were placed at T_A = 25 ms and T_B = 500 ms. The 500 ms component served as the control this time while the 25 ms component, which was chosen to reflect the typical short T_2 peak in experimental transverse relaxation time distributions found in tissue, was analyzed for window truncation effects. The ratio of the lower boundary of the data window to the shortest relaxation time in the input distribution, t_o/T_A, was used as the measure of truncation. Eleven truncation values ranging from 0.04 to 4, which corresponded to t_o times of 1 ms to 100 ms, were each tested over a range of SNR values from 30000 to 100. The truncation of the time window at both upper and lower edges degraded output spectral components in two ways: by increasing their width and

by decreasing their amplitude. Therefore the parameter used to quantify these effects was the following

$$P = \frac{\text{Output Amplitude}}{\text{Input Amplitude}} \times \frac{\text{Input FWHM}}{\text{Output FWHM}} \qquad (2.20)$$

where P was the symbol chosen to represent the precision of the output T2LIN spectra. Any decrease in amplitude or increase in width, relative to input values, resulted in a decreased P value. It should be noted that (output amplitude)/(input amplitude) remained constant at a value of 1 for all degrees of truncation of the upper window edge, while in the case of truncation of the lower window edge it only contributed to a decrease in precision when the degree of truncation became greater than ~2.

2.4 Results and Discussion

2.4.1 Simulation to Test the Resolving Power of T2LIN.

A three dimensional representation of the resolution, R, of two closely spaced components versus both component separation, S, and SNR is presented in Fig. 2.5 for the case where the confidence limit is 99%. This figure comprises three main regions: 1) a dark grey region representing no resolution, R=0, 2) a light grey region representing complete resolution, R=1, and, 3) a grey-scaled transition region between the two extremes, $0<R<1$. As one traverses this surface along lines of constant SNR, it is clear that resolution is lost in the transition region over a relatively small range of relative peak separation values. For example, Fig. 2.6 shows the resulting T2LIN spectra at SNR = 1000 as the relative peak separation, S, is varied within the transition region from 1.08 to 0.685 .

To illustrate the loss of resolution as SNR decreases, Figs. 2.7(a) and (b) show the set of T2LIN spectra for two fixed relative peak separations of S =1.2 and S = 0.67, respectively, as the SNR is varied through the transition region. Note that the transition region range in SNR values is much smaller for S =1.2 than it is for S = 0.67.

When the confidence limit is decreased to 75%, less smoothing and therefore apparently greater resolution results. The dotted lines in Fig. 2.5 at SNR = 30,000 and SNR = 100 show the shift in the transition region due to the change in confidence

limits. At a confidence level of 75%, there is a 25% chance that some noise is being fitted, a fact which could result in small noise artifact peaks in the solution spectra. In practice we choose to use a confidence limit of 99% in order to be very sure that we were not fitting any of the noise. (N.B. when the dotted lines at 75% were computed for Fig. 2.5, no small noise artifact peaks were in fact detected)

Our objective in plotting the surface of Fig. 2.5 was to determine how experimentally achievable SNR values limit T2LIN's resolving ability. For example, in the in-vivo situation, SNR values are usually of the order of 100, in which case T2LIN's resolving ability is severely restricted, requiring a minimum relative peak separation of approximately 1.35 to achieve $R > 0$. In-vitro, the limitations in SNR are not nearly so severe, with values of the order of 1000 or more being readily achievable. For example, the star on Fig. 2.5 indicates the region corresponding to our in-vitro transverse relaxation time studies on nerve cords, which are reported in detail in Chapter 3. We were typically able to achieve a SNR of approximately 3000, which allowed resolution of nerve water components with relative peak separation values greater than 0.8.

Although Kroeker and Henkelman (5) simulated delta-function distributions and not continuous distributions of relaxation times as we have, a comparison of our results to theirs is still of interest as it will indicate whether or not the resolving power of T2LIN is similar to that of another linear inverse algorithm. We would also like to compare our results to those of Brown (14) to determine whether or not T2LIN is providing the proper amount of information given the noisy data. To facilitate these comparisons Fig. 2.8 was constructed. It plots the threshold SNR against relative peak separations for four different data sets. The first two sets of data represent T2LIN's resolving power at 99% confidence. These two curves correspond to the lines of intersection between the surface of Fig. 2.5 and two horizontal planes at $R = 0.5$ and $R = 0.01$, respectively. The third set of data corresponds to Kroeker and Henkelman's results for a component amplitude ratio of $A/B = 1$. The final set of data represents Brown's prediction that the minimum SNR necessary to distinguish two components will be given by $1/(E_2\sqrt{N/8})$ where E_2 is given in Eq. 2.1 and N is the number of data points, ~200 in our case. This figure illustrates that CONTIN's definition of resolving power is comparable with $R = 0.5$ for T2LIN at 99% confidence. It also indicates that the lower limit of T2LIN's resolving capabilities, represented by the $R = 0.01$ curve at 99% confidence, corresponds to Brown's expected limitations. Therefore we can be confident that T2LIN is not yielding more information, in terms of resolving continuous distribution components, than is allowable by the noisy data.

Neither Kroeker and Henkelman, nor Brown have considered continuous distributions of relaxation times which comprise multiple Gaussian components as we have done, and therefore, they have not determined how differences in component widths can affect resolution. The simulation study presented here has been done with the input FWHM for all peaks equal to 20% of their peak relaxation time. This width was chosen to correspond approximately to those found experimentally in our transverse relaxation time analysis of garfish nerve cords. As this intrinsic width increases, resolution values for a given peak separation will decrease and the vertical face of Fig. 2.5 will shift to higher S values. Conversely, if the widths are reduced the vertical face will shift to lower S values. For example if the input FWHM is increased to 40% , the face shifts to higher S values by 0.13 units at SNR = 3,000 and by 0.06 units at SNR = 100. The shift is less at smaller SNR values because the peaks are already broadened by the lower SNR. Alternatively, if the input FWHM is decreased to 10%, the face shifts to lower S values by 0.03 units at SNR = 3000 and by 0.02 units at SNR =100.

2.4.2 Simulation to Test the Effects of Decreasing the Density of Data Points Within a Fixed Time Window.

When the number of data points becomes small the averaging capabilities of the algorithm are substantially compromised and T2LIN becomes more sensitive to individual noise excursions. Even with 256 data points the mean values of the resolution parameter, R, has a standard deviation of 7% brought about by its sensitivity to individual noise representations. The increase in sensitivity as the number of data points decreases is illustrated in Figs. 2.9(a),(b), and (c), where twenty-five T_2 spectra for data sets consisting of 256, 64 and 16 points, respectively, are plotted. The effects upon resolution, precision, and accuracy of decreasing the number of data points in a fixed time window are shown in Figs. 2.10(a), (b), and (c), respectively. All points in these figures represent the means of solution spectra from 150 data sets differing only in the representation of their noise while keeping σ_n fixed. For the resolution, R, and precision, P, these means are seen to decrease gradually as the number of data points is varied from 256 down to 16. The error bars represent the standard deviations brought about by the different noise representations. The growth in the standard deviation due to noise, as the number of data points is reduced, demonstrates the increasing sensitivity

to noise representations. Mean values for fewer than 16 data points could not be determined because the T2LIN algorithm tended to become unstable and had problems converging upon a solution.

Some accuracy in determining the peak relaxation times is also lost as the number of data points is reduced from 256 to 16. In Fig. 2.10(c), the standard deviations of the mean peak relaxation times increase from 2 to 10% of the mean peak times.

Before the SNR$\sqrt{N}$ relation suggested by WBH (1) and Brown (14) can be addressed, it must be stressed that neither of these two groups defined a quantitative measure for resolution. Therefore the SNR$\sqrt{N}$ relation can only be used in a general sense to compare different combinations of SNR and N at a fixed level of resolution. To determine how closely the output of T2LIN follows this general relation, the resolution, R, was plotted against the number of data points, N, for data sets at SNR = 500 and SNR = 250 in Fig 2.11. The dotted line represents the four-fold increase in N, predicted by the SNR$\sqrt{N}$ relation, required to achieve the same resolution at half the SNR. Note that the predicted and experimental curves for SNR = 250 do not coincide, however, they do agree within the standard deviations. This indicates the importance of taking into consideration the sensitivity of an inversion algorithm to differences in the noise representations.

This statistical evaluation of T2LIN has shown that resolution, precision, and accuracy are somewhat degraded as N is reduced from 256 down to 16. At SNR = 500 resolution drops by R = 0.4 units in the transition region. The precision decreases by P = 0.08 units, and peak relaxation times vary by 5%. The most significant result of these tests is the sensitivity of T2LIN to noise variations. Even at N = 256, resolution varies by ±7%, and precision by ±20%. At N =16 these deviations increase to ±50% for resolution, ±25% for precision, and ±5% for peak relaxation times.

2.4.3 Simulation to Test the Effects Upon Fixed Relaxation Time Components of Restricting the Time Window of Data Acquisition.

Constraining the maximum or minimum limiting values of the data acquisition time window affects the output of T2LIN in ways that are illustrated in Figs. 2.12(a) and (b) for various SNR values. Both figures clearly show that SNR is a far more important determinant of precision than are window limitations. Recall that the product of the

output component amplitude and the inverse of the output component width (both taken relative to input values) was the quantitative measure chosen to define the precision, P. The large dependence of precision upon SNR is visualized in Figs. 2.7(a) and (b) where the control peak at 5ms shows a 4-fold increase in width as the SNR is varied from 17500 down to 125. Examples of the loss of precision brought about by the proximity of the edge of the data acquisition window at a fixed SNR of 1000 can be seen in Figs. 2.13(a) for truncation of the lower edge, and 2.13(b) for truncation of the upper edge. Numerous spectra such as these were analysed at all levels of SNR to provide the data plotted in Figs. 2.12(a) and (b). Together, Figs. 2.12(a) and (b) enable one to estimate the effects of limiting the values of the time window for particular values of SNR. For example, for SNR=100, a data set ranging in time from 0.75 times the relaxation time of the shortest peak to twice the relaxation time of the longest peak gives the best possible precision achievable at that SNR, namely $P = 0.2$.

Because truncating the data acquisition window also reduces the number of data points, it is important to establish that the effects attributed to the truncation of the data window are due solely to this truncation and not the overall decrease in data points. This was accomplished by measuring the variations in the control peaks. It was found that the widths of the control peaks varied by less than 10% while their amplitudes and peak times remained accurate to within 5% of input values over the entire range of truncation. These variations are small compared to the changes seen in the degenerated components closest to the truncated window edge, confirming that the measured effects upon precision are correctly attributed to the truncation of the data window. See Fig. 2.13(a) and (b). Although the components closest to the truncated window edge degenerated in terms of component width, the accuracy of their peak positions remained very good for $P > 0.2$, usually within 5% of input values. As well, the amplitude of the 500ms component remained within 5% of the input amplitude right up until the component was almost completely degraded, while the amplitude of the degenerating 25ms peak decreased due to the fact that the initial time points required to determine the proper amplitudes had been removed.

Once again the dotted lines in Fig. 2.12(a) represent the 75% confidence limit solutions. At a SNR of 100 this 75% confidence line shows a 15% increase in precision.

A marked inconsistency between the work of Kroeker and Henkelman on the CONTIN algorithm and that presented here, relates to the dependence of the precision, P, on SNR. Kroeker and Henkelman , whose data acquisition window corresponded to

$t_o/T_A = 0$ and $t_N/T_B = 8$, found only a 50% increase in component width as SNR decreased from infinity down to 100, whereas we found, for our largest data acquisition window, a 300% increase in component width as SNR decreased from 30,000 down to 100. Although T2LIN and CONTIN have many differences as explained earlier in this chapter, the most probable cause of this inconsistency is the fact that CONTIN and T2LIN choose their smoothing parameters differently. For instance as the SNR decreases, the amount of noise that is fitted by the non-smoothed solution increases. Therefore in order to maintain the same amount of confidence that no noise is being fitted, the degree of smoothing must necessarily increase, creating broader peaks. Since CONTIN shows no broadening of component widths as SNR decreases, it cannot be maintaining the confidence level at a fixed value as we do with T2LIN. The F-test performed by CONTIN determines whether or not a solution adequately fits the data. Many of CONTIN's generated solutions pass this F-test criterion, providing the user with a set of adequate solutions which vary in their degree of smoothing and in their corresponding confidence limits. This method gives the user a lot of influence over the solution and fails to maintain the confidence limit. It is better to keep the confidence limit fixed at a large value, which T2LIN does at 0.99, because this provides a consistent set of solutions with the same high level of confidence that any structure present is real and necessary to fit the data, and leaves no room for human bias. This consistency is necessary if any comparison between spectra is to be made.

2.5 Conclusion

In this chapter we have evaluated, through simulation studies, the effects of limitations in SNR, data acquisition windows, and the number of data points upon our linear inverse continuous distribution algorithm, T2LIN. First, we have determined the minimum SNR requirements to resolve two Gaussian relaxation time components at various peak separations, emphasizing the restrictions in SNR characteristic of the in-vivo and in-vitro experiments. We found that T2LIN was comparable to CONTIN and did not resolve more than what was allowable by the data. Secondly, the reduction in resolution, brought about by a decrease in the number of data points, N, was not as drastic as predicted by the $SNR\sqrt{N}$ relation. However, the large standard deviations due to T2LIN's sensitivity to differences in the noise representations, allowed agreement between our results and this relation, emphasizing the importance of determining such

sensitivities. The precision and accuracy of solution spectra were affected, as well, by the reduction in N, but once again the large standard deviations allowed solutions corresponding to a small number of data points to show comparable precision and accuracy to solutions corresponding to larger N. We found 16 data points to be the minimum acceptable by T2LIN since any fewer than this had a tendency to cause the algorithm to break down.

Finally, the effects of restricting the limits in time of the data window upon fixed relaxation time components were presented. We found threshold values for the positions in time of the maximum and minimum edge of the data window at which degradation in T2LIN's precision began to occur. These threshold values varied somewhat between different levels of SNR but typically a maximum in time of twice the longest component and a minimum in time of half the shortest component provided a sufficient data window to achieve the best possible precision attainable at a given SNR. As SNR decreased, it was found that T2LIN's precision decreased continuously as well and therefore only relative widths can be determined by T2LIN. This point emphasizes the importance of maintaining a fixed confidence level for solutions in order to achieve consistency.

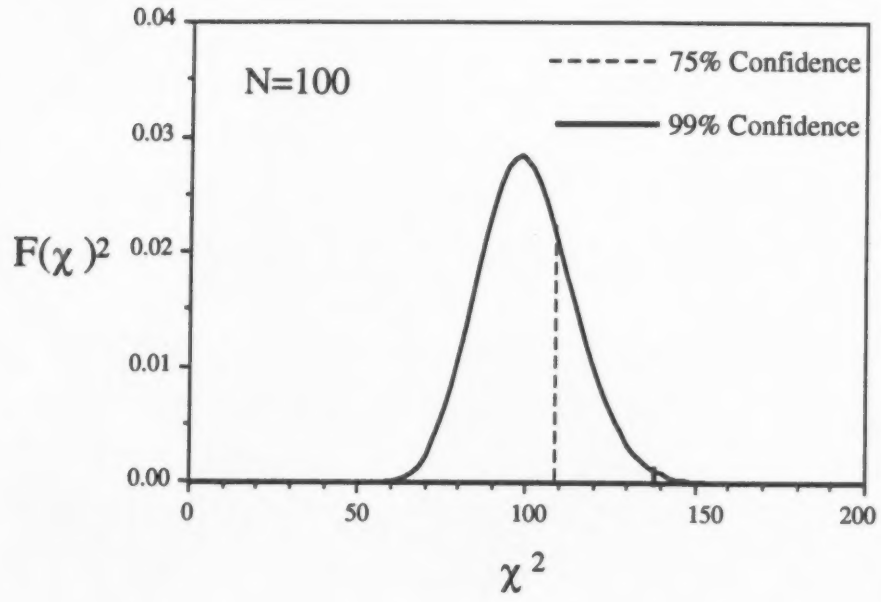

Figure 2.1 Frequency distribution of the chi-square statistic for N = 100. The area under the curve to the left of a specified chi-square value represents the percentage confidence that the smoothed solution corresponding to that specified chi-square value shows the structure necessary to fit the data but no noise artifacts.

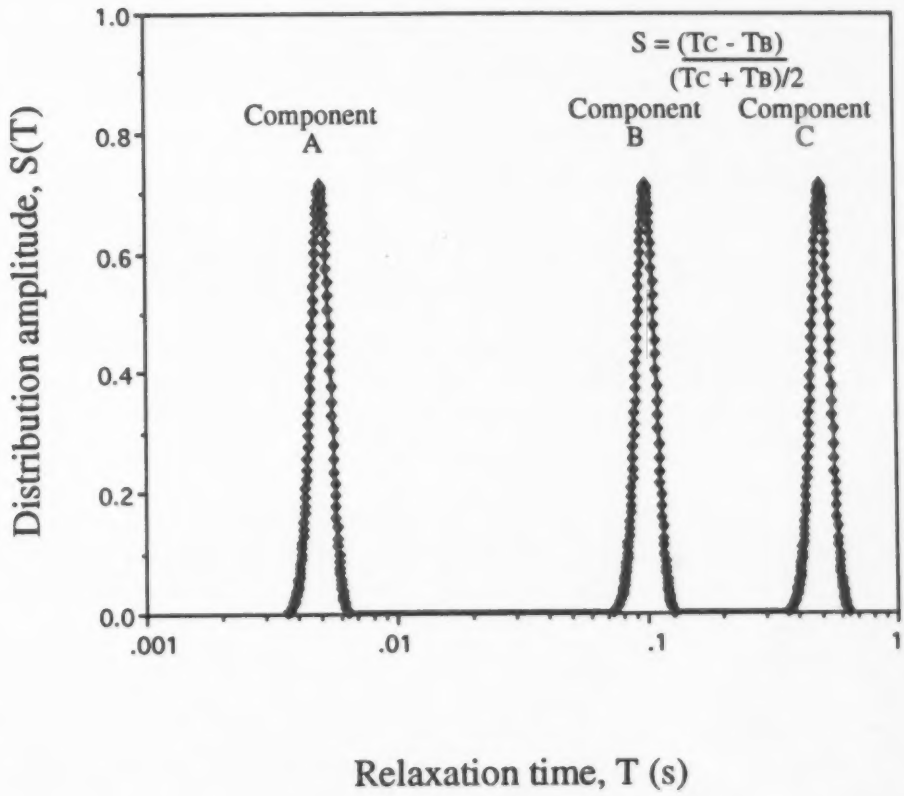

Figure. 2.2. Simulated continuous relaxation time distribution consisting of components A, B, and C at mean relaxation times of 5 ms, 100 ms, and 500 ms, respectively. All components have a FWHM of 20% of the mean component relaxation time, and all components contribute equally to the total magnetization. S defines the relative measure chosen to quantify the input peak separation.

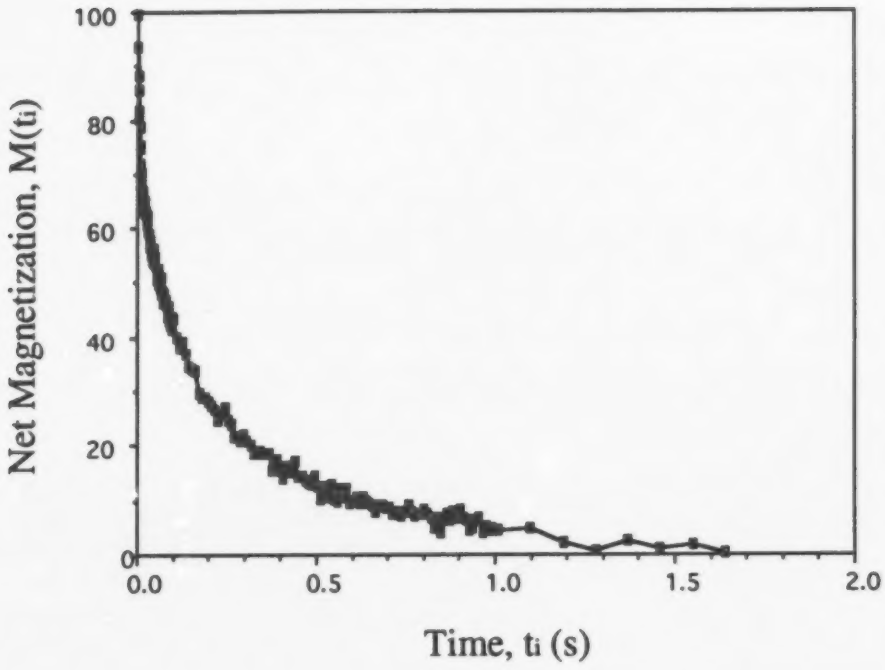

Figure 2.3. Magnetization decay data set corresponding to the relaxation time distribution of Fig. 2.2 with zero mean, Gaussian noise added to yield a SNR of 100. This data set contains a maximum of 100 linearly spaced points per decade with 100 points from 1 ms to 100 ms spaced at 1 ms intervals, 100 points from 100 ms to 1000 ms spaced at 9 ms intervals, and a final 12 points from 1000 ms to 2000 ms spaced 90 ms apart. In this case the decay does not extend out to 2 s because it is cut off when the magnetization falls below the noise level.

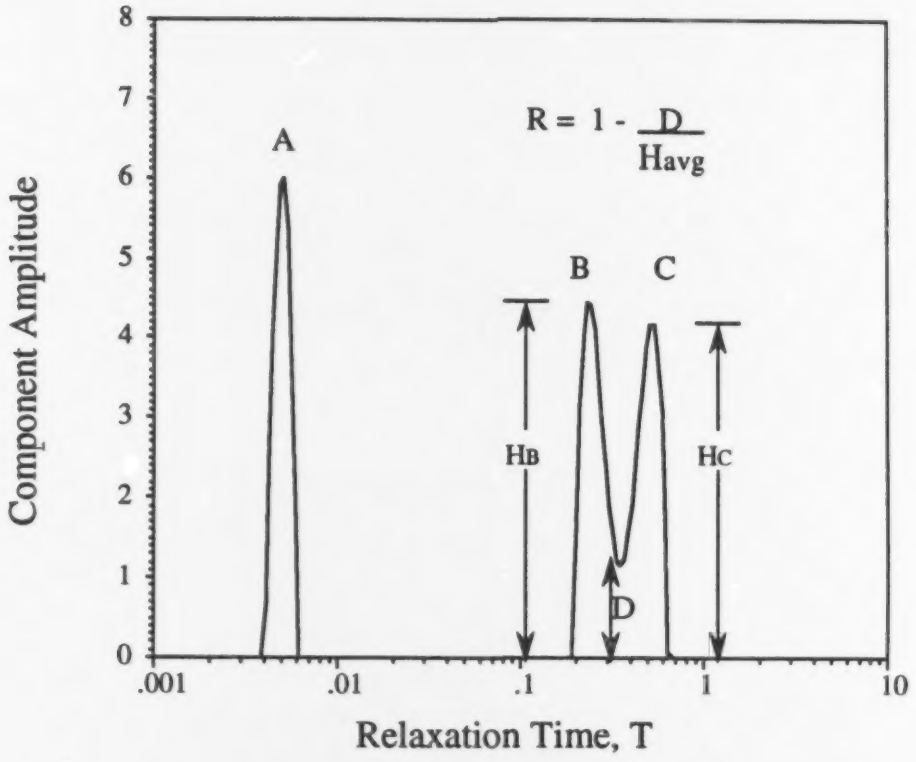

Figure 2.4. A typical, partially resolved, relaxation time spectrum defining the parameters used to quantify the resolution, R. In this example components B and C have a resolution value of R = 0.74.

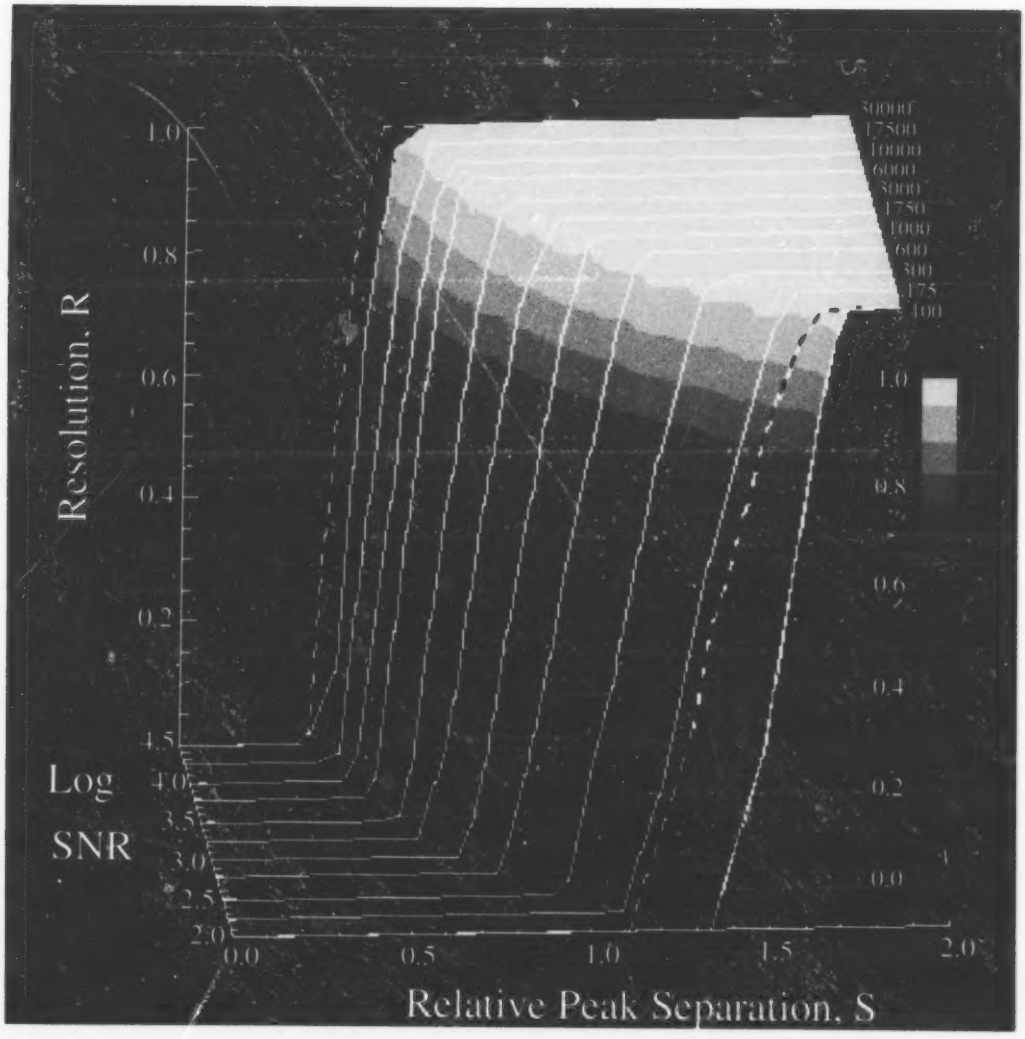

Figure 2.5 The resolution of two closely spaced components versus both component separation and SNR. The resolution, R, is defined as one minus the ratio of the dip height to the average peak height (see Fig. 2.4). The relative peak separation, S, is defined by the ratio of the difference in the peak relaxation times to their mean (see Fig. 2.2). The star on the figure indicates the typical SNR (3000) achieved in our in-vitro transverse relaxation time studies on nerves which allowed complete resolution of components with peak separations greater than 0.8. The dotted lines represent the 75% confidence limit solutions at SNR of 30000 and 100.

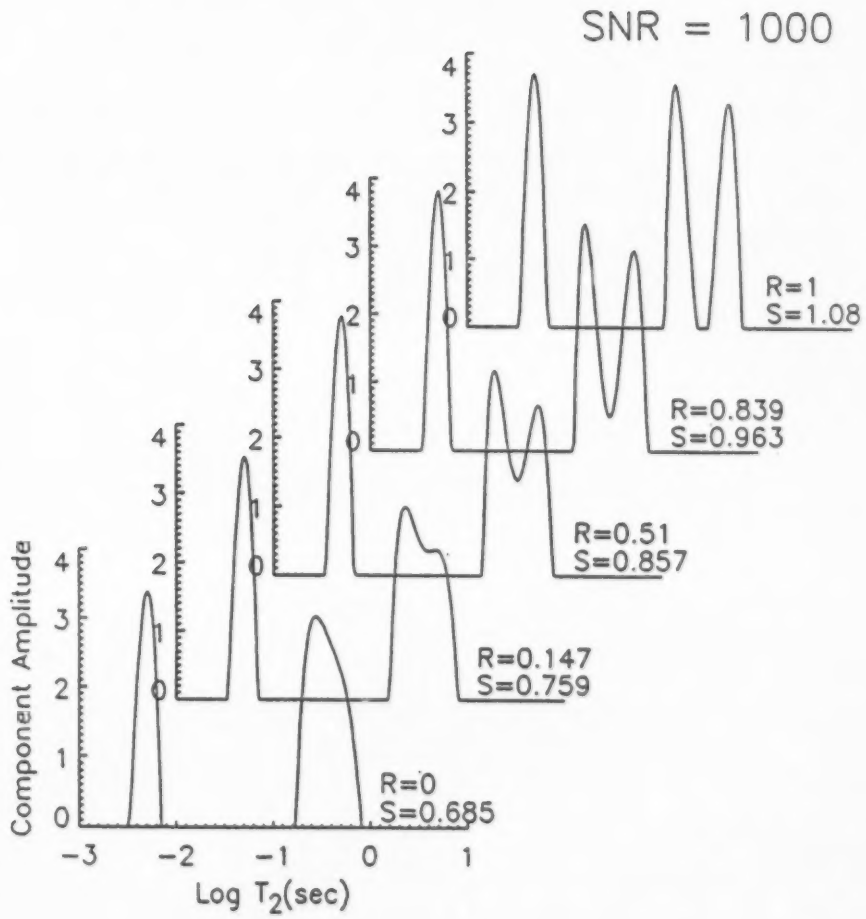

Figure 2.6. T2LIN spectra at a SNR of 1000 showing the change in resolution, R from the extreme of no resolution to that of complete resolution, as the relative peak separation, S, is increased from 0.685 to 1.08.

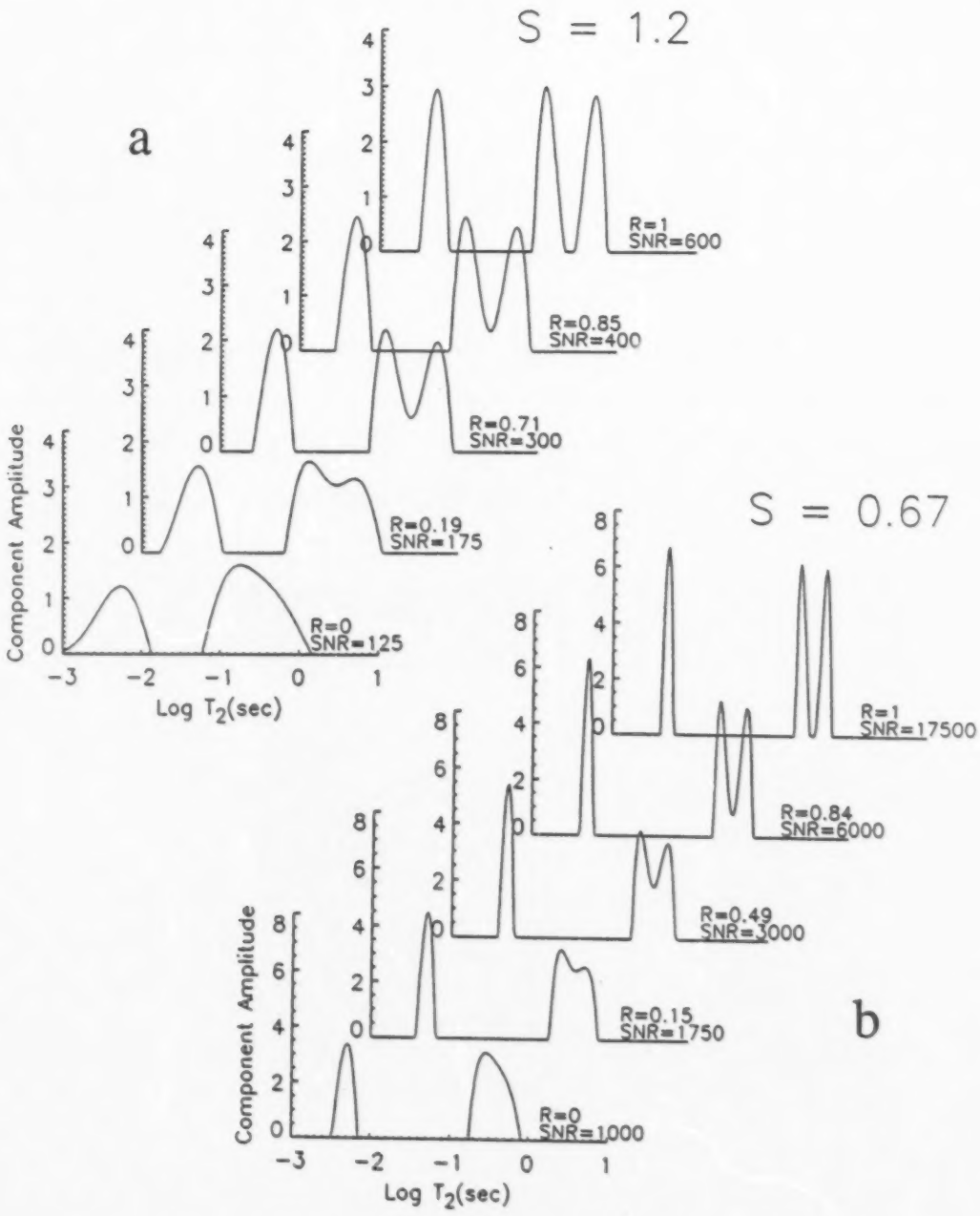

Figure 2.7. T2LIN spectra corresponding to fixed relative peak separations of (a) S = 1.2, and (b) S = 0.67 as the SNR is varied through the transition region. Note the smaller transition region range in SNR values with a larger peak separation of S = 1.2.

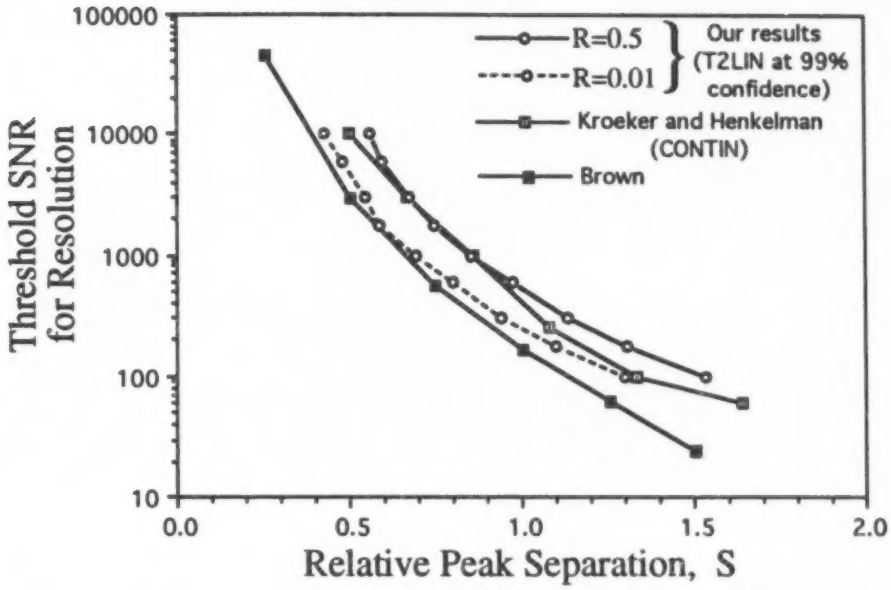

Figure 2.8. Comparison of threshold SNR versus relative peak separation,S, as determined by three different groups. Recall that S is defined by the difference in peak relaxation times divided by their mean, see Fig. 2.2. Brown's results represent his mathematical estimation that the minimum SNR required to distinguish two components, discrete or continuous, is given by $1/(E_2\sqrt{N/8})$, where E_2 is defined in Eq. 2.1, and N = 200 in this case. The curve defining Kroeker and Henkelman's results corresponds to their measurements of CONTIN's ability to resolve two discrete components of equal amplitude. These resolution measurements were all or none, with two components being considered resolved when the resolution showed two peaks with relaxation times within 100ms and amplitudes within 10% of input values. Our results represent T2LIN's ability at 99% confidence to achieve R = 0.5 and R = 0.01 respectively for two Gaussian components with widths equivalent to 20% of their means.

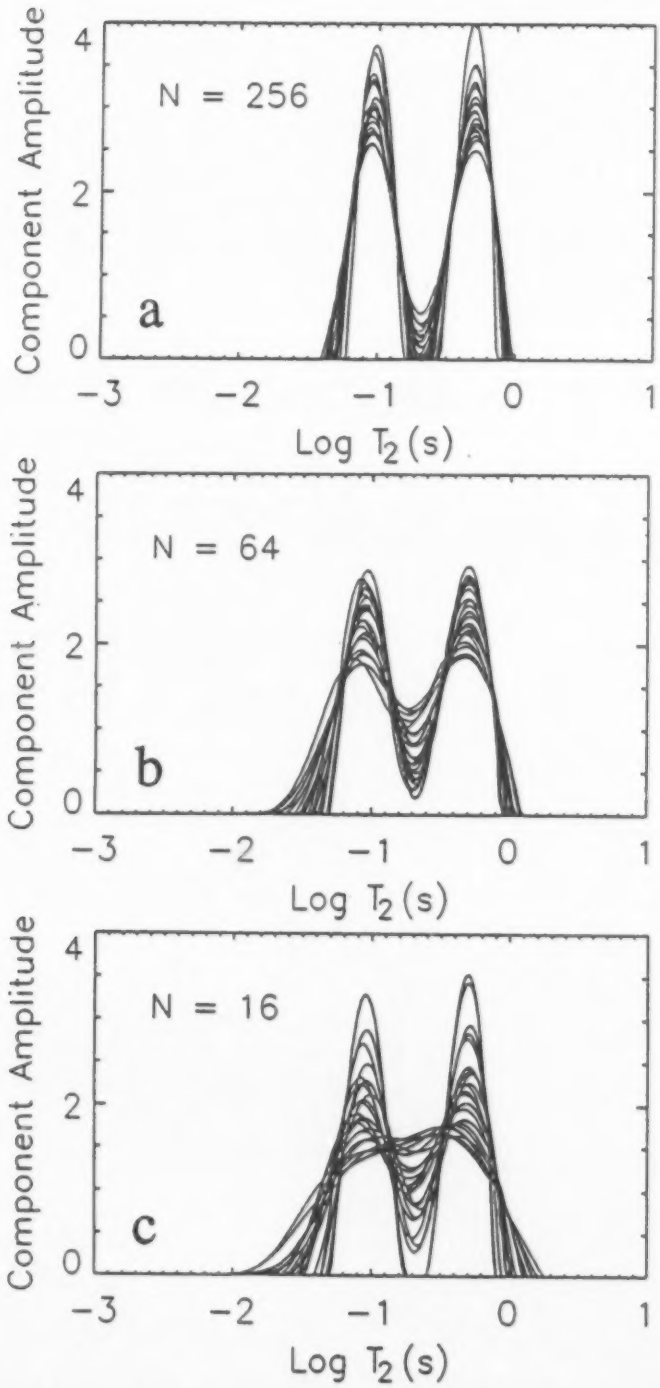

Figure 2.9. Variations in T2LIN spectra caused by changing the representation of the noise. Each figure shows twenty-five T2 spectra for data sets consisting of (a) 256 data points, (b) 64 data points, and (c) 16 data points.

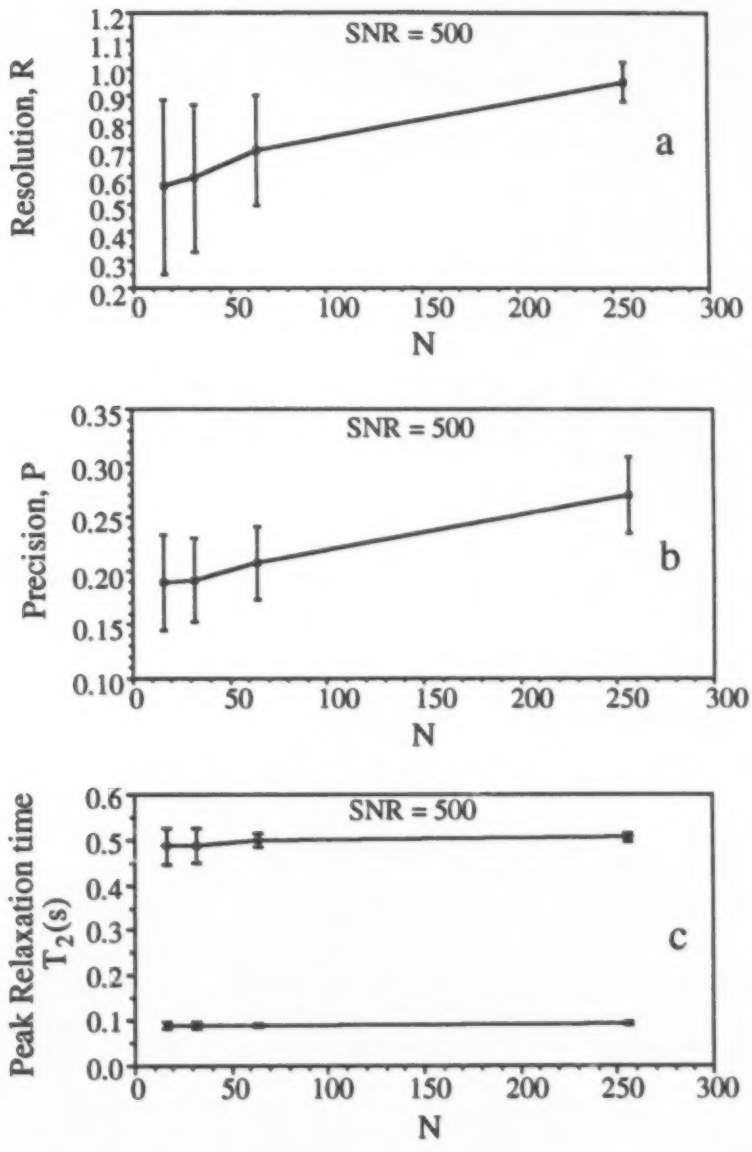

Figure 2.10. **(a)** Resolution , R, **(b)** precision, P, and (c) accuracy of peak relaxation times, T_2 , versus the number of data points within a time window from 75 ms to1000 ms. All points represent the mean and standard deviation values of solution spectra from 150 data sets differing only in the representation of their noise at a constant σ_n .

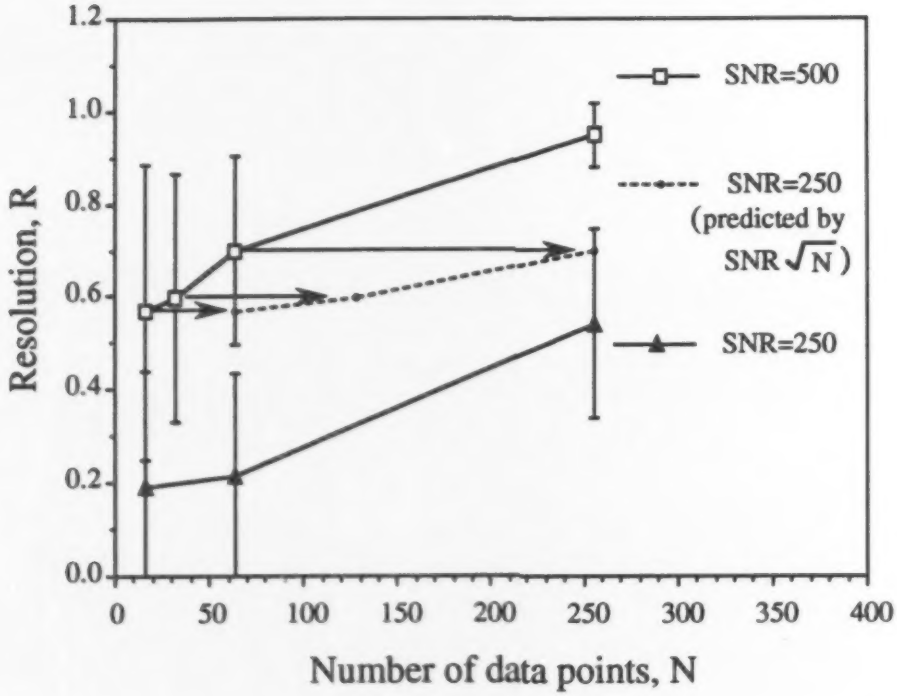

Figure 2.11. Resolution, R, versus the number of data points, N, at SNR = 500 and SNR = 250 (true and predicted). Points on the solid lines represent the mean and standard deviation values of solution spectra from 150 data sets differing only in the representation of their noise at a constant σ_n. The dotted line represents R versus N for SNR = 250 predicted by the SNR$\sqrt{N}$ relation.

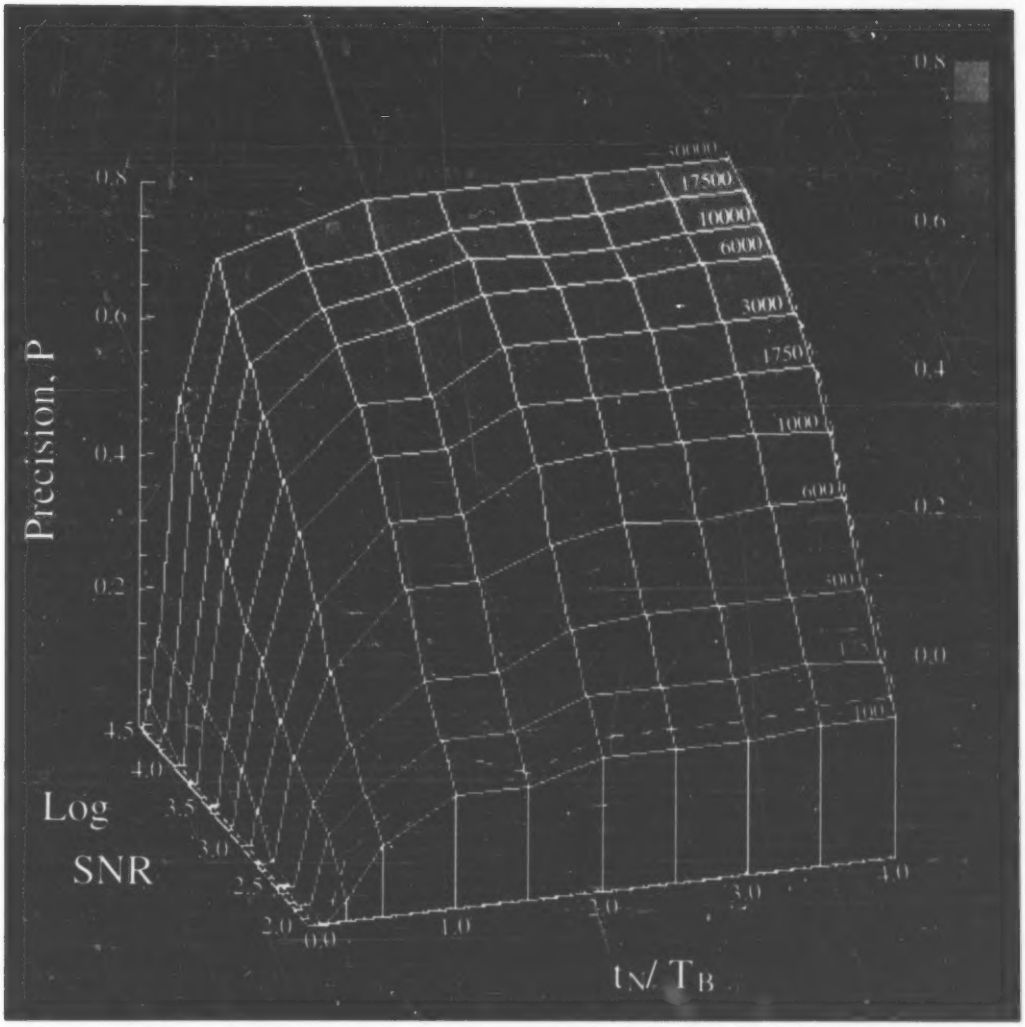

Figure 2.12(a) The precision, P, of a single relaxation time component at various SNR as the upper boundary of the data acquisition window, t_N, is brought into close proximity with the relaxation time, T_B, of that component. Note that for this figure (output amplitude/input amplitude) = 1 throughout. The closeness of approach of the upper cut off of the data acquisition window to the relaxation time of the component is determined by the ratio of these two values, i.e. t_N/T_B. The main figure surface represents solutions at the 99% confidence limit while the dotted lines denote solutions at 75% confidence.

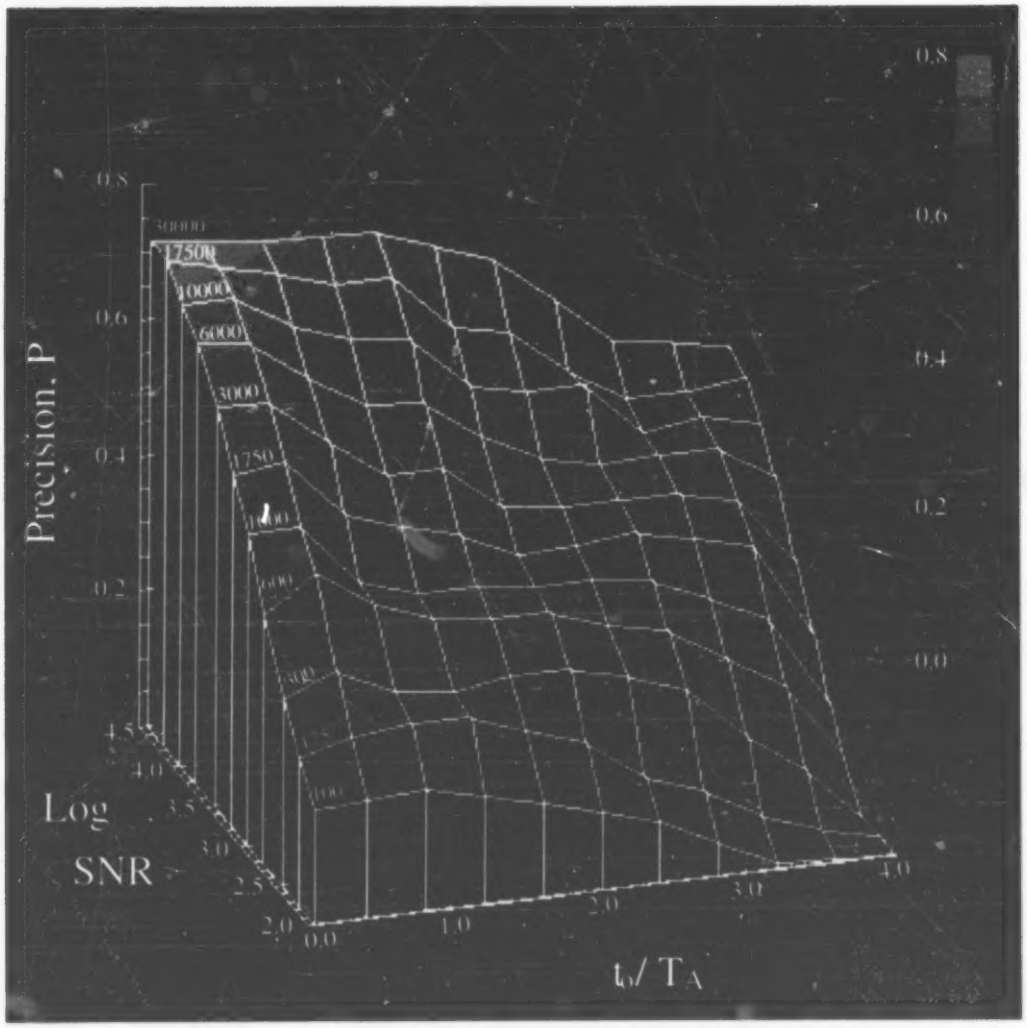

Figure 2.12(b) The precision, P, of a single relaxation time component at various SNR as the lower boundary of the data acquisition window, t_o, is brought into close proximity with the relaxation time, T_A, of that component. The precision is quantitatively determined by the product (output amplitude/ input amplitude)x(input FWHM/output FWHM). The closeness of approach of the lower cut off of the data acquisition window to the relaxation time of the component is determined by the ratio of these two values, i.e. t_o/T_A.

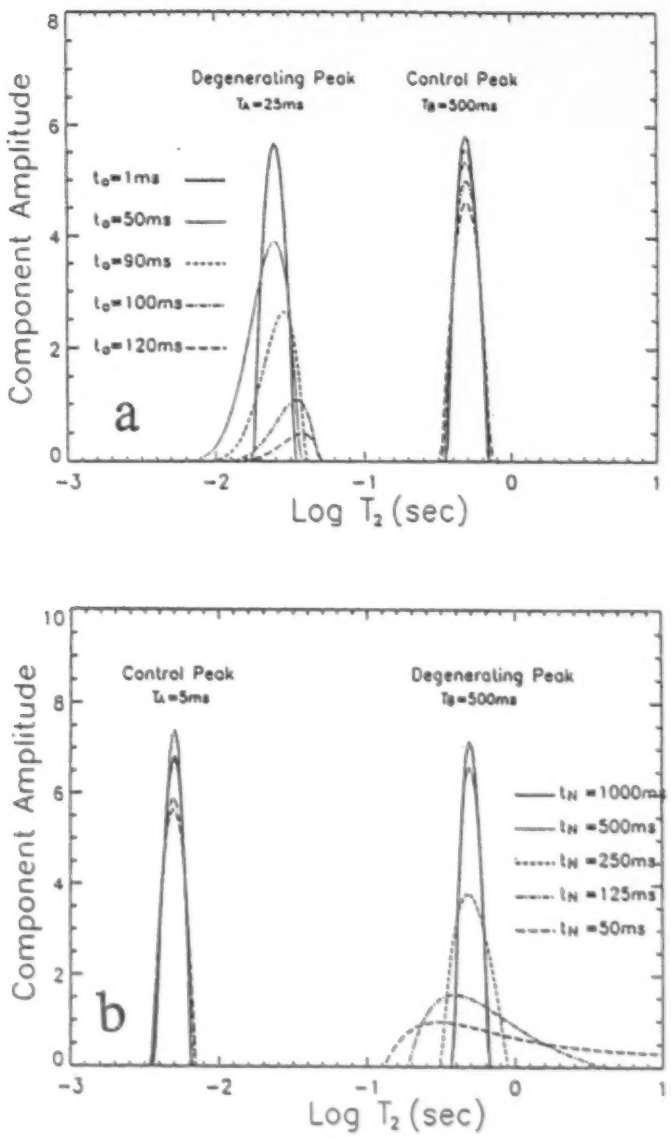

Figure 2.13. Examples of the degeneration of output components brought about by the proximity of (a)the lower boundary, t_o , and (b) the upper boundary, t_N, of the data acquisition window to these components. The SNR for these data sets is 1000.

2.6 References and Selected Bibliography

1. K. P. Whittall, M. J. Bronskill, and R. M. Henkelman, Investigation of analysis technique for complicated NMR relaxation data, *J. Magn. Res.* **95**, 221 (1991).

2. S. W. Provencher, A constrained regularization method for inverting data represented by linear algebraic or integral equations, *Comput. Phys. Commun.* **27**, 213 (1982).

3. S. W. Provencher, CONTIN, a general purpose constrained regularization program for inverting noisy linear algebraic or integral equations, *Comput. Phys. Commun.* **27**, 229 (1982).

4. K. P. Whittall and A. L. MacKay, Quantitative interpretation of NMR relaxation data, *J. Magn. Reson.* **84**, 134 (1989).

5. R. M. Kroeker and R. M. Henkelman, Analysis of biological NMR relaxation data with continuous distributions of relaxation times, *J. Magn. Reson.* **69**, 218 (1986).

6. R. M. Kroeker, C. A. Stewart, M. J. Bronskill and R. M. Henkelman, Continuous distributions of NMR relaxation times applied to tumors before and after therapy with x-ray and cyclophosphamide, *Magn. Reson. Med.* **6**, 24 (1988).

7. R. S. Menon and P. S. Allen, Application of continuous relaxation time distributions to the fitting of data from model systems and excised tissue, *Magn. Reson. Med.* **20**, 214 (1991).

8. R. S. Menon, M. S. Rusinko and P. S. Allen, Proton relaxation studies of water compartmentalization in a model neurological system, accepted *Magn. Reson. Med.* (1992).

9. W. A. Stewart, K. P. Whittall, D. W. Paty, Analysis of CPMG data from CNS tissue: a potential method for detecting demyelination in Multiple Sclerosis, 10th Annual SMRM Meeting, Abstract 85, (1991).

10. A. L. MacKay, K. P. Whittall, K. S. Cover, D. K. B. Li, D. W. Paty, Invivo T_2 relaxation measurements of brain may provide myelin concentration, 10th Annual SMRM Meeting, Abstract 917, (1991).

11. K. P. Whittall, Recovering compartment sizes from NMR relaxation data, *J. Magn. Reson.* **94**, 486 (1991).

12. A. E. English, K. P. Whittall, M. L. G. Joy, and R. M. Henkelman, quantitative two-dimensional time correlation relaxometry, *Magn. Reson. Med.* 22, 425 (1991).

13. C. L. Lawson and R. J. Hanson, "Solving Least Squares Problems", Prentice-Hall, Englewood Cliffs N.J., (1974).

14. R. J. S. Brown, Information available and unavailable from multiexponential relaxation data, *J. Magn. Reson.* **82**, 539 (1989).

15. G. E. Backus and J. F. Gilbert, Uniqueness in the inversion of inaccuarate gross earth data, *Phil. Trans. R. Soc. A* **266**, 123 (1970).

16. J. P. Butler, J. A. Reeds and S. V. Dawson, Estimating solutions of first kind integral equations with nonnegative constraints and optimal smoothing, *Siam J. Numer. Anal.* **18**, 318 (1981).

17. M. Abramowitz and I. A. Stegun, eds., "Handbook of Mathematical Functions With Formulas, Graphs and Mathematical Tables", Dover (1964).

18. J. T. McClave, F. H. Dietrich, "Statistics", 4th Ed., Dellen Publishing Company, San Francisco, (1988).

CHAPTER 3

Water Proton Transverse Relaxation Time Analysis of Myelinated and Nonmyelinated Nerves: A Simple White Matter Model.

3.1 Introduction

Magnetic resonance imaging (MRI) has proven very useful in the detection and diagnosis of various white matter diseases such as edema and demyelination. Since MRI depends upon differences in water proton relaxation times for contrast, a good understanding of water proton relaxation in white matter tissue is essential if the specificity of MRI is to be improved. At present normal and pathological tissues are characterized by single relaxation times and the contrast achieved is sufficient to allow easy detection of white matter lesions. However, within a lesion itself there is no contrast because of limits in contrast and resolution, and the relaxation characteristics of the microscopic compartments within a single tissue type are not known. This limits the diagnostic ability of MRI. For example, cytotoxic (intracellular) edema cannot be distinguished from vasogenic (extracellular) edema.

Because white matter, like all biological tissue, is a heterogeneous system, it most likely will be characterized by multiple transverse relaxation (T_2) components which correspond to different microscopic water compartments between which the exchange of water is limited. Changes in the relaxation times and proportions of these T_2 components, if experimentally quantifiable, can be used to detect changes in the compartmental structure in-vivo, thereby providing greater specificity in the diagnosis of white matter diseases of the brain which result from a breakdown of the microstructural architecture. In order to develop the use of multiple transverse relaxation in-vivo, a research program, of which this project is only a part, has been developed to improve the quantitative understanding of water proton relaxation in white matter tissue through the use of a series of increasingly complex model systems. The specific objectives of the research project described in this chapter were to investigate the water proton transverse relaxation time characteristics of a model white matter tissue system consisting of myelinated and nonmyelinated cranial nerves of the spotted garfish, and to assign the multiple T_2 components to specific water compartments in the nerves. The garfish was chosen for its olfactory nerve which contains the longest and most homogeneous

population of unmyelinated axons found in any vertebrate. The garfish also provides easily accessible myelinated nerves of both the peripheral and central nervous system.

Previous work on various white matter models (1,2) in our laboratory has firmly established the existence of compartmentalization giving rise to multi-component transverse relaxation. For example, for the three transverse relaxation components observed in the crayfish abdominal nerve cord, two were identified, one from the axonal water fraction (T_2 =197 ms, Pop = 59%), and another from the extra-axonal water fraction (T_2 = 639 ms, Pop = 32%), but the third component (T_2= 49 ms, Pop = 7%) was unidentified. With hindsight, the crayfish abdominal nerve cord was not the ideal tissue system for modelling white matter. It contained no myelinated axons and was not as simple a system as initially anticipated. It served therefore, to focus the project on its essentials by means of a cleaner model system, namely, one which would allow determination of the effect of myelin upon the transverse relaxation time distribution. Knowledge of the myelin contribution to the T_2 distribution is of utmost importance in the diagnosis of demyelinating white matter diseases.

The existence of multi-component transverse relaxation and attempts at associating these components with particular anatomical water compartments have also been documented for the frog sciatic nerve (3), in-vitro cat brain (4), and in-vitro guinea pig brain in experimental allergic encephalomyelitis (EAE) (5). In the case of the frog sciatic nerve three components with relaxation times (populations) of 17 ms (29%), 70 ms (50%), and 310 ms (21%) were ascribed to water associated with proteins and phospholipids (myelin), axoplasmic water, and extracellular water, respectively. The relaxation times of the axonal and extracellular water in the sciatic nerve are two to three times shorter than those of similar compartments in the crayfish abdominal nerve cord, while the ratio of axonal to extracellular populations is similar for the two nerves. The results of the cat brain and guinea pig brain studies were consistent. Both attributed a short time component at approximately 10 ms to water compartmentalized in myelin. This time is also consistent with the T_2 of the myelin component found in the frog sciatic nerve. In white matter of the cat this short T_2 component contributed 7% to the total water population while in guinea pig normal white matter it contributed substantially more, 20%. Both studies also assigned a second larger component at 80 to 100 ms to the intracellular water (consisting of axoplasm and glial cell cytoplasm). The populations of these longer components were 86% and 80% for the cat brain and guinea pig brain, respectively. These populations are much larger than the corresponding intracellular components in the sciatic nerve and crayfish abdominal nerve because of

the large amount of glial cell cytoplasm and lack of extracellular space in cat and guinea pig white matter. As well, the relaxation times of these intracellular components in the cat and guinea pig white matter are slightly larger than the T_2 of the axonal space in the frog sciatic nerve and a factor of 2 smaller than that of the axoplasm component in the crayfish abdominal nerve cord. The nerve tissues examined in these studies are all complex myelinated tissue systems and although each study has suggested a myelin component, it is not absolutely certain that a myelin component is identifiable. Because the garfish model includes a very homogeneous unmyelinated nerve it provides a simpler view of nerve tissue without the complicating effects of myelin. Comparison of the transverse relaxation time distribution of this nonmyelinated nerve to that of the myelinated nerves from the same species should provide an extra clue as to the myelin contribution.

The application of a multiple transverse relaxation time analysis in-vivo has recently been attempted (6) on normal and Multiple Sclerosis (MS) volunteers. The results were consistent with the in-vitro studies on cat and guinea pig brain described above. Two T_2 components were readily separable. The short component with a T_2 less than 60 ms and a population of 20% was assigned to the water associated with myelin. This component was found to be absent in grey matter and was reduced in amplitude in MS lesions. The longer T_2 peak at 80 to 100 ms corresponded to the remainder of the tissue water. If these assignments are correct, such T_2 measurements may enable quantitative in-vivo determinations of myelin concentration to be made. Thus it is apparent that a multiple relaxation time analysis has the potential to yield important diagnostic information and we, therefore, continue to seek a greater understanding of the physiological determinants of the transverse relaxation characteristics in white matter through the use of simple tissue models.

The model chosen comprised three different cranial nerves of the spotted garfish (Lepisosteus oculatus): the olfactory nerve, the trigeminal nerve, and the optic nerve. The spotted garfish (shown in Fig. 3.) is a fresh water fish found in lakes and river systems ranging from the Great Lakes, south to the Gulf Coast and east to western Florida (7). The garfish was chosen because its abnormally long snout contains olfactory nerves which are the longest, and most homogeneous source of nonmyelinated nerve axons found in any vertebrate (8). These olfactory nerves may be up to 20 cm in length in the long-nosed garfish, but were typically found to be 3 to 4 cm in the spotted gar. We would have preferred the long-nosed variety of the garfish, however, it was not available. Fish used in these experiments ranged from 26 cm to 34 cm in length.

The olfactory nerve of the garfish provided us with a simple model system, consisting mainly of nonmyelinated nerve axons. The two other cranial nerves, both myelinated, were chosen to extend the model to include myelin. The optic nerve which is part of the central nervous system (CNS) and myelinated by oligodendrocytes most closely resembles white matter. The trigeminal nerve, like the olfactory nerve, is part of the peripheral nervous system (PNS) and is myelinated with Schwann cells.

In the past these nerves of the garfish have been subjected to tests of their composition (9), degeneration (10), axonal transport (11), and electrical properties (12). As well, relaxation time measurements have previously been made on the optic and olfactory nerves (13), however, only single relaxation components were reported.

In this chapter, our first objective was to investigate the water proton transverse relaxation time distributions of the nonmyelinated olfactory, and myelinated trigeminal and optic nerves of the spotted garfish. To achieve this objective we used the continuous relaxation time distribution technique described in detail in Chapter 2 to analyze the magnetization decay data from all three nerves. The transverse relaxation time distributions showed multiple resolved components for all nerves while clearly distinguishing the myelinated from the nonmyelinated nerves due to the presence of an extra fast relaxing component in the case of the myelinated nerves. Our second objective was to assign these transverse relaxation time components to anatomical water compartments in the nerves. By comparison of the T_2 distribution amplitudes with proportions of water in the anatomical compartments derived from electron (EM) and light microscopy, we have assigned the major T_2 distribution components to intracellular, extracellular and myelin water, respectively, thus fulfilling our second objective. Knowledge of such correlations is the first step in utilizing changes in the transverse relaxation times and proportions of the T_2 components to detect in-vivo changes in compartmental structure due to pathology.

3.2 Gross Anatomy and Microstructure of the Garfish Cranial Nerves

3.2.1 Olfactory Nerve

The olfactory nerve, which is the peripheral sensory nerve of smell, extends from the olfactory epithelium in the nostrils of the garfish snout to the olfactory bulb near the brain. The olfactory nerve lies together with the trigeminal nerve and a few small blood

vessels in a long bony channel which runs the length of the rostrum. The rostrum is the central longitudinal segment of the upper jaw which contains two bony channels, one on either side. Each bony channel contains its own nerve bundle consisting of olfactory nerve, trigeminal nerve, and blood vessels encased in a single connective tissue sheath. The size of the excised olfactory nerve was typically 0.5 to 1 mm in diameter and 3 to 4 cm long.

Fig. 3.2(a) shows a light microscopic cross-section of the olfactory nerve after excision and separation from the trigeminal nerve, blood vessels and sheath. Figs. 3.2(b) and (c) are EM micrographs of the nerve at much higher magnifications. The olfactory nerve consists of approximately 10^7 nonmyelinated nerve axons, each about 0.24 μm in diameter (8). In Fig. 3.2(c) mitochondria, microtubules, and neurofilaments can be seen inside the individual nerve axons. Groups of several hundred axons are enfolded by a single Schwann cell creating a Schwann cell domain, approximately 25 μm in diameter, which may be further subdivided by cytoplasmic processes of the same Schwann cell. Thus the axons are in direct contact with one another unlike most other nerves where each axon is individually wrapped by an enfolding Schwann cell. Where the axons are not in direct contact, they are separated by extracellular fluid. Some Schwann cell domains show large empty areas which may reflect axonal degeneration due to destruction of the cell body. The olfactory cell bodies are easily accessible to infection and destruction by toxic substances in polluted waters (8).

The Schwann cell domains of the olfactory nerve are separated from each other by connective tissue channels. These connective tissue channels are composed of an extracellular matrix, which is a gel-like substance consisting of tissue fluid derived from blood plasma with a high content of mucopolysaccharides and glycoproteins (14), with embedded fibrils of collagen and a few isolated connective tissue cells. The collagen fibrils aggregate around the Schwann cell domains leaving the wider channels much more sparsely populated with collagen, than the narrower channels.

3.2.2 Trigeminal Nerve

The trigeminal nerve which is found together with the olfactory nerve in the long bony channels of the garfish rostrum is just one branch, the maxillary branch, of the facial nerve. In fish, the facial nerve has four branches which constitute the general

cutaneous sensory nerves of the head. The excised trigeminal nerve was similar in length to the olfactory nerve (3 to 4 cm) and typically had a diameter of 0.25 to 0.5 mm.

The trigeminal nerve consists mainly of myelinated axons as can be seen in the light microscopic cross-section of the nerve, Fig. 3.3(a). The axons range in size from 2 μm to 30 μm in diameter with approximately 57% of the nerve cross-sectional area consisting of the largest axons with a few intermediate sized axons interspersed. The remaining 43% contains intermediate and small sized axons. Since these percentages were determined for a single nerve, there may be some biological variability between nerves of different fish. The nerve also contains a few unmyelinated axons which occupy ~1% of the total nerve cross sectional area and which can be distinguished in the EM of Fig. 3.3(b). These unmyelinated axons are the smallest axons with diameters on the order of 1 μm.

In peripheral nerves the axons are myelinated by Schwann cells. Since each Schwann cell creates only one internode of myelin, it is common in EM cross-sections to see some of the Schwann cell bodies. Examples of this are seen in Fig. 3.3(b). Separating the myelinated axons from one another is a connective tissue matrix similar to that found in the olfactory nerve. The collagen fibrils are concentrated around the myelinated fibres leaving the larger connective tissue spaces free of collagen. As well a few connective tissue cell bodies and their flattened cytoplasmic processes can be seen throughout this connective tissue space.

3.2.3 Optic Nerve

The optic nerve is the visual sensory nerve connecting the eye of the fish to the optic chiasm. The size of the optic nerve ranged from approximately 0.75 cm to 1 cm in length, and 1 mm to 1.5 mm in diameter. The overall structure of the nerve is shown in Fig. 3.4(a). There is an outer connective tissue sheath (on the order of 50 μm thick) which completely encloses the nerve plus a thinner inner sheath (~10 μm thick) which not only surrounds the nerve but penetrates the axonal space in such a way that in cross-section, the nerve appears to have a folded ribbon-like structure. The structure of the outer connective tissue sheath as well as the inner sheath is seen in Fig. 3.4(b). Both consist of layers of dense collagen fibrils separated by flattened connective tissue cell processes.

The connective tissue channels penetrating the nerve, Fig. 3.4(c), are similar in content to the connective tissue spaces in both the olfactory and trigeminal nerves. Dense collagen fibrils embedded in the connective tissue matrix border the axon field. A basement membrane separating this connective tissue space from the glial cell cytoplasm is easily seen in Fig. 3.4(c). Connective tissue cells and their flattened cytoplasmic processes are again dispersed throughout the connective tissue space.

The axonal field, shown in Fig. 3.4(d), consists of a fairly homogeneous population of myelinated axons. Axon sizes range from approximately 1 μm to 10 μm in diameter. The majority are in the 1 to 5 μm range with only a few in the 5 to 10 μm range. The optic nerve is part of the central nervous system and therefore the nerve axons are myelinated with oligodendrocytes. Since one oligodendrocyte creates numerous internodes of myelin it is quite uncommon to see the oligodendrocyte associated with a particular myelinated axon. Interspersed between the myelinated axons is glial cell cytoplasm. Some glial cell nuclei can be distinguished in Fig. 3.4(d).

3.3 Water Compartments in the Nerves

By considering the microcellular environment of the water protons in the various anatomical compartments as well as the various rates of exchange between compartments, we can postulate the number of observable transverse relaxation time components and their relative relaxation rates.

In the case of the olfactory nerve we postulate two NMR distinguishable water compartments, the Schwann cell domains, and the connective tissue space. We believe the Schwann cell domains constitute a single compartment for the following reasons. The EM of Fig. 3.2(c) shows a homogeneous population of nerve axons within each domain as well as a similar microstructure of the axoplasm. This suggests that the water molecules in all axons will have the same relaxation properties. Previous work on suspended and layered red blood cell ghosts in buffer (1), has demonstrated that in the case of single cells of ~5 μm diameter, transmembrane exchange is too fast to generate multiple components. Since the axons of the olfactory nerve are an order of magnitude smaller than the red blood cell ghosts, the exchange of water protons between the axoplasm and the extracellular space of each domain will definitely be fast enough to produce a single relaxation component whose mean relaxation rate will be the fast exchange average between the "bulk" water in the axoplasm as well as the extracellular

space, and the "hydration" layer of water associated with the cellular macromolecules. Because of the large number of closely spaced axons constituting each domain and the presence of the enfolding Schwann cell, we expect the exchange between each domain and its neighboring connective tissue space to be slow, resulting in two distinguishable relaxation compartments. The relaxation time of the water protons in the connective tissue channels will be longer due to the much smaller concentration of macromolecules in this space.

For the trigeminal nerve, the anatomical compartments giving rise to separate relaxation components are the axoplasm, the myelin, and the connective tissue space. Although the magnification of the EM in Fig. 3.3(b) is not high enough to discern the microstructural anatomy, the uniform transparency of all axons indicates a consistent relationship between the axonal water protons and their microcellular environments. Since it has been shown that the axonal membrane contributes very little to water proton relaxation when compared to the contribution from the macromolecular structures in the axons (15), the relaxation of the water in the trigeminal nerve axons will be independent of axon size and will be a fast exchange average between the bulk water in the cells and the hydration layer of the intracellular structures. The myelin encasing each axon provides a diffusion barrier which causes slow exchange of water between the axoplasm, the myelin water itself, and the connective tissue space. Estimates of the exchange times across the myelin sheath have shown rapid exchange on a T_1 time scale but slow to intermediate exchange on a T_2 time scale. These estimates, which were undertaken to explain the enhancement of longitudinal relaxation of water protons in white matter (16) were based on permeability measurements for artificial sphingomyelin-cholesterol membranes at 25 °C. It was found that a time of 64 ms was required for water in the 10^{th} myelin layer to mix with the axoplasm. In the case of the trigeminal nerves, the myelin sheath is on average ~50 layers thick, yielding a complete exchange time of ~300 ms with the axoplasm. However, water in the myelin can exchange outwards as well, with the connective tissue space, thereby decreasing the time of water exchange out of the myelin to 150 ms. This exchange time is ~3 times greater than the expected T_2 of myelin and we should therefore see three components, axoplasm, myelin, and connective tissue space. The myelin is expected to have the shortest relaxation time because of its high relative concentration of proteins and other macromolecules. Due to fast exchange across single membranes, the connective tissue compartment includes the Schwann cell cytoplasm external to the myelin, and the few unmyelinated axons. Most of this space has a much lower concentration of proteins and macromolecules than the axoplasm, and

therefore, its exchange averaged relaxation time is expected to be much longer than that of the axoplasm.

In the case of the optic nerve, four different compartments are postulated: i) axoplasm, ii) myelin, iii) glia, and iv) connective tissue. As in the case of the trigeminal nerve, the optic nerve myelin, which is on average ~30 layers thick, will prevent fast exchange between water in the axoplasm, myelin, and glial cytoplasm, thereby creating the first three relaxation compartments. There may be some exchange between the glial cell cytoplasm and the connective tissue space, but this will be limited by the basement membrane and the dense layers of collagen fibrils. As well, only a very small proportion of the glial cell cytoplasm is in close proximity to the connective tissue spaces and therefore the connective tissue space provides the fourth compartment. Once again, we expect the myelin water to have the shortest relaxation time and the connective tissue the longest relaxation time due to their respective macromolecular densities. The axoplasm and glial cytoplasm will have intermediate relaxation times. Since axoplasm and glial cytoplasm have approximately the same solid content, we do not expect their relaxation times to be significantly different.

In comparing the relaxation compartments between nerves we expect the following. The axonal water compartments in each of the three nerves (Schwann cell domains in the case of the olfactory nerve) should be characterized by approximately the same mean relaxation time since axonal relaxation is independent of axon size and since the microcellular environment is similar for all axons regardless of nerve type. The myelin compartments of the trigeminal and optic nerves should also have similar short relaxation times. Any difference may be the result of a difference in protein, and water content due to the fact that they are myelinated by different cell types, the trigeminal by Schwann cells and the optic by oligodendrocytes. Of course the olfactory nerve should lack such a short time component as it contains no myelinated axons. Finally, since all three nerves contain similar connective tissue spaces we expect similar slow relaxation rates for these compartments.

Each of these postulated nerve water compartments will produce a transverse relaxation time distribution component of finite width. The finite width will be a result of the heterogeneity in the microstructural environment within each compartment and intermediate exchange at compartment boundaries.

3.4 Experimental

3.4.1 Excision of Nerves

Twenty-six to thirty centimeter long spotted garfish (Lepisosteus oculatus) were obtained from the Tropical Fish Gallery, Edmonton. The fish were anesthetized by immersion in 4g/l ethyl 3-aminobenzoate methanesulfonic acid (MS-222), Aldrich, for 10 to 15 minutes and then decapitated. The lower jaw was removed and discarded. Several shallow, transverse cuts were then made every centimeter or so along the length of the rostrum using a circular saw bit attached to a dremmel tool. Care was taken not to cut too deeply to avoid damaging the nerves. The terminal 0.5 cm of the rostrum, containing the olfactory cell bodies, was cut off and discarded. The remaining sections of the rostrum, beginning with the most distal, were then snapped at their respective shallow cuts and pulled from the distal end leaving two nerve bundles, one from each bony channel, attached proximally. Once all the segments of the rostrum were removed in this fashion, the remaining hard bony covering of the head between the eyes was peeled away exposing the olfactory/trigeminal nerve bundles right back to the olfactory bulbs. The nerve bundles were then cut as far back as possible and placed in a petri dish containing garfish buffer solution (8). During the entire dissection process the nerves were kept moist with this buffer. Viewing with a dissection microscope, the olfactory and trigeminal nerves were separated from one another by removing the surrounding sheath and blood vessels. Each nerve type was then placed in a 5 mm diameter NMR tube and completely bathed with about 50 µl of gar buffer. Each olfactory nerve was typically 15 µl in volume and each trigeminal nerve 10 µl in volume.

During the preparation of the olfactory and trigeminal nerves, the optic nerves were dissected from the head of the garfish. The bony skull of the fish was peeled further back to expose the anterior part of the brain. The optic nerve was very easy to locate as it was the large nerve connecting the eyeball to the optic chiasm located at the frontal part of the brain. After removal of the fatty tissue surrounding both optic nerves, the nerves were cut out simultaneously and placed in gar buffer. Once again the nerves were kept moist with buffer during their dissection. Placed under the dissection microscope, the optic nerves were cleaned of adhering fatty tissues and in some cases the outer connective tissue sheath removed. Both nerves, each consisting of approximately 10 µl volume, were placed with ~50 µl of buffer in a 5 mm diameter NMR tube.

In some instances only one of a given nerve type was successfully dissected, in which case only one nerve of that type was available for study. The time from excision to the first water proton transverse relaxation measurements ranged from 30 to 60 minutes for the olfactory nerve, 40 to 120 minutes for the trigeminal nerve, and 50 to 120 minutes for the optic nerve.

The garfish buffer solution contained 125 mM NaCl, 3.5 mM KCl and 3.5 mM $CaCl_2$. These concentrations were based upon the composition of garfish blood (8). To check these concentrations, a measurement of the garfish blood plasma osmolality was made with a vapour pressure osmometer and found to be 296 mosm/kg. The buffer solution osmolality, 267 mosm/kg, was within 10% of this measured value and therefore the ionic concentrations given above were maintained. The pH of the buffer was ~6 and was not adjusted.

3.4.2 Action Potential Measurements on the Nerves

To test the viability of the nerves, action potential measurements were made using a biphasic stimulating and recording electrode system. The basics of this system are shown in Fig. 3.5. A voltage difference is applied across the stimulating electrodes which depolarizes the nerve. Depolarization is a term used to describe the influx of Na^+ ions from the extracellular space into the axoplasm causing the potential difference across the axonal membrane to rise from its negative equilibrium value to a large positive value. If the depolarization is great enough and the nerve axons viable, an action potential is initiated and transmitted the length of the nerve. The recording electrodes measure the voltage differences as the action potential passes between them. The result is a biphasic signal which is amplified and displayed on an oscilloscope. The action potential signals measured in this way are then stored and transferred to a personal computer for processing.

The stimulating and recording electrodes of the particular system used were separated by a minimum distance of 1.2 cm and a maximum distance of 1.7 cm. Therefore only action potential measurements could be made on the olfactory and trigeminal nerves. The optic nerve was too short. The olfactory and trigeminal nerves used for the action potential study were dissected from a long-nosed garfish and were therefore 6 to 7cm long. Long-nosed garfish nerves were used rather than the spotted garfish variety because the nerves of the spotted garfish were not quite long enough.

The olfactory nerve was stimulated with a 7.5 volt, 1ms pulse at a frequency of 1 pulse every 1.2 s, while the trigeminal nerve was successfully stimulated with a 50 μs, 2 volt pulse at the same frequency. Action potential measurements were made every hour for up to 11 hours and then again at 23 and 30 hours. Between measurements, the nerves were placed in garfish buffer at room temperature.

3.4.3 NMR Transverse Relaxation Measurements

The NMR tube containing a given nerve type was placed in a 1 cm diameter rf solenoidal excitation and receiver coil, such that the sample was centered both vertically and horizontally. The nerve cords were coiled at the bottom of the NMR tube so that the rf coil extended ~ 0.5 cm above and below the sample. With the coil and sample assembly centered in the 40 cm bore magnet of a 100 MHz Bruker CXP spectrometer, the water proton transverse relaxation times were measured. The proton line width obtained for the < 100μl samples was typically 30 Hz. The transverse relaxation decay was measured using a 4096 echo CPMG add/subtract sequence (18, 19), with an inter-echo spacing, τ, of 1.6 ms. The 180° pulses were 10 μs in duration. The CPMG pulses were phase cycled in order to eliminate baseline errors (20) generated by both receiver dc offsets and residual magnetization caused by phase errors in the 180° pulses. The choice of the echo time was made to minimize the effects of diffusion on T_2. Sixteen averages were taken with a repetition interval of 20 seconds. All data were acquired using the Bruker 12 bit digitizer alternately sampling between real and imaginary data points every 4 μs. All measurements were made at a room temperature of (22 ± 2) °C.

In order to use all excised nerves from each garfish, transverse relaxation measurements were made successively on each nerve type, one after the other. The order of nerves was varied from fish to fish. Since a single measurement required approximately 20 minutes including setup time, each nerve type typically had a transverse relaxation measurement done every hour or so up to a maximum of 8 hours. Single measurements of T_2 were made at much longer times up to 1 or 2 weeks. In these cases the nerves were refrigerated after the 8 hour point.

3.4.4 Electron and Optical Microscopy of Nerves

Freshly excised nerves were fixed with 2% gluteraldehyde and 0.5% paraformaldehyde in 0.06 M cacodylate buffer and postfixed in osmium tetroxide. The nerves were then dehydrated in a graded series of ethanol and embedded in Epok. For EM ultrathin sections, 60 to 90 nm in thickness, were stained first with uranyl acetate and then with lead citrate. Sections were observed in a Hitachi H 7000 Transmission Electron Microscope. For light microscopy, thick sections ~0.5 to 2 μm were stained in 1% methylene blue. Olfactory nerves were also fixed at one and eight hours after excision while trigeminal and optic nerves were fixed at two and eight hours after excision, as well. From the time of excision to fixation, the nerves were immersed in gar buffer at room temperature.

3.5 Data Analysis

3.5.1 Analysis of Transverse Relaxation Measurements

The CPMG transverse relaxation experiments performed on the nerve chords provided time dependent magnetization decay curves consisting of 4096 points from 1.6 ms to 6.6 s at 1.6 ms intervals. The signal to noise ratio, given by the ratio of the magnetization at t =1.6 ms to the standard deviation of the noise, was typically 3000. For analysis, the 4096 point decay data set was reduced to a 230 point decay data set by sampling every point from 1.6 ms to 40 ms, every 4^{th} point from 40 ms to 200 ms, every 8^{th} point from 200 ms to 500 ms, and finally every 24^{th} point from 500 ms to 6.5 s. This form of sampling was chosen to come as close as possible to a logarithmic sampling in order to sample equitably each of the component relaxation times. Fig. 3.6 shows the time dependent magnetization decay data set from a typical T_2 experiment. Note the multiexponential nature of this decay.

The inversion of the multiexponential decay data into a distribution of relaxation times is accomplished with the linear inverse technique, T2LIN, described in detail in Chapter 2. This method is a continuous relaxation time distribution approach involving the non-negative least squares (NNLS) algorithm of Lawson and Hanson (21), as modified by Whittall and MacKay (22). This method has the advantages of (i) requiring no a priori guess as to the number of components, (ii) producing a fit to the

data that is stable and not dependent on initial guesses of the component times and fractions, and (iii) producing a more realistic description of the relaxation times in the sample.

The results of the simulation tests done upon this algorithm in Chapter 2 give an indication of the ability of T2LIN to determine the experimental relaxation time distributions. The tests of resolution indicate that with our typical SNR of 3000, we can expect to resolve components with a minimum relative peak separation of ~0.6 which corresponds to a factor of ~2 between peak relaxation times. As well, the simulation test to determine the effects of data point density reductions indicate that with data sets consisting of 230 points, resolution and precision will vary by ~7% and ~20%, respectively, due to differences in noise representations. The extent to which the nerve components will be degraded, due to the experimental limits on the data time window and SNR, can also be determined from the simulation test results. Given that our experimental SNR is 3000 and our data time window extends from 1.6 ms to 6 s, the resolved nerve components, within the range of 5 ms to 3 s, will be approximately 1.5 times wider than the true component widths, with further degradation outside of this range.

For a given sample, the repeatability for successive NMR measurements of both the relaxation rates and populations was better than ±10% for peaks whose populations were between 5 and 10% of the initial signal intensity, less than ±5% for larger peaks and ±20% for smaller peaks. The confidence level, as defined in Chapter 2, of all solutions was maintained at 99% to prevent the fitting of any noise.

Our usual method of displaying the output T2LIN nerve spectra, as shown in Fig. 3.7(a), has led to some misunderstanding regarding component populations. T2LIN generates solution spectra amplitudes at discrete times defined by an input T_2 grid consisting of 200 logarithmically spaced points from 1 ms to 10 s. Therefore, component populations are given by the sum of the discrete spectral amplitudes composing each continuous distribution component. The usual display method, which connects the spectral amplitude data points by a single line, implies that the populations are given by the enclosed areas. This is incorrect if the areas are taken relative to a linear time scale, i.e. see Fig 3.7(b). Thus to avoid any ambiguity about component populations, single T_2 spectra will be presented as a bar graph as shown in Fig. 3.7(c). However, the multiple spectra making up the time course stackplots will be shown as line graphs for presentation purposes in order to avoid confusion from overlapping

spectra. In this case the true component populations are indicated in separate population versus time graphs.

3.5.2 Analysis of Electron and Optical Microscopy of Nerves.

Selected 8x10 photographs of the electron and optical microscopy of each nerve were scanned with a Hewlett Packard Scan Jet and saved in Tiff file format on a Macintosh IIci computer. Photographs of the total cross-section plus EM photographs at higher magnifications were scanned for each nerve. The scanned images of each photograph were then analyzed in Image, which is a Macintosh software package useful for image analysis. Using the selection and thresholding options of this application, the proportionate areas of nerve compartments were determined.

In the case of the olfactory nerve, thresholding was used on the image of the total cross-section to determine the proportionate areas of the Schwann cell domains (75%) and the connective tissue channels (25%). Numerous Schwann cell domains at higher magnifications were then analyzed with the selection and area measurement options to determine the relative areas of Schwann cell cytoplasm, axoplasm, and extra-axonal space. As well numerous connective tissue channels were analyzed in a similar manner to measure the relative areas occupied by connective tissue cells, regions of dense collagen, and regions of no collagen.

The total trigeminal nerve cross-section was divided into two regions, a large axon region (57%) and a small axon region (43%). A high magnification image of each region was then analyzed to determine the proportion of each anatomical structure in that region. To determine area proportions for the total nerve a weighted average of the anatomical areas in each of the two regions was obtained.

The computer image of the optic nerve's total cross-section allowed determination of the areas corresponding to the outer connective tissue sheath (21%), the inner connective tissue sheath and its penetrating channels (11%), and the axon field (68%). Two representative regions of the axon field were analyzed at higher magnifications: a region adjacent to connective tissue channels, and a region distant from connective tissue channels. It was found that the regions close to the connective tissue channels contained a greater amount of glial cell cytoplasm. This is apparent in Figs. 3.4(c) and (d), which show regions of the axon field adjacent and far from connective tissue channels, respectively. A weighted average of the areas measured in

each of these two regions was then calculated based on an estimate of the proportion of the total axon field directly adjacent to the connective tissue channels. Using the total nerve cross-section, this proportion was estimated to be 20%. A segment of a connective tissue channel was also analyzed at high magnification to estimate the relative areas of dense collagen, no collagen, and connective tissue cells in the connective tissue space.

To determine the contribution to total nerve signal from each anatomical region, the area fractions were converted to water content. Water content values for the different tissue types found in the nerves are tabulated in Table 3.1.

3.6 Results

The action potential results for the olfactory nerve at ~3 and ~11 hours are shown in Figs. 3.8(a) and (b), respectively, while the action potential results for the trigeminal nerves at ~3 and ~30 hours are shown in Figs. 3.8(c) and (d), respectively.

Results of the analysis of EM and optical microscopy are tabulated in Table 3.2(a), (b), and (c) for the olfactory, trigeminal, and optic nerves, respectively. These tables include the converted water fractions and group the various anatomical regions into their postulated compartments.

The results of the application of T2LIN to 10 freshly excised olfactory nerves, 12 fresh trigeminal nerves, and 6 fresh optic nerves are summarized in Table 3.3(a), (b), and (c), respectively. Although there is considerable biological variability between samples of a given nerve type, the averages indicate that the same well defined features are common to all T_2 distributions for a particular nerve type. Typical spectra for each nerve are shown in Figs. 3.11(a), (b), and (c). For ease of comparison a summary of NMR component populations and compartment water populations from the EM and optical analysis for all nerves is given in Table 3.4. Note that all NMR data presented for freshly excised optic nerves are on nerves that were desheathed. Figs 3.12 shows the T_2 distribution of a removed outer connective tissue sheath alone.

In Fig. 3.13(a), 3.14(a) and 3.15(a) we demonstrate by means of stacked plots, the way in which the T_2 distributions of the nerves vary over time. The behavior of the individual relaxation populations is shown in Fig. 3.13(b), Fig. 3.14(b), and Fig. 3.15(b) for the olfactory nerve, trigeminal nerve, and optic nerve, respectively. Fig. 3.16 illustrates the decrease in T_2 of the buffer solution for each nerve.

3.7 Discussion

3.7.1 Viability of Excised Nerves

3.7.1.1 Action Potential Study

The action potential studies were very successful in proving the viability of the freshly excised nerves. These nerves, however, were of the long-nosed garfish variety and not of the spotted garfish, which were used in the NMR experiments. Electron microscopy of the long-nosed and spotted garfish nerves has shown no structural differences between the nerves of the different fish types. The only significant difference then, is their length. We therefore assume that the nerves will behave in a similar manner when kept under the same conditions (i.e. same excision technique, buffer solution and temperature), and extrapolate the general results of the action potential study to apply to the nerves used for NMR. Figs. 3.8(a) and (c) are examples of the action potential signal measured at ~3 hours after excision for the olfactory and trigeminal nerves respectively. These figures show an initial peak, which is an artifact of the stimulation pulse, followed by the biphasic recording of the action potential. The delay in time of the action potential from the point of stimulation is dependent upon the conduction velocity of the nerve impulse. In the case of the olfactory nerve, the positive peak of the action potential was on average at 51 ± 7 ms. Given that the minimum distance between electrodes was 1.2 cm, a simple calculation yields a conduction velocity of ~0.24 m/s. This value is consistent with previous measurements of conduction velocity in olfactory nerves (12, 23). In the case of the trigeminal nerve, the positive peak of the action potential occurred on average at 0.6 ± 0.1 ms indicating a conduction velocity of ~20 m/s, which is within the range of expected conduction velocities for large myelinated axons (24). The agreement of the measured conduction velocities with expected values is a good indication that the action potential signals measured were real and not artifactual. Another convincing argument is the fact that when the nerves were coiled loosely between the stimulating and recording electrodes rather than pulled tightly, the action potential peaks shifted to times as long as twice the average because of the longer conduction paths.

The measurement of an action potential signal is an indication that viable axons are present in the nerve under investigation. The proportion of viable nerve axons is not readily determinable from the action potential signals since the peak voltages were very

dependent upon how the nerves were laid upon the stimulating and recording electrodes and were therefore quite variable. Action potentials were detected in the olfactory nerve for a period of approximately 11 hours after excision as shown in Fig. 3.8(b). At the 11 hour point, the measured action potential had an amplitude which was significantly smaller than all previous measurements, being only 20% of the average amplitude. For the trigeminal nerve, an action potential was detectable at a much longer time of 30 hours, see Fig. 3.8(d). The amplitude of this signal was ~24% of the average and again significantly smaller than all previous measurements on that nerve. The decreased signal amplitude at long times is an indication that nerve axons are degenerating and can no longer transmit action potentials.

To summarize the important results of this action potential study, at periods of 1 to 2 hours from excision, the time period within which the transverse relaxation time measurements on freshly excised nerves had been made, the olfactory and trigeminal nerves tested, transmitted action potentials and were therefore viable. Since action potentials of the optic nerve could not be measured, it can only be assumed that its viability was similar to that of the trigeminal nerve since both are myelinated. However, the much shorter length of the optic nerve may affect its viability. After excision, the trigeminal nerve was capable of transmitting an action potential for up to 30 hours which was approximately 3 times longer than that for the olfactory nerve, indicating that trigeminal nerve axons do not degenerate as fast as olfactory nerve axons. Since the major difference between the olfactory and trigeminal nerves is the fact that the trigeminal nerve is myelinated while the olfactory is not, the difference in viability is most likely due to the myelination difference.

3.7.1.2 Electron Microscopy

Figs. 3.9(a), (b) and (c) are representative electron microscopic photographs of the olfactory nerve at 1 hour post excision, and the trigeminal and optic nerves at 2 hours post excision, respectively. These fixation times were chosen because they are the maximum times at which the transverse relaxation time measurement were made on the freshly excised nerves.

The EM photographs of the olfactory nerve, like the one pictured in Fig. 3.9(a), show that the nerve axons are intact and the majority are of normal size, ~.2 μm in diameter. However, a small number, ~10%, have increased in size and have become

irregularly shaped. The axonal membrane of these enlarged axons appears to be intact and may still be functional. Within the cytoplasm, mitochondria are still present but fewer neurofilaments and microtubules are seen. This enlargement and breakdown of the cytoplasmic structure is probably the beginnings of degeneration. The presence of these abnormal axons should not have much effect upon the transverse relaxation time distribution since a fast exchange average is expected between many axons of the Schwann cell domains and the contribution to this T_2 distribution from the few abnormal cells should not be too great. EM sections of the olfactory nerve were made proximal, intermediate and distal to the cell bodies and all showed similar structure. Thus at 1 hour from excision the olfactory nerve has an intact and normal structure except for the few enlarged axons.

EM and thick sections were also made at different positions along the length of the trigeminal nerve. All sections, see Fig. 3.9(b) as an example, show the myelin and the majority of axons to be intact. Some axons appear to have broken away from the myelin, but this was seen in control EMs as well, see Fig. 3.3(b).

Although the optic nerve EM of Fig. 3.9(c) is centered on a contracted axon within its myelin wrapping, it clearly shows normal structure for a vast number of myelinated axons. EM and optical microscopy of other sections show this as well. Therefore, at 2 hours post excision, both the trigeminal and optic nerves appear to be pretty much in a normal physiological state.

Figs. 3.10(a), (b) and (c) are EM photographs of the olfactory, trigeminal and optic nerves, respectively, at ~8 hours post excision. For this set of EM sections, the controls, fixed immediately after excision, showed normal structure for the olfactory nerve but very abnormal structures for the trigeminal and optic nerves. The trigeminal and optic nerve controls had substantial degeneration of myelin and axoplasm. The optic nerve was especially bad showing a very sparse population of thinly myelinated axons. The fish from which these nerves were excised, was contaminated with parasites and was not healthy. This may have had a degenerative effect upon the myelinated axons. It was therefore impossible to determine degenerative changes which occurred during the 8 hours after excision. The EM photographs at 8 hours for the trigeminal and optic nerves only serve as an indication of the type of degeneration which may occur in-vivo during disease and in-vitro after excision. No conclusions upon the time course of degeneration in these nerves can be made.

The olfactory nerve EM, on the other hand, does indicate the type of degeneration which occurs after excision. The EM of Fig. 3.10 (a) shows that in this

particular section the Schwann cell domains still exist at 8 hours, but the enfolded axon field is very much degenerated. Very few intact axons remain with the majority of the domain occupied by clumps of cellular debris amidst large empty spaces. It appears that when the axons die they expand 10 to 20 times their original size, while the cytoplasmic structures break down forming the large empty spaces within the distended remains of axonal membranes. The axons which remain intact become compacted. Since, in this case, only a small portion of the nerve was fixed and sectioned it is not certain that the entire nerve was in this same physiological state, but assuming it was, it was definitely not viable at this point in time. This is somewhat inconsistent with the results of the action potential study which indicated viability in the olfactory nerve for up to 11 hours. The inconsistency may simply be explained by biological variability or by the fact that the nerves used in the action potential study were from a long-nosed garfish and were therefore much longer with increased viability.

3.7.2 Transverse Relaxation in Freshly Excised Nerves

The action potential and EM studies described above confirm the viability of the freshly excised nerves. Therefore, the in-vitro transverse relaxation time measurements upon the freshly excised nerves can be considered a good approximation to the situation in-vivo. The most important result of the transverse relaxation studies of the garfish nerves is the presence of a significant short time component, denoted by C, in the T_2 spectra of both myelinated nerve types, which is not seen in the nonmyelinated olfactory T_2 distribution. Since the major anatomical difference between these two nerve types (myelinated and nonmyelinated) is the presence of myelin, and since the T_2 of myelin is expected to be short because of its large solid content, we have attributed component C in both trigeminal and optic nerves to myelin water. In further support of this assignment, the NMR populations for component C agree with the myelin water populations derived from EM and optical microscopy (see Table 3.4). As well, the average relaxation times for the myelin components, 49 ms in the optic nerve and 34 ms in the trigeminal, are on the order of those presented previously for myelin water in the frog sciatic nerve (3), and white matter tissue (4,5,6).

The similarity , in terms of mean transverse relaxation times, between components denoted A and B in all three nerve types, upholds the assignment of these two components to similar anatomical compartments in each nerve type. First, consider

the simplest nerve type, the nonmyelinated olfactory nerve. The results of the transverse relaxation time measurements on freshly excised olfactory nerves consistently showed two main components, denoted A and B, plus a third small component, C, which was quite variable. The agreement of the NMR component populations and the compartmental populations determined from EM and optical microscopy (see Table 3.4) was very good. This agreement leads us to assign component A to the water of the connective tissue and component B to the fast exchanging water within the Schwann cell domains which are 75% intracellular space by volume. The average transverse relaxation times of 508 ms and 169 ms, corresponding to components A and B respectively, are consistent with the T_2 times determined for the extra-axonal ($T_2 = 639$ ms) and axonal ($T_2 = 197$ ms) spaces , respectively, in the crayfish nerve cord (2). These relaxation times are somewhat larger than but similar in proportion to those transverse relaxation times found for axoplasmic ($T_2 = 70$ ms) and extracellular ($T_2 = 310$ ms) water in the frog sciatic nerve. As well, the relaxation time of component B is close to that found for the intracellular water component ($T_2 = 80$ to100 ms) in cat (4), guinea pig (5), and human (6) white matter.

Because the connective tissue spaces in all three nerves are quite similar and the T_2 of nerve axoplasm is not expected to differ too much between these three nerve types, components A and B in the trigeminal and optic nerves are also assigned to connective tissue water and axoplasm, respectively. Recall that component B in the olfactory nerve is a result of the fast exchange between water of the entire Schwann cell domain which includes ~25% extracellular water. This may explain the slightly longer T_2 of component B in the olfactory nerve (169 ms) when compared to component B of the myelinated nerves (~140 ms).

Referring to Table 3.4, the NMR populations for components A and B of the trigeminal nerve agree with the EM and optical populations within experimental error and biological variability. This supports the assignment of the connective tissue space to component A and the axons to component B. In the case of the optic nerve, the microscopy and NMR populations for components A and B do not agree within experimental error and biological variability. The optic nerve is somewhat different from the trigeminal nerve in that glial cell cytoplasm is interspersed between the mylinated axons rather than connective tissue. Because the transverse relaxation time of the glial cell compartment is not expected to be significantly different from that of the axoplasm, glia are grouped together with axoplasm in the assignment of the anatomical compartments to the NMR components. This assignment yields the best agreement

between NMR and EM populations. However, an inconsistency remains which may be due to the complexity of the dense inner connective tissue sheath, which remains adhered to the nerve even after the outer connective sheath has been removed.

The components denoted by D in the optic and trigeminal nerve T_2 spectra and the component denoted E in the optic T_2 spectra have not been assigned to any anatomical compartment since small water compartments such as these could not be determined in the EM sections. They may be due to water molecules associated with collagen as will be discussed in the next section.

3.7.3 Transverse Relaxation of Outer Connective Sheath of the Optic Nerve

The T_2 spectra of the optic nerve's outer connective tissue sheath, shown in Fig. 3.12 is more complex than initially anticipated, consisting of 4 distinct components. The origin of these components is not completely understood and can only be speculated. The outer sheath, shown in the EM of Fig. 3.4(b), consists of dense layers of collagen fibrils, separated by flattened connective tissue cell processes. The connective tissue ground substance fills the spaces between the individual collagen fibres and between the dense layers. A previous study of proton relaxation in collagen (25), had identified three water proton populations each with its own characteristic transverse relaxation time. The first population had a T_2 of ~10 ms and was identified with the water molecules tightly bound within the triple helix structure of the collagen. The second population, T_2 ~ 25 ms, was identified with the weakly bound hydration water associated with the collagen, while the third water population, T_2 ~100 ms, was associated with the amorphous ground substance between the collagen fibres. The bound and hydration water fractions of collagen may be responsible for the two shortest components seen in the optic nerve sheath's T_2 spectrum. They may also be responsible for component D of the optic and trigeminal nerves as well as component C of the olfactory nerve. The T_2 of the optic nerve sheath also shows two large components with $T_2 > 100$ ms. The cellular component of the connective tissue may contribute to one of these, however, referring to the EM of Fig. 3.4(b), the cellular contribution does not appear to be that great. It may be possible that the ground substance within the dense collagen layers contributes to the component at ~120 ms, while the ground substance between layers contributes to the longest T_2 component. In support of this, it was found that when the outer connective tissue sheath was placed in an NMR tube with the same

amount of buffer as was placed with the desheathed nerve in a separate tube, the nerve sheath signal was ~70% of the entire desheathed nerves signal. This is ~3 times greater than what area and water population values predict. The dissection and desheathing process probably causes separation of the collagen layers of the outer sheath which will cause an increase in the populations of the ground substance water fractions. The populations of the bound and hydration water fractions should not be affected because the amount of collagen remains fixed. This increase in ground substance water fraction may explain the inconsistency between the NMR populations and the EM populations for the optic nerve, since the desheathed nerves are still surrounded by a thin sheath similar to the outer sheath, which may also be damaged during the desheathing process.

The optic nerve, therefore, is not the ideal white matter tissue model due to the complexity of the dense connective tissues which remain even after desheathing. The presence of nerve sheath T_2 components between 50 ms and 120 ms complicates the most important optic nerve components B and C assigned to intracellular and myelin water, respectively. In the case of the olfactory and trigeminal nerves, no dense connective tissue sheath is present and the collagen within the inner connective tissue spaces is only sparsely populated in comparison with the dense collagen of the optic nerve. Therefore no complicating effects due to dense connective tissues are present in the olfactory and trigeminal T_2 spectra.

3.7.4 Time Dependent Measurements

Upon excision of the nerves, the axons are cut off from their parent cell body and as time progresses, nerve cell death progresses. Cell death is characterized by shifts in electrolyte and fluid balances and eventually Wallerian degeneration. These changes should cause variations in peak populations and relaxation times which are consistent with our assignment hypothesis. Furthermore, by following the changes that accompany nerve death, we can evaluate the promise of NMRI techniques to provide quantitative information about healthy and diseased neurological tissue and ways to differentiate the two.

Figs. 3.13(a), 3.14(a), and 3.15(a) demonstrate by means of stacked plots, the behavior of the T_2 distributions of the nerves in bathing medium over a period of 3 days for the olfactory nerve, 13 days for the trigeminal nerve and 7 days for the optic nerve. Note that the component corresponding to the bathing solution has been cutoff in order

to emphasize the variations in the nerve components. Since component population variations are difficult to discern from the stacked plots, the component populations, including that for the bathing solution are quantified in Figs. 3.13(b), 3.14(b) and 3.15(b) for each nerve respectively.

The most significant result of the time dependent measurements is the fact that major variations in the olfactory nerve's T_2 spectra can occur within hours but similar variations are not seen in the trigeminal or optic nerves, even at much longer times. The most probable cause of this result is the difference in the anatomical structure of these three nerves, predominantly the presence of myelin in the latter two. In the case of the olfactory nerve, Fig. 3.13(a), the increase in the population of component A relative to component B and the convergence of these two components by 8 hrs 20 min may reflect the progressive degeneration of the olfactory nerve axons. From the time of excision, the axons begin to degenerate. It is not known exactly how the excised nerves degenerated or how fast. Degeneration has been measured in olfactory nerves detached from their cell bodies but remaining within the animal (10). In this case, degeneration was found to progress from the proximal end near the cell body towards the distal end at temperature dependent rates, 0.3 mm/day at 10 °C to 6.0 mm/day at 22 °C. However, in our case, the nerves are completely excised and bathed in Ringer's solution. Therefore, degeneration may progress from the proximal end, from both ends, or along the entire length simultaneously, and may occur at a much faster rate. Regardless of how the excised nerves degenerate, it is certain that as the time from excision increases, the proportion of the nerve which is degenerated also increases. The EM of Fig. 3.10(a) is an example of axonal degeneration in the olfactory nerve. This particular section, which was fixed 8hrs after excision, shows complete degeneration of the axons which are replaced by large empty spaces and cellular debris. The encasing Schwann cells remain intact. In such a degenerated state, the exchange of water between the domains and the connective tissue channels would no longer be restricted by the intact axonal membranes and cytoplasm resulting in a fast exchange between these two compartments. As the proportion of degenerated nerve increases, the proportion of the domainal water in fast exchange with the connective tissue channels should increase as well, and therefore, the T_2 component corresponding to the connective tissue space should show an increase in amplitude while the domain component shows a decrease. Finally, when the degree of degeneration becomes great enough the T_2 distribution should yield a single dominant component with a T_2 value less than that of the original connective tissue space brought about by the new exchange with the cellular debris.

This scenario is almost identical to the actual variation in the olfactory T_2 spectra over time. The population and T_2 variations for the nerve components are somewhat complicated by the fact that the bathing solution is continuously seeping into the nerve as is illustrated in Fig. 3.13(b). If the convergence of components A and B in the olfactory is a true reflection of degeneration then the rate of degeneration varies from nerve to nerve since convergence was seen to occur at times ranging from 5 hours to 5 days. This variation may be a result of differences in nerve length or different degrees of nerve damage during excision.

The trigeminal nerve shows no convergence of T_2 components A and B even at two weeks, Fig. 3.14(a). This can be explained by the fact that myelin requires a substantially longer time to break down and therefore the compartments generating components A and B, namely connective tissue and axoplasm, remain separate. Over time periods on the order of 1 to 2 weeks, it is expected that the myelinated axons will begin to degenerate. Fig. 3.10(b) illustrates various stages of degeneration of myelinated trigeminal nerves. The axolemma breaks away from the inner myelin layer and contracts inward as the myelin layers separate and expand inwards to fill the axonal space. The actual variations in the trigeminal T_2 spectra over time are consistent with these anatomical changes. By day 13, the myelin component, C, shows a decrease in population while the axonal component, B, shows an increase in population with a decrease in T_2. This latter variation is consistent if the degenerated axons filled with separated myelin layers have a characteristic T_2 only marginally less than that of the intact axoplasm. Component A, corresponding to the connective tissue space shows an increase in population and decrease in T_2 as well. This may be a result of the influx of buffer in combination with an increased amount of cellular debris in the extracellular space.

The optic nerve, like the trigeminal , also shows no convergence of the two dominant components, A and B, over a period of 7 days, Fig. 3.15(a). Because the anatomy of the optic nerve is different from that of the trigeminal nerve in that the myelinated axons are separated by glial cell cytoplasm, a breakdown of the myelin would not directly affect the exchange of water between the connective tissue channels and the axon field. In this case the separation of components A and B, which have been assigned to the connective tissue and intracellular spaces, respectively, may persist because the layers of dense collagen separating these two regions do not break down and the diffusion of water across the axon field is slowed by the cellular debris, especially the degenerating myelin .

A significant result seen in the variation of the optic T_2 spectra over time is the fact that the component we have assigned to myelin water, C, is only partially resolved from component B at 1 hour and 20 minutes and thereafter is not resolved at all. The lack of resolution between components B and C may be caused by an increase in myelin permeability brought about by cell death, resulting in a fast exchange between myelin water, axoplasm, and glial cell cytoplasm. The reason why resolution of myelin and axonal components is not a problem in the trigeminal nerve is the fact that trigeminal nerve axons are approximately an order of magnitude larger than optic nerve axons. Therefore, the trigeminal nerves axons have substantially more myelin wrappings and the diffusional barrier between intra-myelinic and extra-myelinic water is much greater than in the optic nerve. Also, trigeminal nerves are ~3 times longer than the optic nerves and if degeneration progresses from the end nearest to the cell bodies then a larger proportion of the optic nerve will degenerate in a given amount of time when compared to the proportion of the trigeminal nerve degenerated. Thus in the case of the optic nerve, individual variations over time in the populations and transverse relaxation times of myelinic, axoplasmic, and glial cell water cannot be distinguished. Only variations in the cumulative population of these three compartments and the exchange averaged relaxation time can be determined. The plot of optic nerve component population versus time in Fig. 3.15(b) shows an increase in the extracellular population, component A, by a factor of two, while the total intracellular population, components B and C combined, decreases by approximately one third over a period of 7 days. The biphasic variation in these two populations, i.e. the large changes within the first 6 hours from excision followed by a much slower variation afterwards may be a result of the temperature dependence of degeneration since the nerves were refrigerated from the 6 hour point to 7 days. The increase in population of the extracellular component, A, is caused partially by an inflow of water from the bathing solution plus a shift of water from the intracellular to extracellular space. This occurs because the extracellular space is hypertonic relative to plasma or plasma analogues such as the garfish Ringer solution (26, 27) and becomes even more hypertonic upon cell death when cellular debris begins to accumulate. Thus the extracellular space also exhibits a shortening of its relaxation time. The intracellular components, B and C unresolved, also shows a decrease in relaxation time brought about by its decrease in water content. These variations in the water proton populations of the intracellular and extracellular spaces are consistent with those reported in the crayfish nerve cord (2).

Another consequence of degeneration which was also seen in the crayfish nerve cord studies (2) and is illustrated in Fig. 3.16 is the decrease in the relaxation time of the bathing solution by a factor of ~1.5. This is brought about by an accumulation of cellular debris in the bathing solution. It was also found that the variation in the bathing solution population varied from nerve to nerve. For example, in the case of the olfactory nerve, one nerve showed only a 5% decrease in bathing solution population over a 5 day period while in the example given, Fig. 3.13(b), a decrease in the bathing solution population by 20% occurred over 3 days. In fact, it was found that the olfactory nerves which showed little decrease in bathing solution population, took much longer for components A and B to converge into one. This is further proof that the convergence of peaks A and B in the olfactory nerve is indicative of cell death since a shift of water from the bathing solution into the nerve is expected upon cell death. When cells die, their ion pumps shut down, intracellular ions accumulate, setting up osmotic gradients which result in an influx of water.

Variations in the small unidentified components are not significant. The fact that population changes are small supports their assignment to collagen bound and hydration water since the amount of collagen is not expected to vary much over time. As well the shifts in T_2 of these components is consistent with the fact that the T_2 of bound water of collagen is orientation dependent (25).

3.8 Conclusion

In this chapter we have investigated the multiexponential transverse magnetization decay of water protons in nonmyelinated and myelinated nerves of the spotted garfish. The assignment of the multiple transverse relaxation time components in the various nerves to different anatomical compartments was achieved through comparisons of the NMR component populations with populations derived from EM and optical microscopy. Assignments were supported by comparisons of component relaxation times to previously reported relaxation times in similar nerve tissues as well as comparisons between the three garfish nerves themselves. The anatomical compartments successfully identified with NMR transverse relaxation components are the following: the extracellular space in the form of connective tissue channels in each of the three nerves, the Schwann cell domains of the olfactory nerve which are a fast exchange average of water in the axons, extracellular space and enclosing Schwann cells,

the axonal water of the trigeminal nerve, and the unresolved axonal and glial cell water of the optic nerve. The final and most important assignment is that of myelin water in both the trigeminal and optic nerves. The transverse relaxation time spectra discovered for the dense connective tissue sheath of the optic nerve was found to be quite complex consisting of multiple components spanning the same range of relaxation times as the optic nerve T_2 spectra. Since a similar but thinner connective tissue remains on the optic nerve even after desheathment, the optic nerve T_2 spectra is no doubt complicated by multiple components originating from this sheath. Thus the optic nerve is not an ideal model for white matter tissue of the brain.

The fact that the action potential measurements and EM sections exhibit viable nerves is a good indication that similar transverse relaxation time distributions exist in-vivo. If these distributions could be measured in-vivo, then nerve tissues could be characterized by their T_2 distribution. The time course measurements indicate that transverse relaxation is sensitive to the physiological state of tissue, and may therefore be useful in differentiating normal and diseased tissue. For example in Multiple Sclerosis, myelin breaks down and is digested by surrounding glial cells while the axon remains intact. Although this disease is significantly different from the form of degeneration which occurs in-vitro in excised myelinated nerves, where degenerating myelin is not removed and axons and glia degenerate as well, MS lesions should still be distinguishable from normal white matter lesions. The lack of myelin should result in the disappearance of the short time component in the T_2 distribution just as the degeneration of myelin in the in-vitro nerves causes a decrease in the short T_2 component assigned to myelin. Thus multi-component transverse relaxation has the potential to be a very important diagnostic tool.

Table 3.1

Volume fractions of water in various types of nervous tissue found in the garfish cranial nerves.

Tissue type	Volume fraction of water[a]
axons	0.75
glia[b]	0.85
myelin	0.40
connective tissue	0.90
dense connective tissue	0.70
extracellular space[c]	1.00

[a] Estimated from references (2,28-31).

[b] Includes Schwann cells in the peripheral nerves plus oligodendrocytes, astrocytes, and other glial cell types in the optic nerve.

[c] Extra-axonal spaces within the Schwann cell domains of the olfactory nerve.

Table 3.2(a)

Water populations of various anatomical compartments of the olfactory nerve.

Compartment	Cross-sectional area[a,c] (% of total area)	Water population[b,c] (% of total nerve water)
A. CONNECTIVE TISSUE	25±2	27±3
B. SCHWANN CELL DOMAINS		
axons	48±4	43±4
extracellular space	16±1	19±2
Schwann cell bodies	11±1	11±1

[a] Measured from digitized electron and optical microscopy cross-sections.
[b] Calculated using volume fractions of water from Table 3.1.
[c] Variabilities given are calculated from estimated errors in area measurements and do not include biological variability.

Table 3.2(b)

Water populations of various anatomical compartments of the trigeminal nerve.

Compartment	Cross-sectional area[a,c] (% of total area)	Water population[b,c] (% of total nerve water)
A. CONNECTIVE TISSUE SPACE		
connective tissue	22±2	29±4
glia[d]	3±1	4±1
unmyelinated axons	1±0	1±0
B. AXONS	41±4	46±5
C. MYELIN	33±3	20±3

[a] Measured from digitized electron and optical microscopy cross-sections.
[b] Calculated using volume fractions of water from Table 3.1.
[c] Variabilities given are calculated from estimated errors in area measurements and do not include biological variability.
[d] Includes Schwann cell cytoplasm associated with and external to the myelin as well as the Schwann cell associated with the unmyelinated axons.

Table 3.2(c)

Water populations of various anatomical compartments of the optic nerve.

Compartment	Cross-sectional area[a,c] (% of total area)	Water population[b,c] (% of total nerve water)
A. CONNECTIVE TISSUE		
connective tissue channels	7±1	9±2
dense connective sheath	8±1	8±2
B. INTRACELLULAR		
axons	34±3	37±4
glia[d]	24±2	30±4
C. MYELIN	27±2	16±2

[a] Measured from digitized electron and optical microscopy cross-sections.
[b] Calculated using volume fractions of water from Table 3.1.
[c] Variabilities given are calculated from estimated errors in area measurements and do not include biological variability.
[d] Oligodendrocytes, astrocytes, and other neuroglial cells.

Table 3.3(a)

Summary of populations and relaxation times in 10 freshly excised olfactory nerves

Component	A		B		C	
	Population[a,c]	T_2[c] (ms)	Population[a,b]	T_2[b] (ms)	Population[a,d]	T_2[d] (ms)
	15.6	596	83.4	165	1.0	12
	17.5	495	80.6	179	1.9	22
	20.9	486	77.7	201	1.4	6
	28.7	453	65.5	163	5.7	39
	13.4	700	84.7	183	1.9	14
	15.2	580	81.6	170	3.2	19
	26.5	451	72.6	163	0.9	8
	28.7	428	67.5	148	3.7	9
	19.8	515	78.5	173	1.2	15
	19.7	380	74.9	131	5.4	27
Mean[e]	21 ±6	510 ±90	77 ±7	170 ±20	3 ±2	17 ±10

[a] Normalized to 100.
[b] ±5%
[c] ±10%
[d] ±20%
[e] Variability given as the standard deviation of the 10 measurements.

Table 3.3(b)

Summary of populations and relaxation times in 12 freshly excised trigeminal nerves

Component	A		B		C		D	
	Population[a,b]	T_2[b] (ms)	Population[a,b]	T_2[b] (ms)	Population[a,c]	T_2[c] (ms)	Population[a,c]	T_2[c] (ms)
	46.2	447	38.7	125	11.2	32	3.8	9
	46.9	438	37.6	130	12.1	29	3.4	9
	38.9	459	37.6	127	17.1	36	6.4	8
	39.5	502	39.1	131	16.4	37	4.9	9
	40.3	452	40.1	148	15.4	37	4.2	7
	32.9	563	37.7	157	7.6	41	21.8	12
	43.8	469	39.7	146	11.4	35	5.1	14
	42.4	423	41.3	126	14.4	27	1.9	4
	34.9	486	46.3	183	16.6	38	2.3	5
	38.7	464	46.3	145	13.9	27	1.1	3
	53.9	370	30.8	106	12.0	25	3.3	7
	40.9	472	38.5	146	16.1	39	4.5	8
Mean[d]	42 ±6	460 ±50	40 ±4	140 ±20	14 ±3	34 ±5	5 ±5	8 ±3

[a] Normalized to 100.
[b] ±10%
[c] ±20%
[d] Variability given as the standard deviation of the 12 measurements.

Table 3.3(c)

Summary of populations and relaxation times in 6 freshly excised optic nerves

Component	A		B		C		D		E	
	Pop[a,b]	T_2[b] (ms)	Pop[a,b]	T_2[b] (ms)	Pop[a,c]	T_2[c] (ms)	Pop[a,c]	T_2[c] (ms)	Pop[a,c]	T_2[c] (ms)
	26.4	435	48.5	141	17.2	62	7.1	13	0.8	3
	20.4	560	49.7	123	25.2	45	4.6	9	-	-
	27.2	494	57.5	147	9.7	44	4.7	9	0.9	2
	26.7	483	52.5	143	13.5	49	7.0	10	0.3	2
	24.5	441	57.8	115	10.6	39	7.1	8	-	-
	25.6	490	51.5	159	16.5	55	4.9	15	1.4	3
Mean[d]	25 ±2	480 ±40	53 ±4	140 ±20	16 ±5	49 ±8	6 ±1	11 ±3	1 ±1	2 ±1

[a] Normalized to 100.
[b] ±10%
[c] ±20%
[d] Variability given as the standard deviation of the 6 measurements.
[e] Dashes indicate component was not present.

Table 3.4

Comparison of NMR populations with those derived from electron and optical microscopy cross-sections.

Compartment	Population	
	EM and optical microscopy	NMR
OLFACTORY		
A. Connective tissue	27±3	21±6
B. Schwann cell domains (axons, Schwann cells, extracellular space)	73±7	77±7
TRIGEMINAL		
A. Connective tissue space (connective tissue, Schwann cells, unmyelinated axons)	34±5	42±6
B. Axons	46±5	40±4
C. Myelin	20±3	14±3
OPTIC		
A. Connective tissue	17±4	25±2
B. Intracellular (Axons and glia)	67±8	53±4
C. Myelin	16±2	16±5

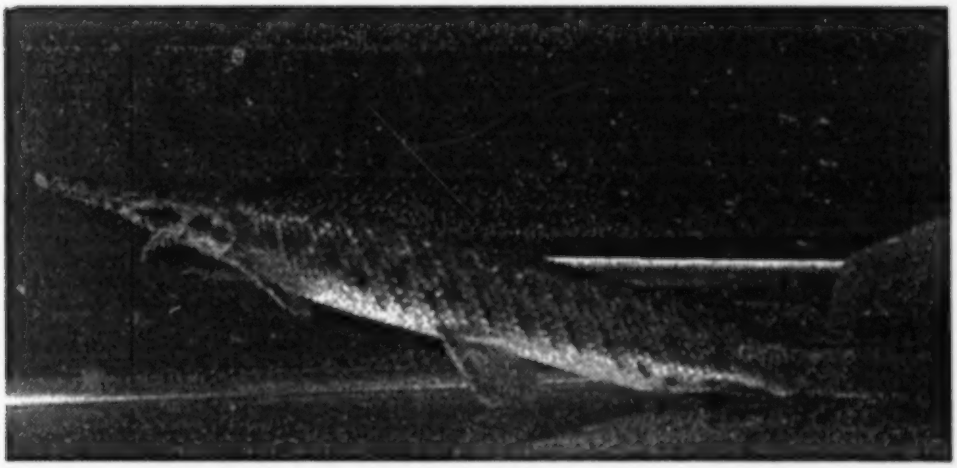

5 cm

Figure 3.1 Spotted garfish (Lepisosteus Oculatus).

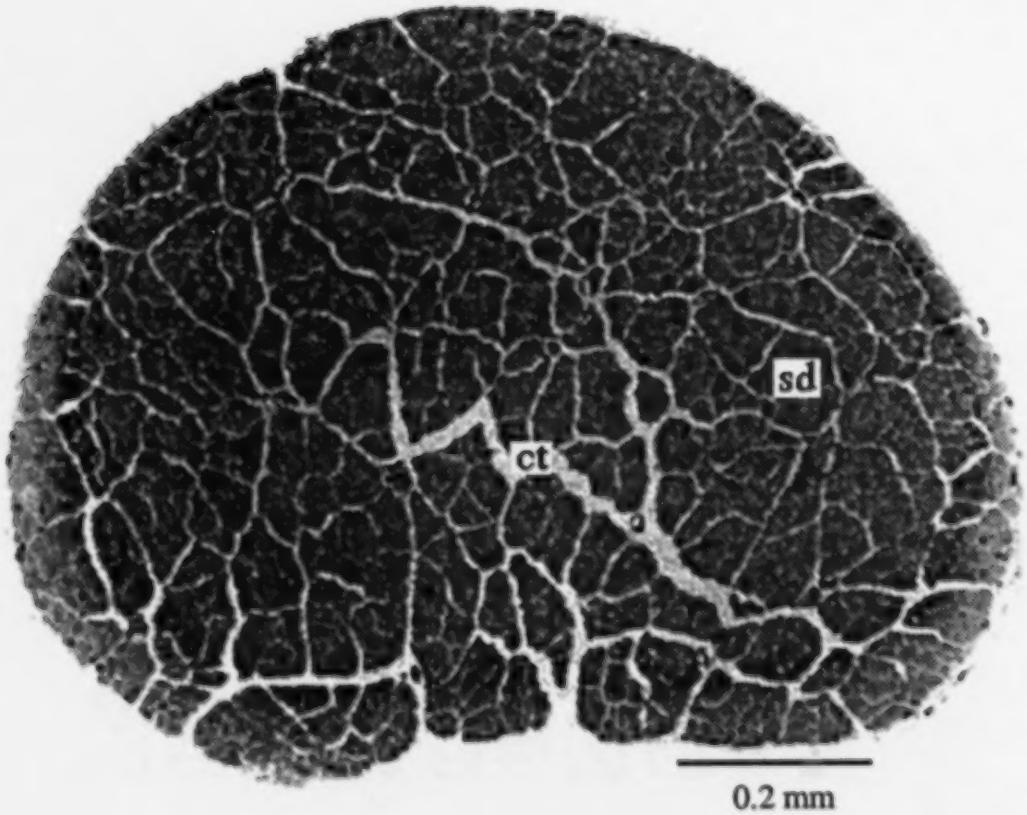

Figure 3.2(a) Light microscopic section of olfactory nerve after excision and separation from the trigeminal nerve. The nerve consists of numerous Schwann cell domains (sd) separated by connective tissue channels (ct). Each Schwann cell domain contains hundreds of axons enfolded by a single Schwann cell process.

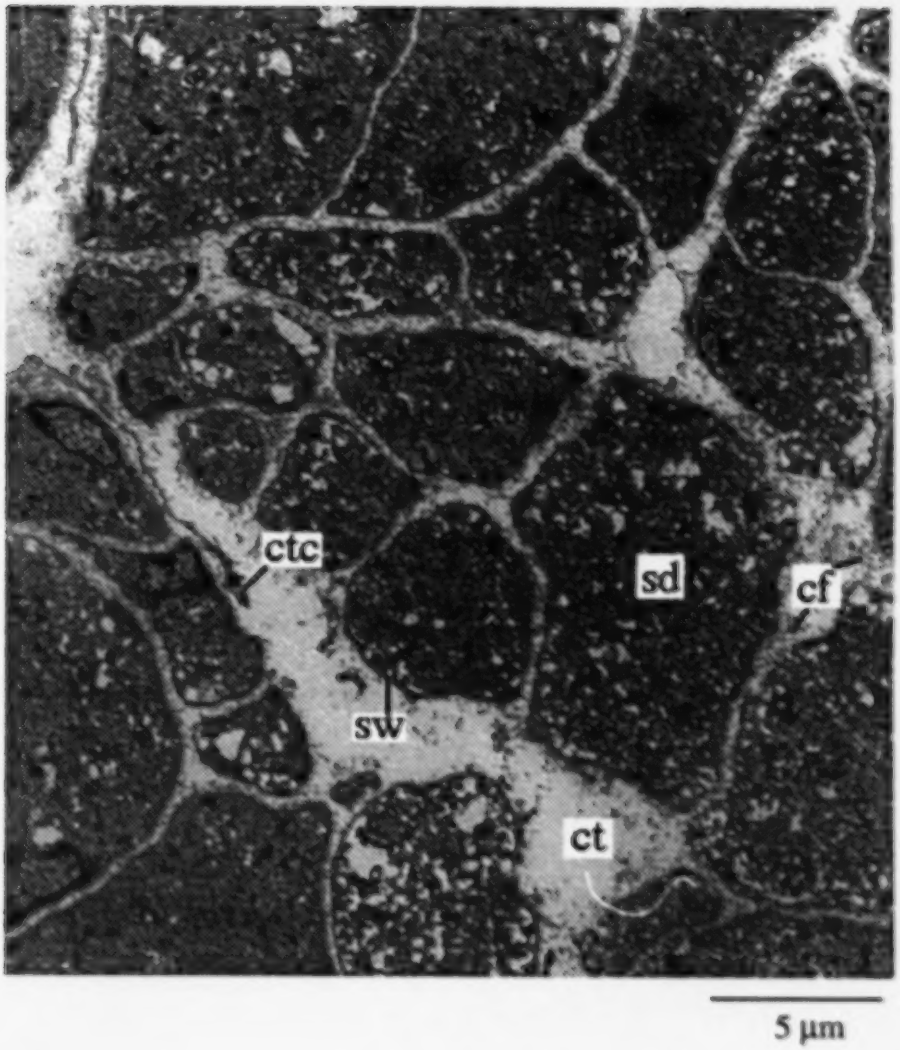

Figure 3.2(b) Olfactory nerve. In this EM, the individual Schwann cell domains (sd) are seen at a high enough magnification to distinguish the Schwann cell wrappings (sw). Collagen fibrils (cf) and connective tissue cells (ctc) can also be seen in the connective tissue channels (ct). Collagen is concentrated at the Schwann domain boundaries and therefore the narrow channels have much denser collagen compared to the larger channels. There are some spaces within the domains which are devoid of axons. These may be regions from which axons have degenerated.

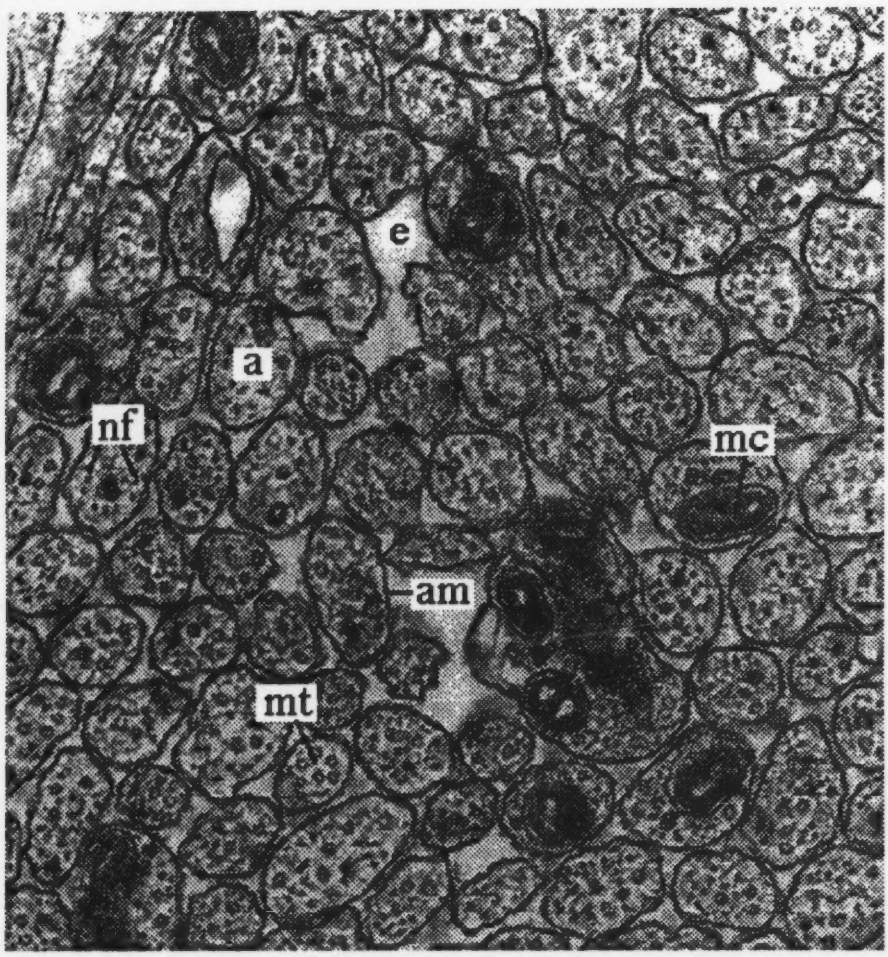

Figure 3.2(c) Olfactory nerve. This high magnification EM shows the individual axons (a) bounded by their axonal membrane (am). Within the axoplasm, microtubules (mt), neurofilaments (nf), and mitochodria (mc) can be distinguised. The axons are very homogeneous in size, ~2 μm diameter, and are packed together tightly within an extracellular medium (e).

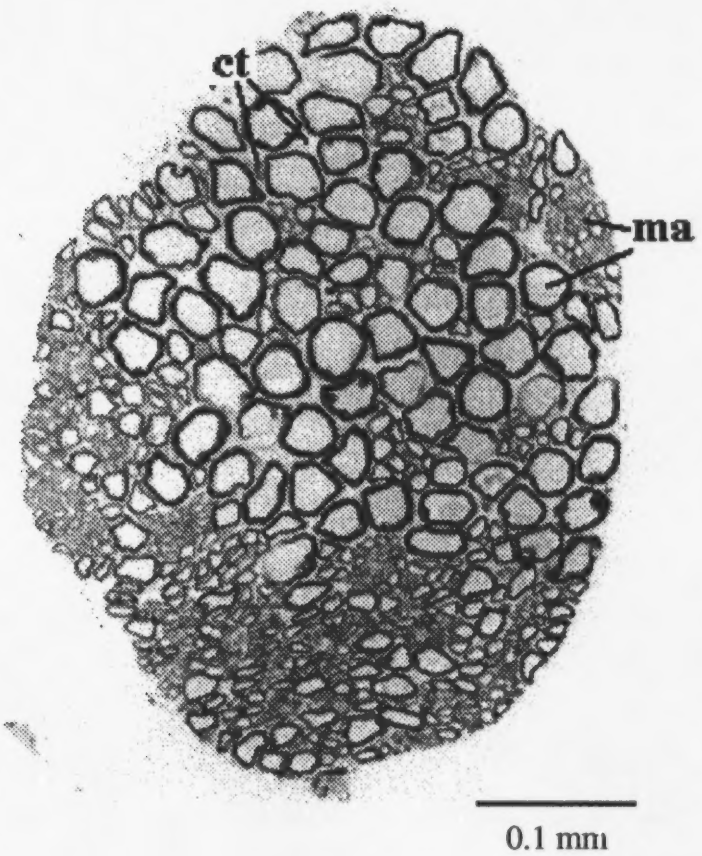

Figure 3.3(a) Light microscopic section of the trigeminal nerve. The trigeminal nerve consists mainly of myelinated axons (ma) which range in diameter from 2 μm to 30 μm. There are regions of large, intermediate, and small axons. Interspersed between the myelinated axons is connective tissue (ct).

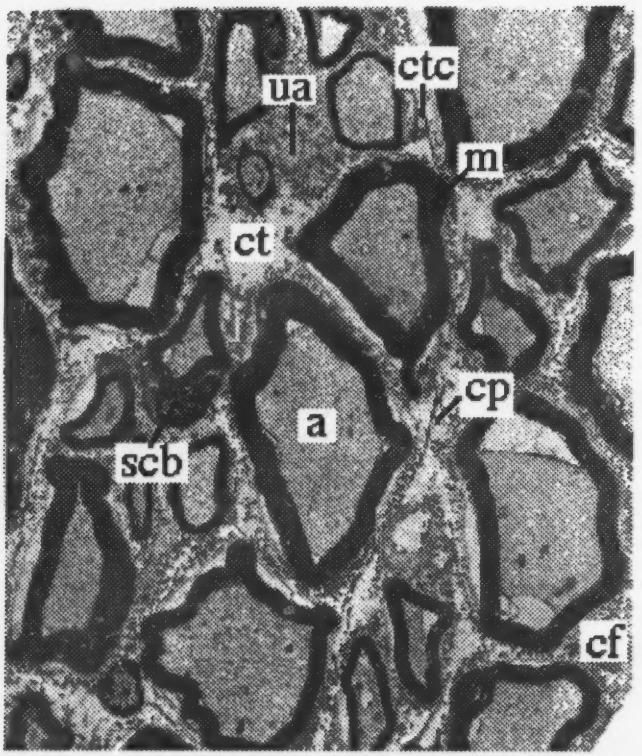

Figure 3.3(b) EM of trigeminal nerve fixed immediately after excision. Thick layers of myelin (m) wrap almost all axons (a). A few small unmyelinated axons (ua) are present as well. The myelinated axons are separated by connective tissue (ct) which contains collagen fibrils (cf), connective tissue cells (ctc), and their cellular processes (cp). The collagen fibrils tend to be concentrated around the myelinated fibres. Some Schwann cell bodies (scb) are seen associated with their myelin wrapping. At this magnification it is difficult to distinguish cytoplasmic constituents, however, some mitochondria are seen. Some axons have contracted away from their myelin leaving clear fluid filled spaces.

Figure 3.4(a) Light microscopic section of optic nerve. The nerve is enclosed by an outer connective tissue sheath (os) plus an inner sheath (is) which not only surrounds the nerve but penetrates the nerve forming connective tissue channels (ct). These channels give the nerve a folded ribbon-like structure. The inner portion of the nerve consists of myelinated axons separated by glial cell cytoplasm.

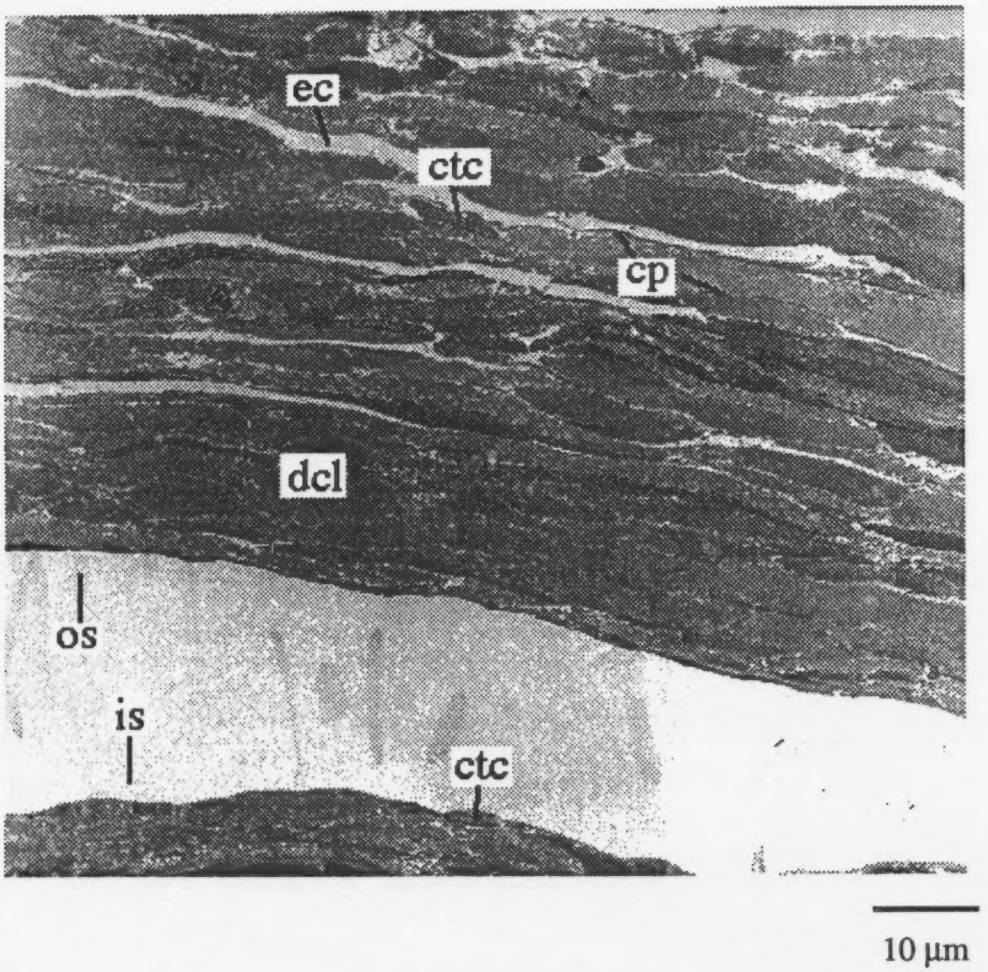

Figure 3.4(b) Outer and inner connective tissue sheath of the optic nerve. Both the inner (is) and outer sheath (os) consist of dense collagen layers (dcl) separated by connective tissue cells (ctc) and their processes (cp). Some extracellular clefts (ec) are present between layers of the outer sheath.

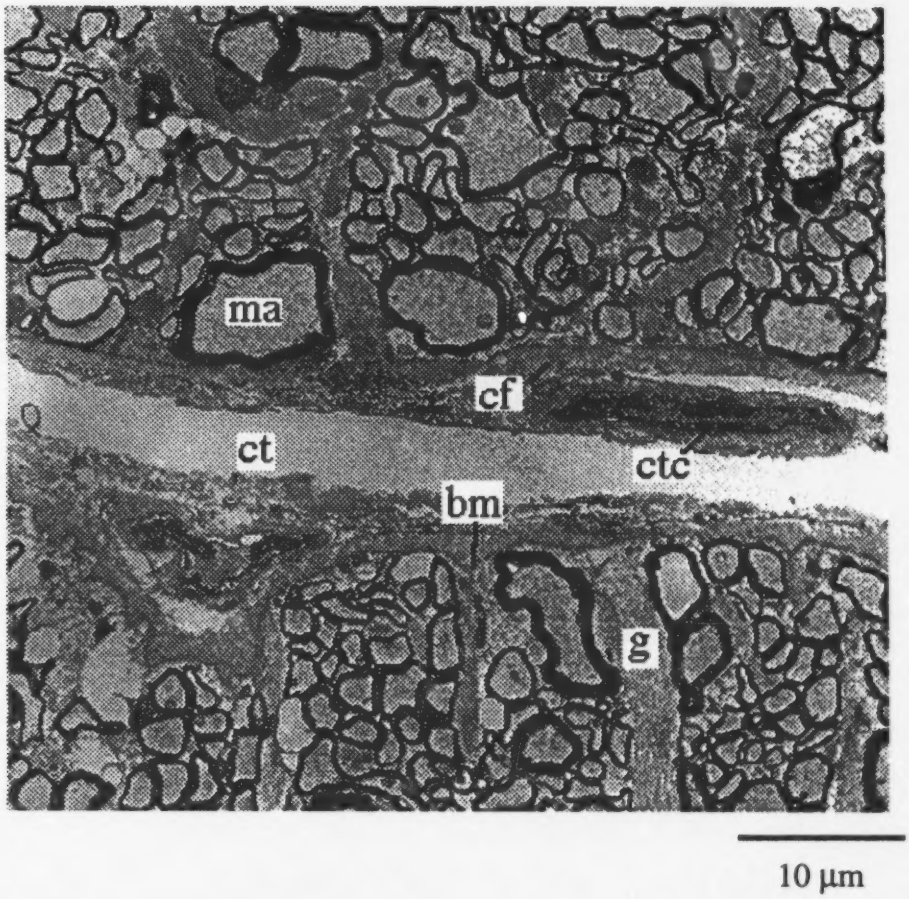

Figure 3.4(c) Connective tissue channel (ct) of the optic nerve. Dense collagen fibrils (cf) embedded in the connective tissue matrix border the axon field, composed of myelinated axons (ma) and glial cell cytoplasm (g). A basement membrane (bm) separates the connective tissue space from the glial cell cytoplasm. Connective tissue cells (ctc) and their flattened cytoplasmic processes are dispersed along the connective tissue channel.

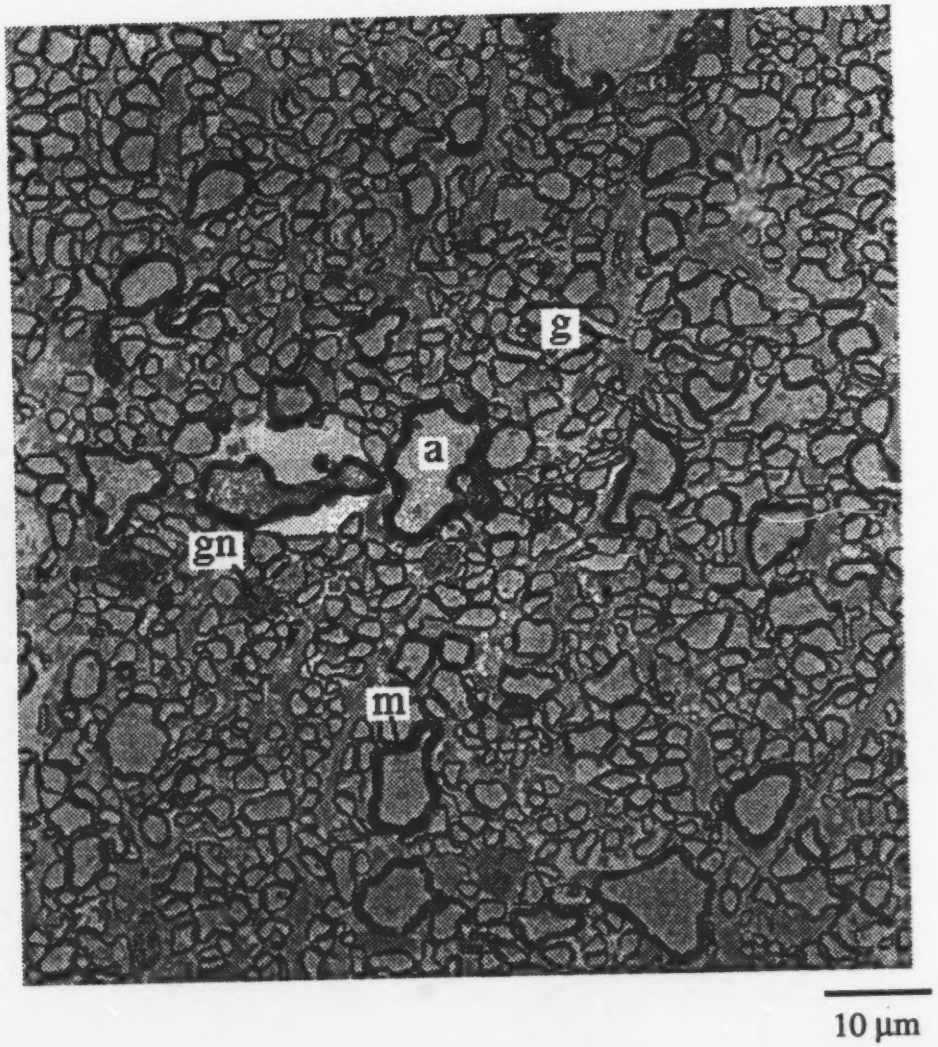

Figure 3.4(d) Axon field of optic nerve. All axons (a) are wrapped with myelin (m). Interspersed between the myelinated axons is glial cell cytoplasm (g). Within this cytoplasm, glial cell nuclei (gn) can be distinguished. The most dense of these may be oligodendrocyte nuclei. Oligodendrocytes are the glial cells which myelinated the axons, however, they are not seen associated with the myelin because one oligodendrocyte myelinates many axons.

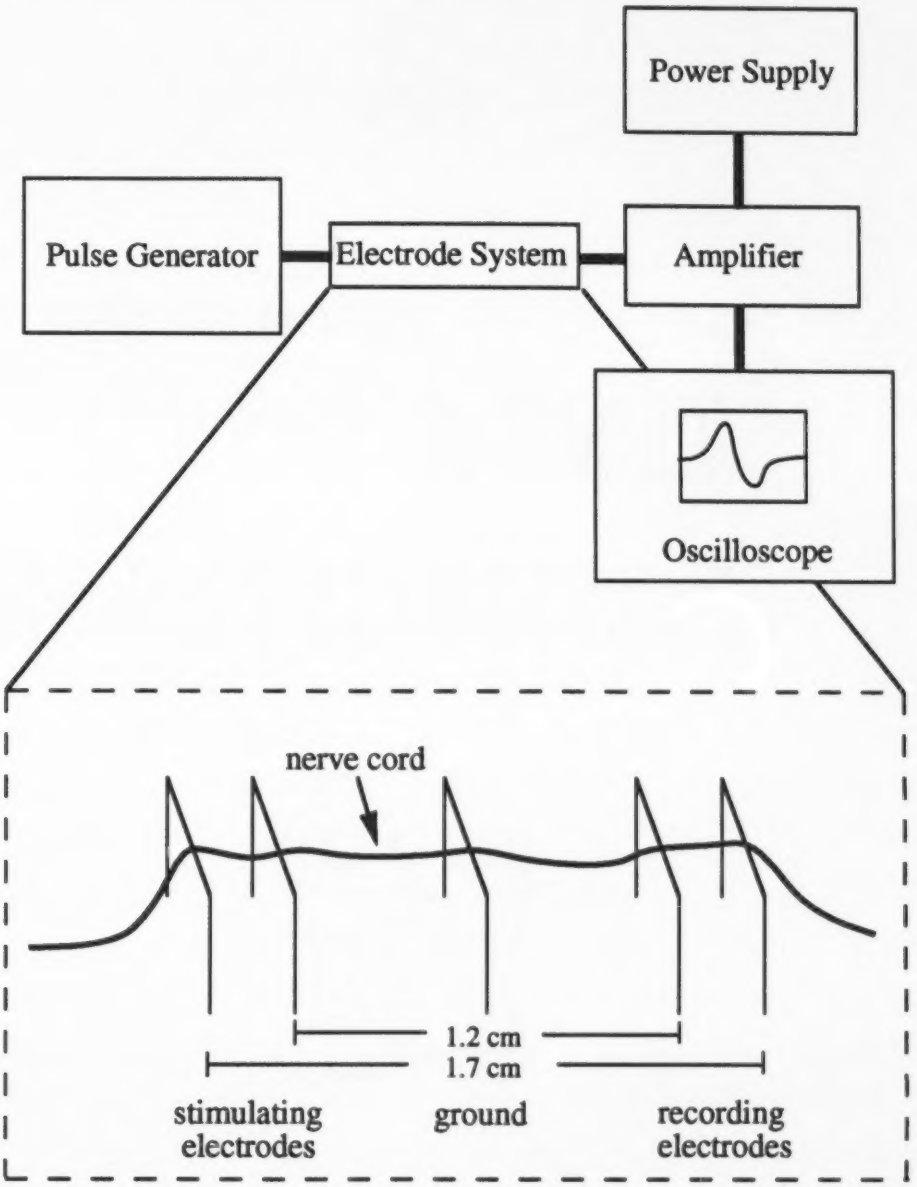

Figure 3.5 Block diagram of biphasic stimulating and recording electrode system used for measuring action potentials in nerves.

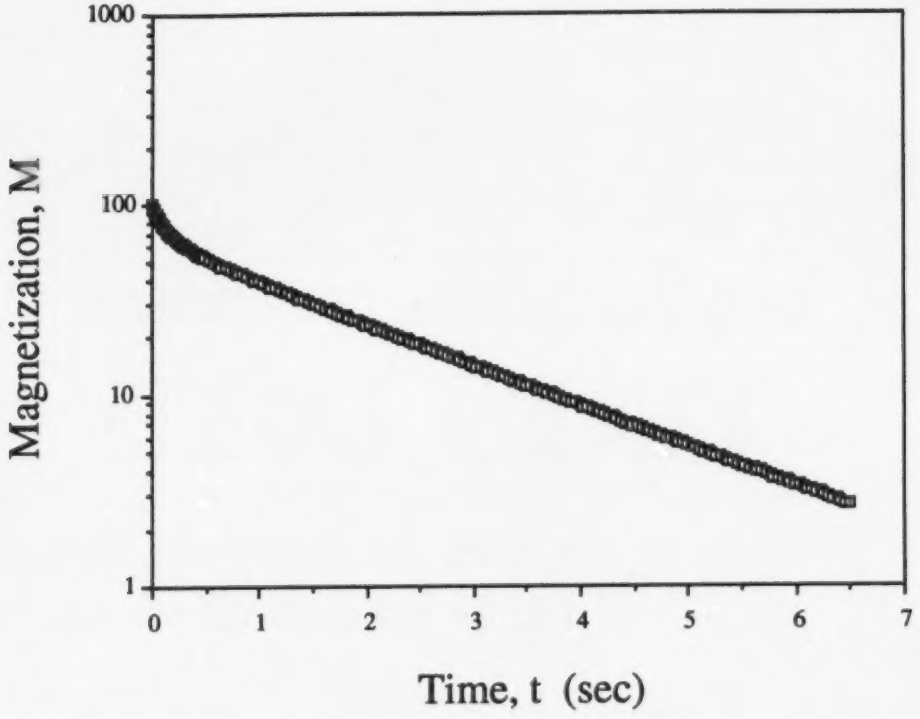

Figure 3.6 Transverse magnetization decay from a typical T_2 experiment. Note the multiexponentiality of the decay as well as the high signal to noise ratio.

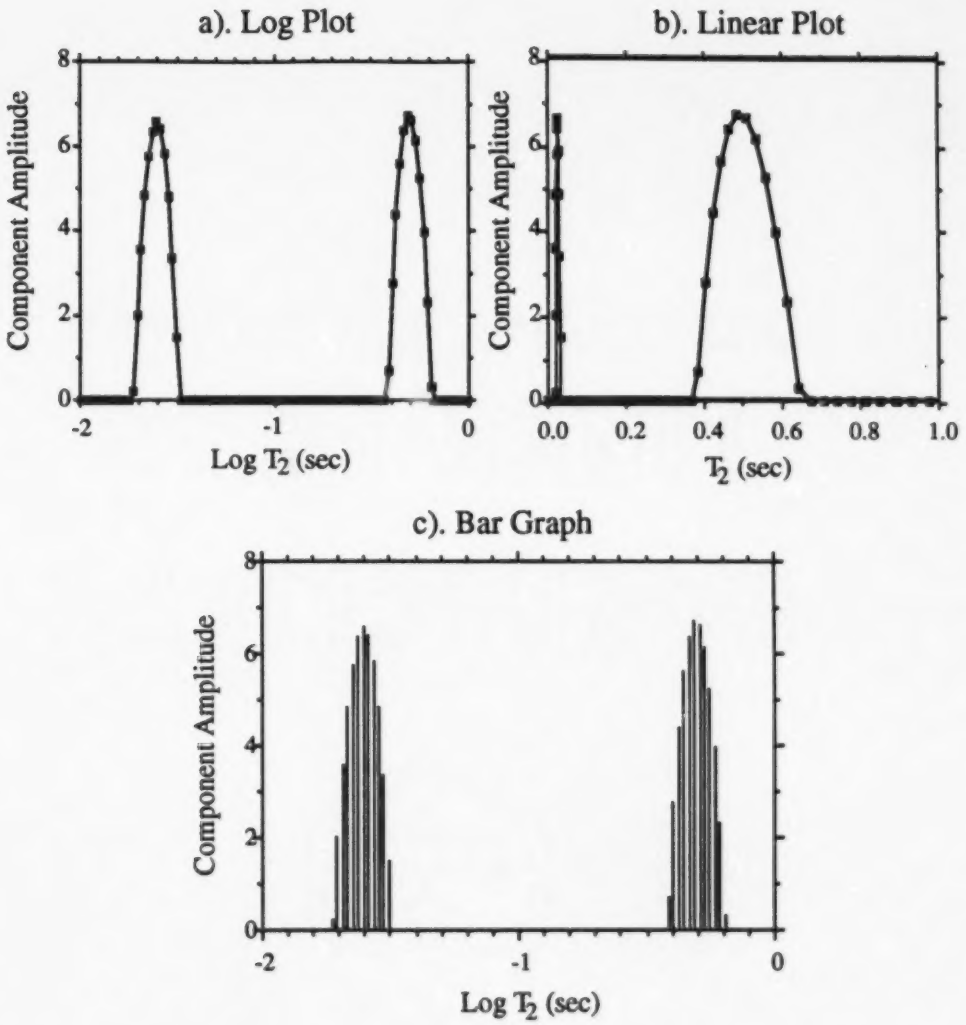

Figure 3.7 Sample T2LIN spectra, consisting of two equal amplitude components, plotted **a)** as a line graph on a log scale, **b)** as a line graph on a linear scale, and **c)** as a bar graph on a log scale. These three plots illustrate different methods of presenting T2LIN spectra. Since the amplitude of each component is given by the sum of the amplitudes of the individual points making up that component, the best method of presentation is the bar graph. The line graphs lead one to assume that the area under the spectral curve represents the component amplitude which is an incorrect assumption.

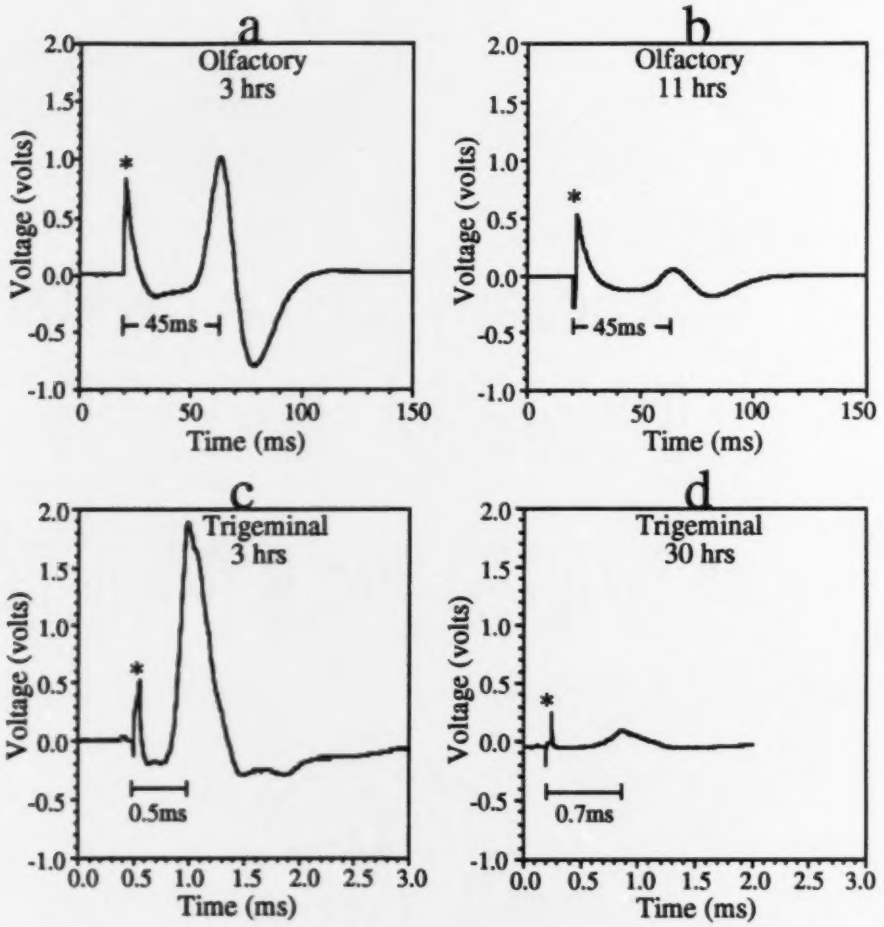

Figure 3.8 Action potential voltage measurements for the olfactory nerve at **a)** 3 hours, **b)** 11 hours and for the trigeminal nerve at **c)** 3 hours, **d)** 30 hours. The initial peak in each plot, denoted by *, is an artifact of the stimulation pulse. The time interval from this artifact to the first action potential peak represents the time for the action potential to be transmitted from the stimulating to the recording electrode. Note that the time for transmission is approximately two orders of magnitude greater in the olfactory which is consistent with the slower conduction velocity of the olfactory nerve.

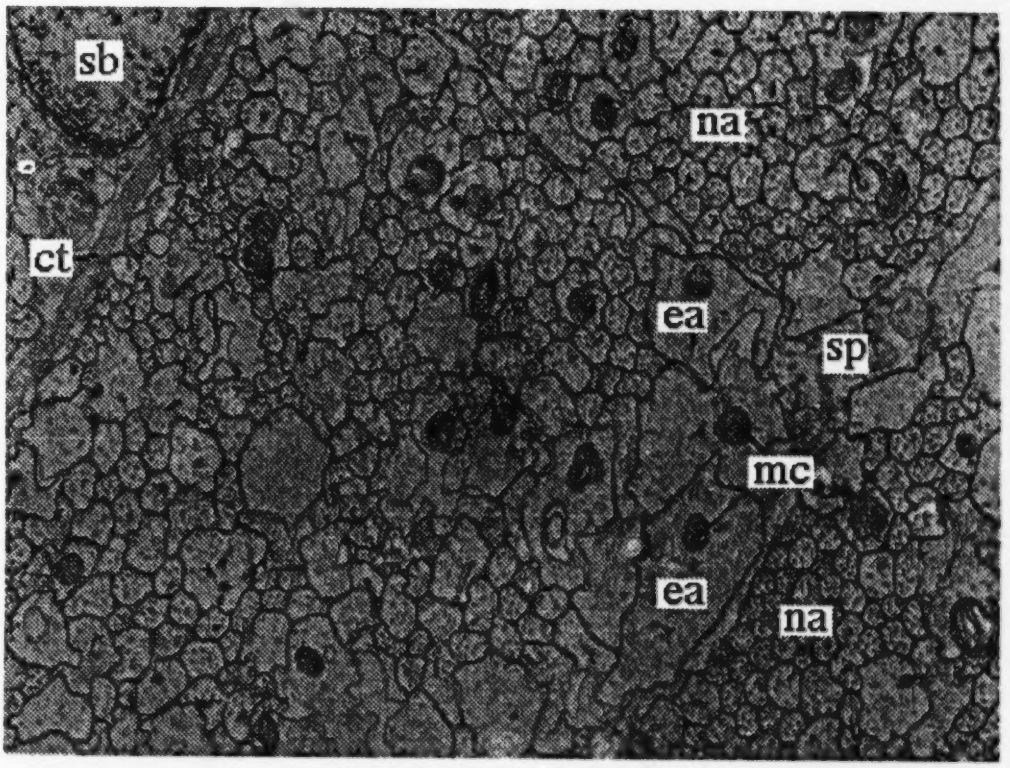

Figure 3.9(a) EM of olfactory nerve fixed at 1 hour post excision. Individual axons are easily seen in this photograph. The majority have normal size and structure (na), while a few axons have become enlarged and irregularly shaped (ea). In the enlarged axons, mitocondria (mc) are still visible but few neurofilaments and microtubules are present. Also visible in this EM are a Schwann cell body (sb), Schwann cell process (sp) and a narrow connective tissue channel (ct).

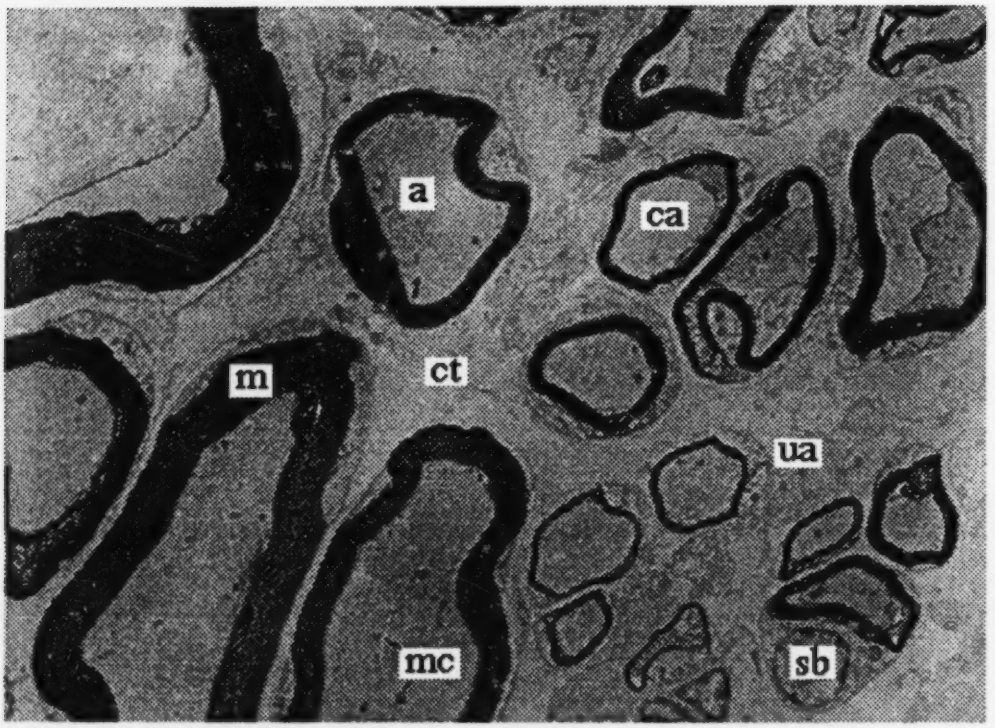

Figure 3.9(b) EM of trigeminal nerve fixed at 2 hours post excision. Myelin (m) and most of the axons (a) are intact. A few axons (ca) have contracted away from the myelin. Mitochondria (mc) are disinguishable within the axoplasm of most axons. Visible within the connective tissue space (ct) are unmyelinated axons (ua) and Schwann cell bodies (scb).

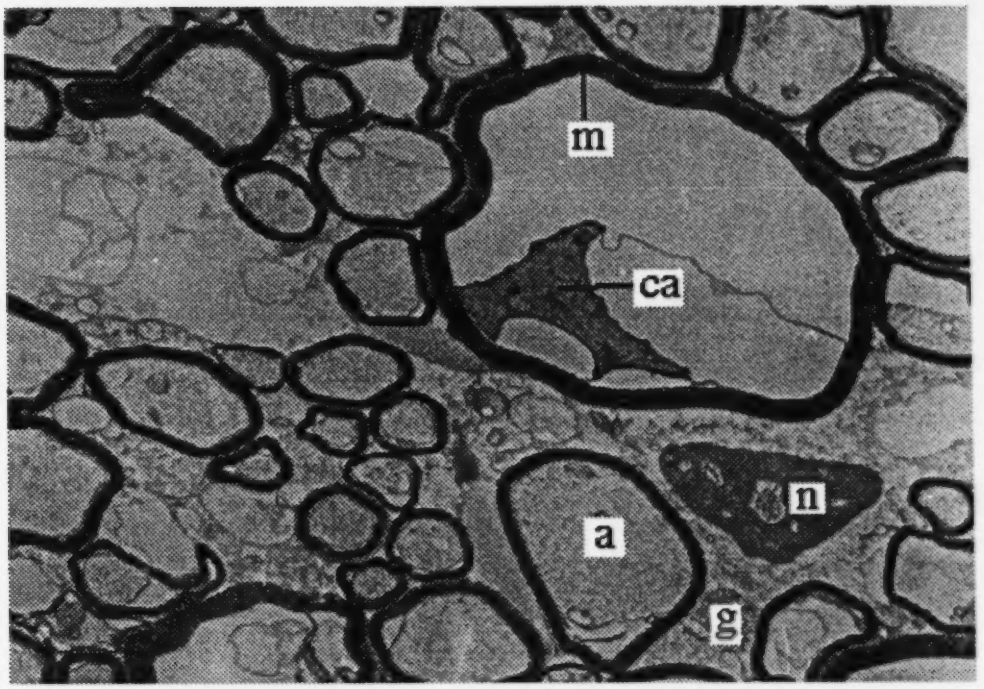

Figure 3.9(c) EM of optic nerve fixed at 2 hours post excision. Most of the myelin (m) and axons (a) appear to be intact, however, some axons have collapsed (ca). Within the glial cell cytoplasm (g) surrounding the myelinated axons, a glial cell nucleus (n) is visible.

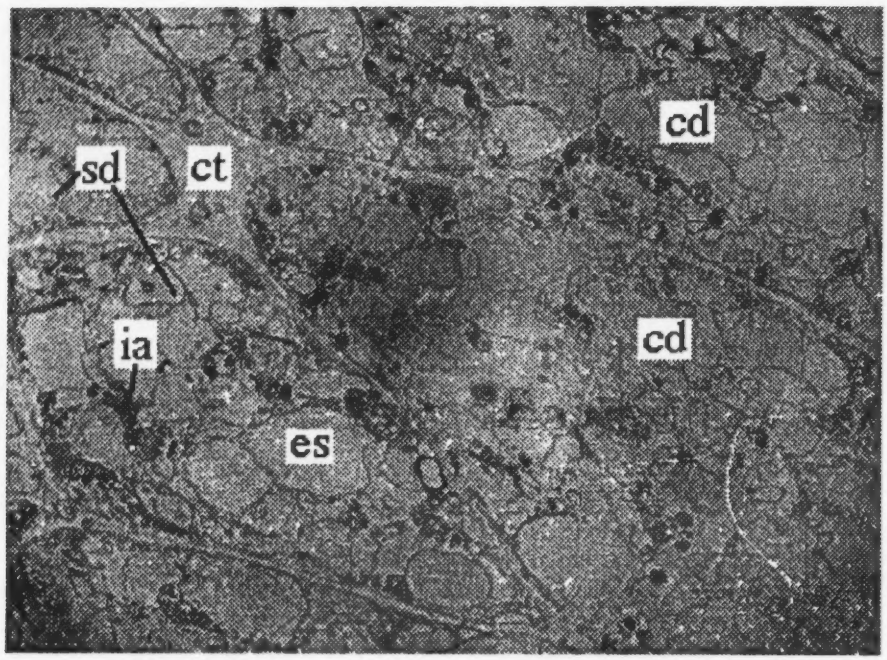

Figure 3.10(a) EM of olfactory nerve section at 8 hours post excision. The Schwann cell domains (sd) are still intact and separated by connective tissue (ct), however, very few intact axons (ia) remain. Most of the domain is filled with cellular debris (cd) amidst large empty spaces (es) formed by the expansion and breakdown of the axons.

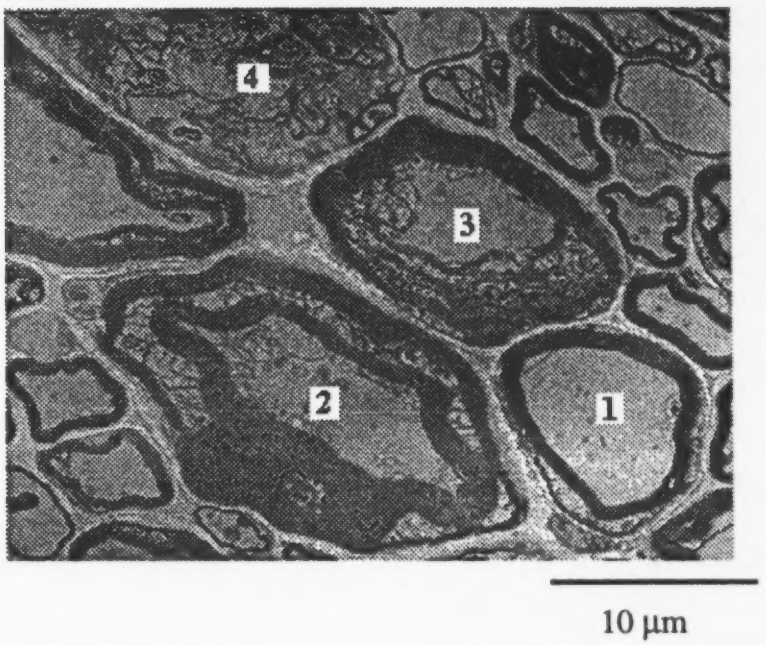

Figure 3.10(b) EM of trigeminal nerve at 8 hours post excision. Note that the controls for this nerve showed degeneration as well, and therefore conclusions about the general state of the trigemianl nerve at 8 hours cannot be made. This EM emphasizes the different stages of myelin degeneration which may occur upon excision of the nerve. The stages are numbered from 1 (normal mylinated axon) to 4 (advanced degeneration). At stage 2 the axonal membrane begins to break away from the myelin and contracts inwards as myelin layers begin to separate. At stage 3, the myelin layers continue to separate and expand inward to fill the axonal space. Finally, by stage 4, the degenerated myelin completely fills the axonal space.

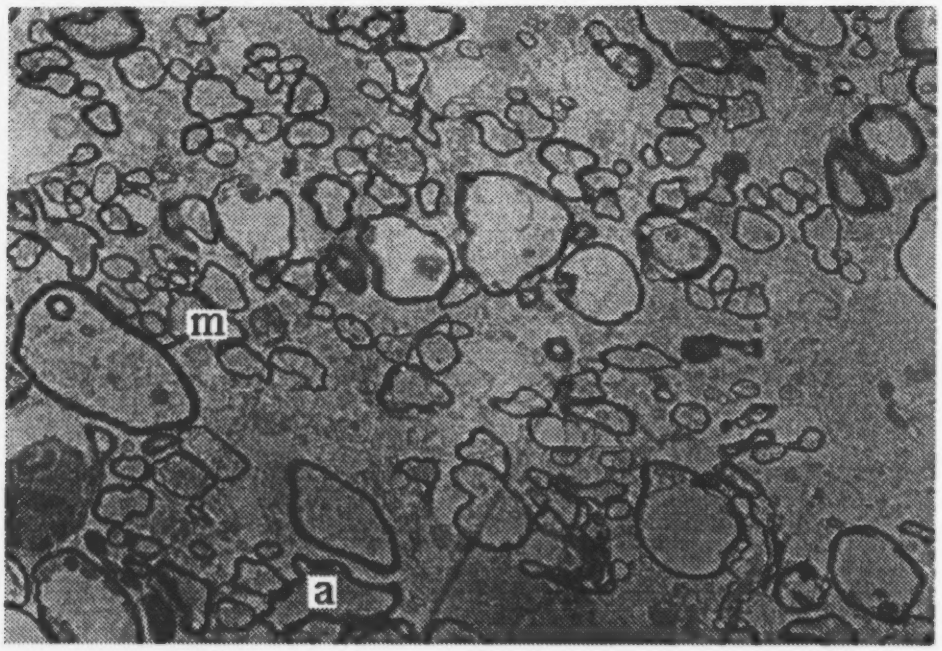

Figure 3.10(c) EM of optic nerve fixed at 8 hours post excision. Like the trigeminal nerve of Fig. 3.10(b), the controls for this optic nerve showed a very degenerate state with a sparse population of thinly myelinated axons. This EM shows a similar degenerated state. Very few axons (a) appear to be intact. Some myelin (m) does appear normal but the population of mylinated axons is much less than normal (see Fig. 3.4(a)).

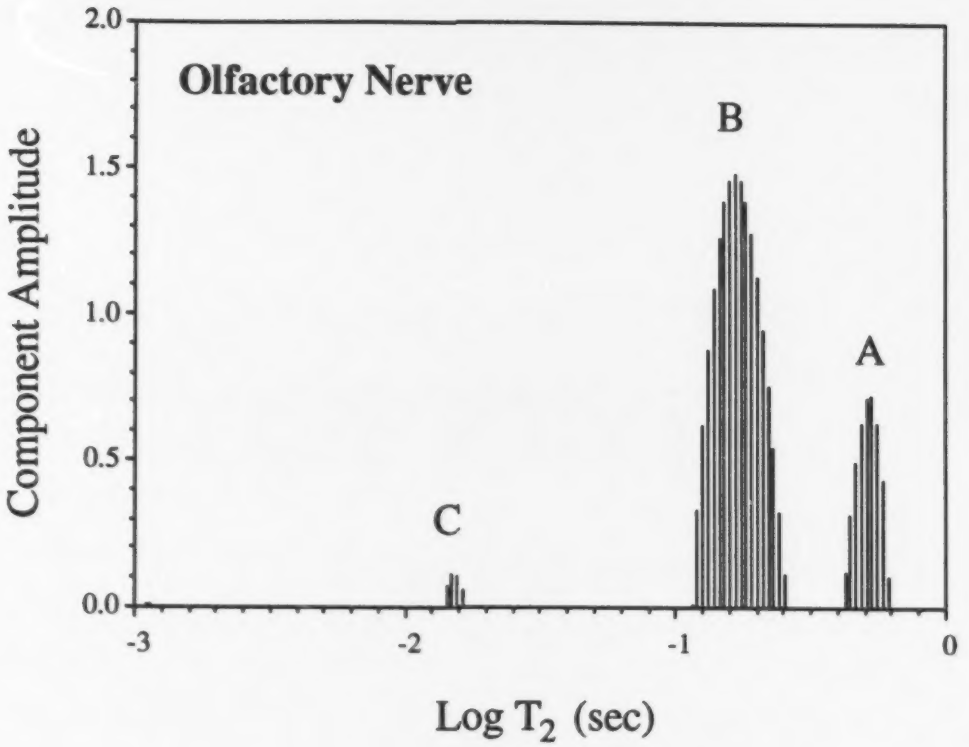

Figure 3.11(a) Typical olfactory nerve T_2 spectrum.

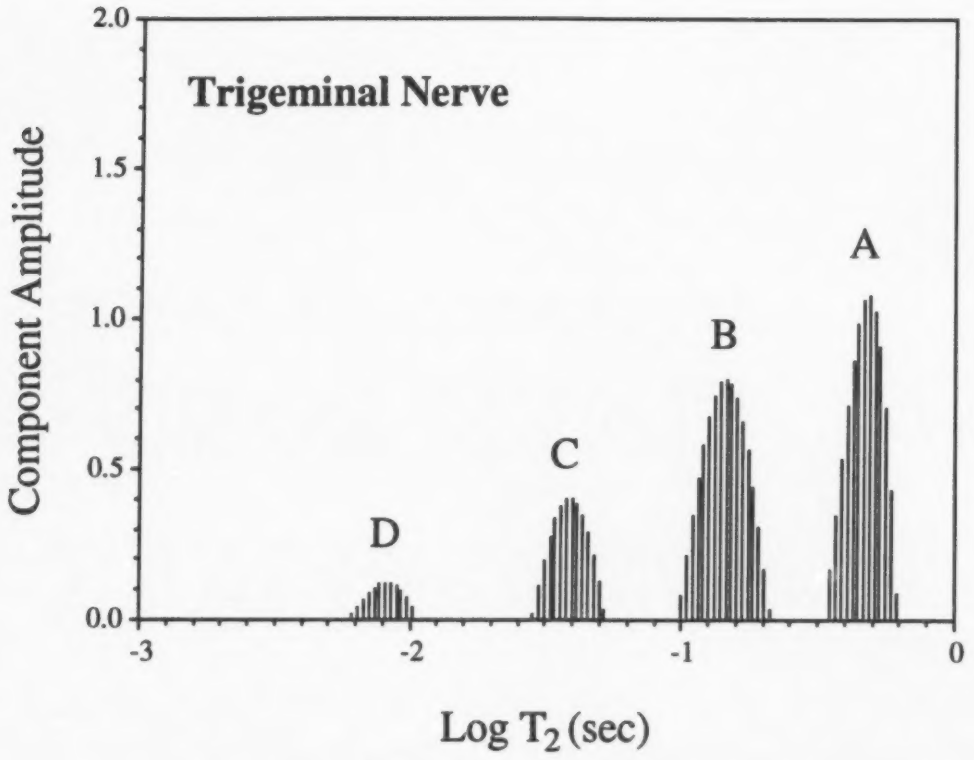

Figure 3.11(b) Typical trigeminal nerve T_2 spectrum.

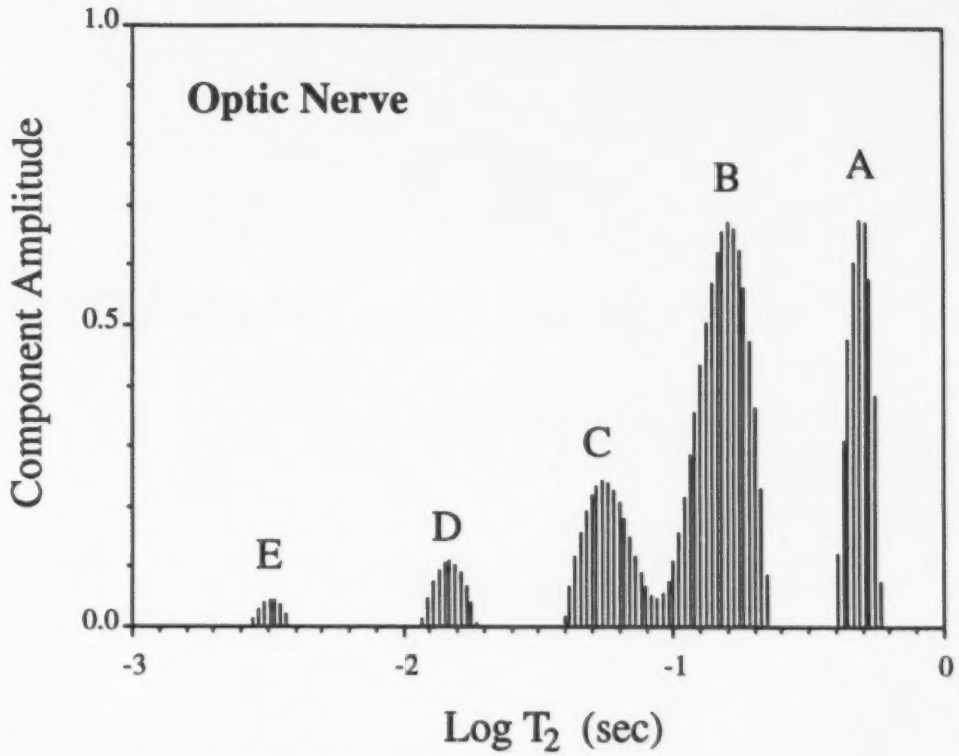

Figure 3.11(c) Typical optic nerve T_2 spectrum.

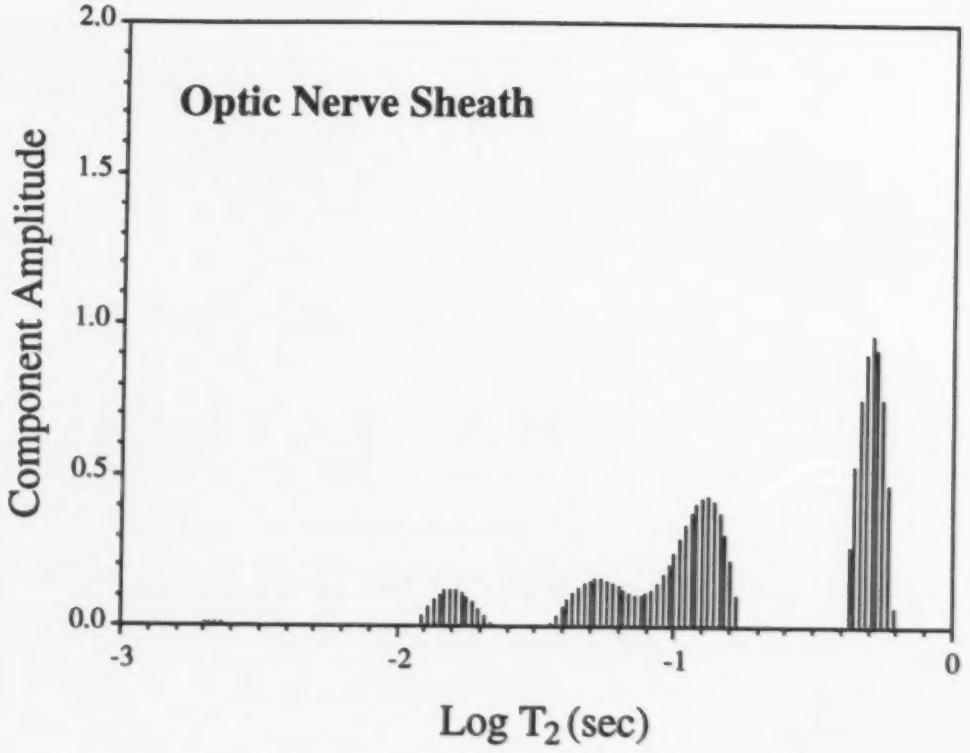

Figure 3.12 T_2 spectrum of optic nerve sheath.

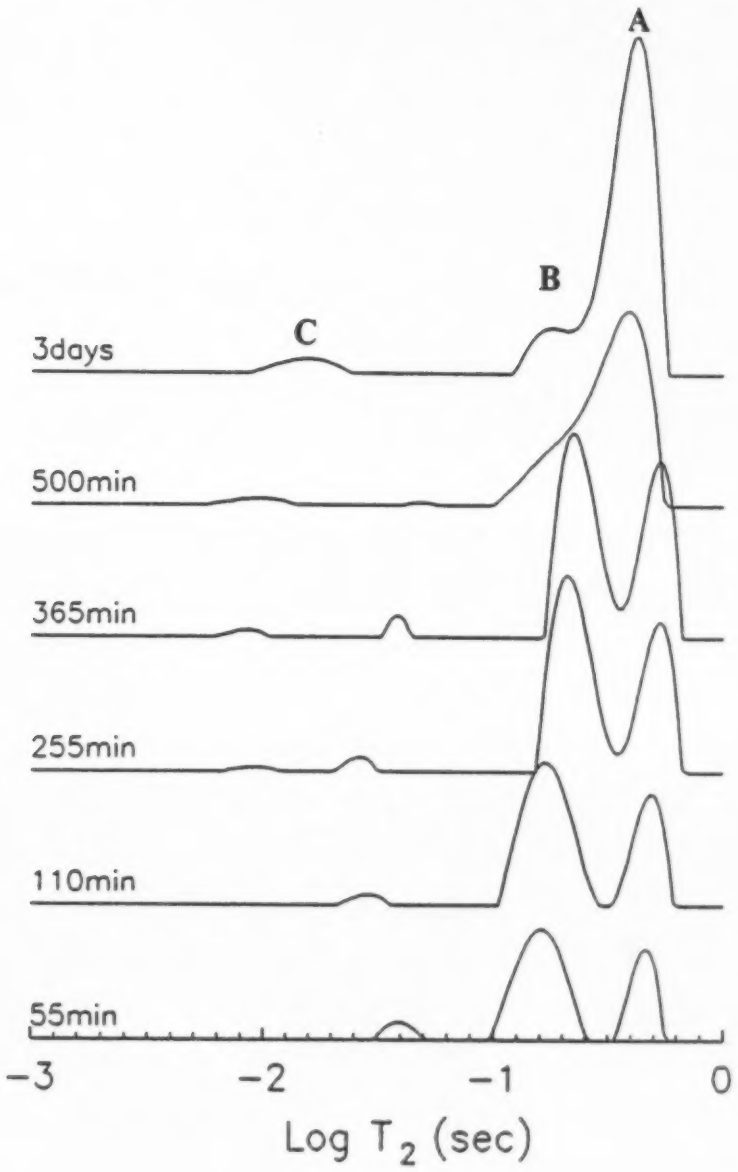

Figure 3.13(a) Time variation of the olfatory nerve T2 spectra over a period of 3 days. Note the convergence of components A and B.

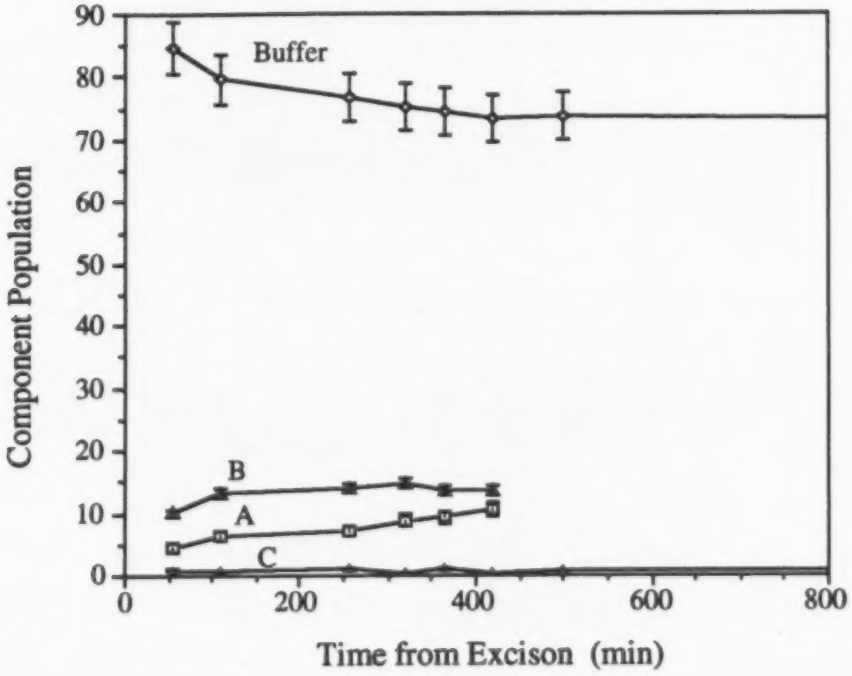

Figure 3.13(b) Olfactory nerve population versus time graph corresponding to the stackplot of Fig. 3.13(a).

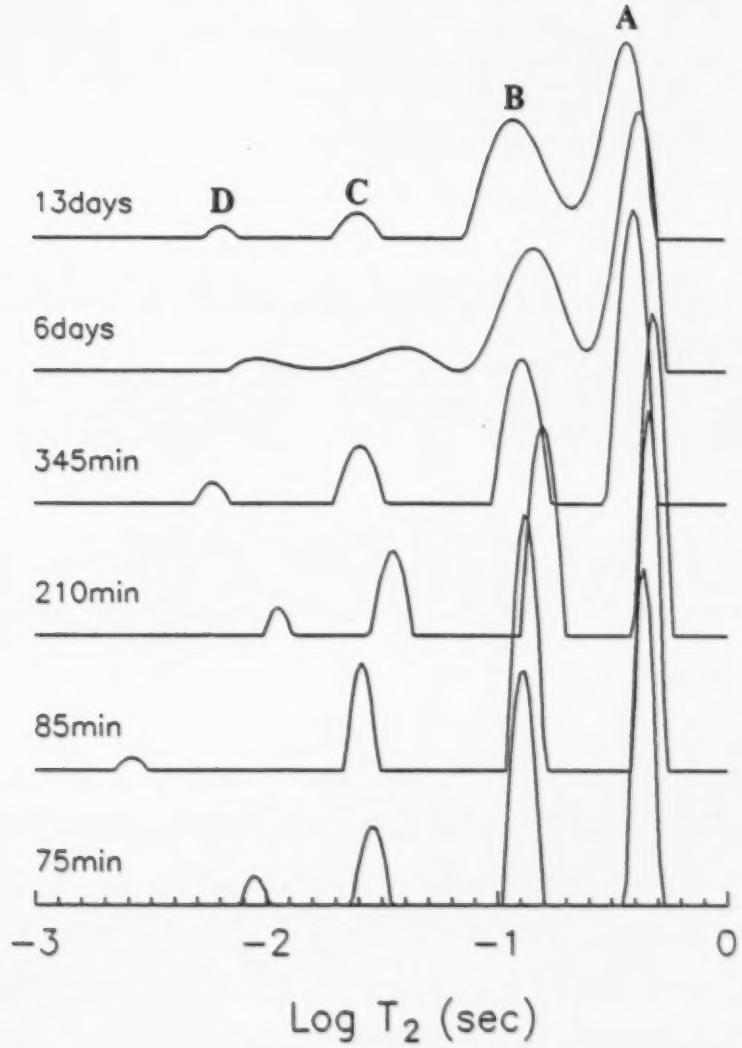

Figure 3.14(a) Time variation of the trigeminal nerve T2 spectra over a period of 13 days. Unlike the olfactory nerve, Fig. 3.13(a), components A and B of the myelinated trigeminal do not converge even at times as long as 13 days. This is attributed to the slow breakdown of the myelin. Component C which is attributed to myelin water shows a noticeable decrease in amplitude which may indicate a breakdown in some of the myelin.

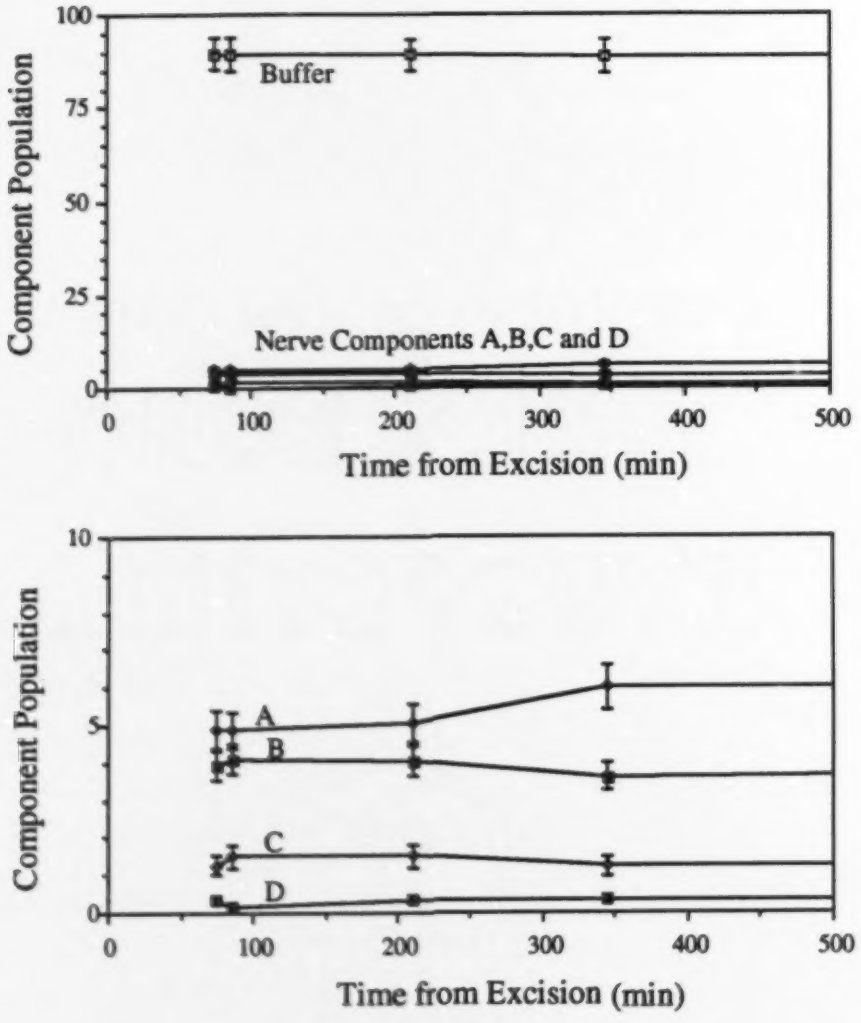

Figure 3.14(b) Trigeminal nerve population versus time graphs corresponding to the stackplot of Fig. 3.14(a). Two plots covering different ranges of population are shown to illustrate the variations in populations for the buffer as well as the nerve components.

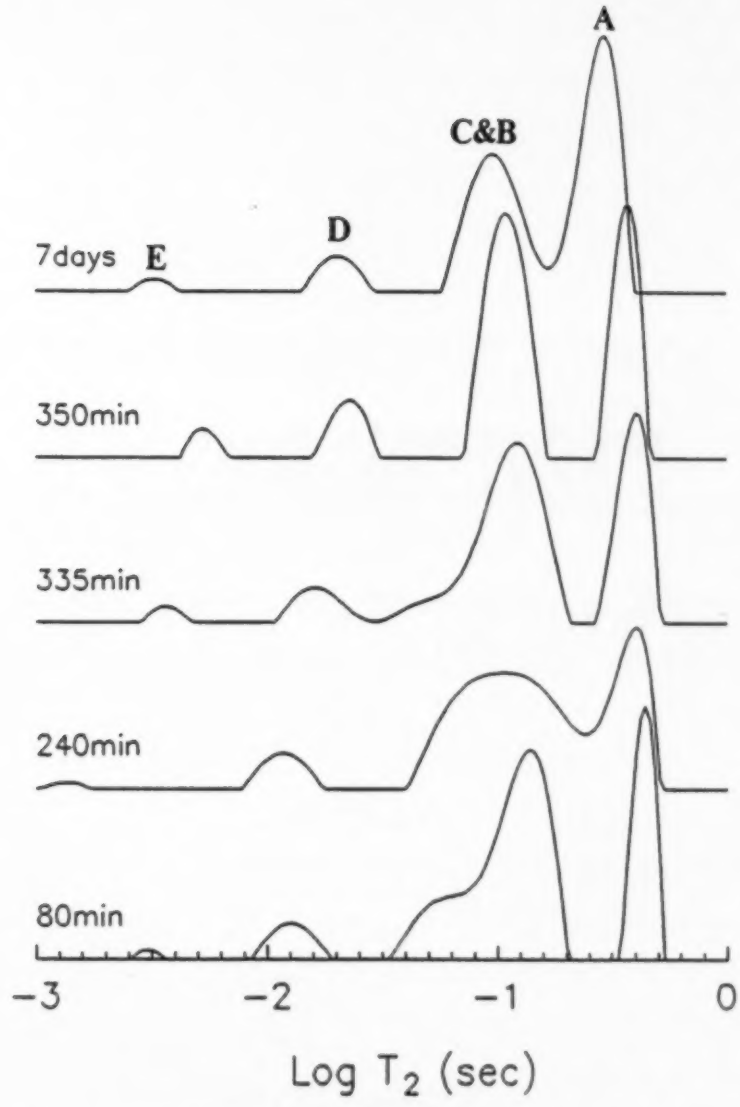

Figure 3.15(a) Time variation of the optic nerve T2 spectra over a period of 7 days. As seen in the trigeminal nerve, Fig. 3.14(a), components A and B of the optic nerve do not converge in a time period of 7 days. This is attributed to the presence of myelin in the optic nerve. Component C, attributed to myelin, is only partially resolved at 80min, and thereafter is not resolved at all. This may be a due to the fact that optic nerves have thinner myelin sheaths than those present in the trigeminal nerve, and therefore faster exchange between axonal, myelin and glial cell water.

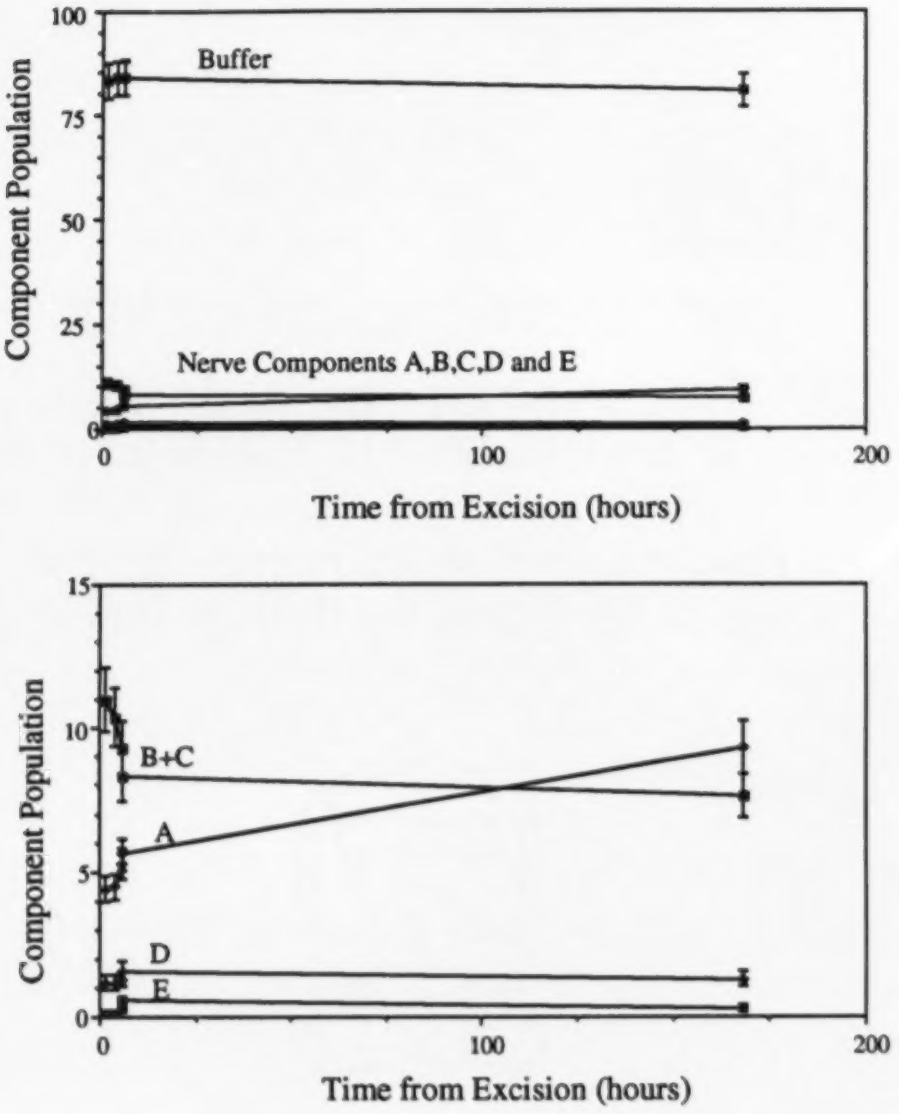

Figure 3.15(b) Optic nerve populations versus time graphs corresponding to the stackplot of Fig. 3.15(a). Two plots covering different ranges of population are shown to illustrate the variations in populations for the buffer as well as the nerve components.

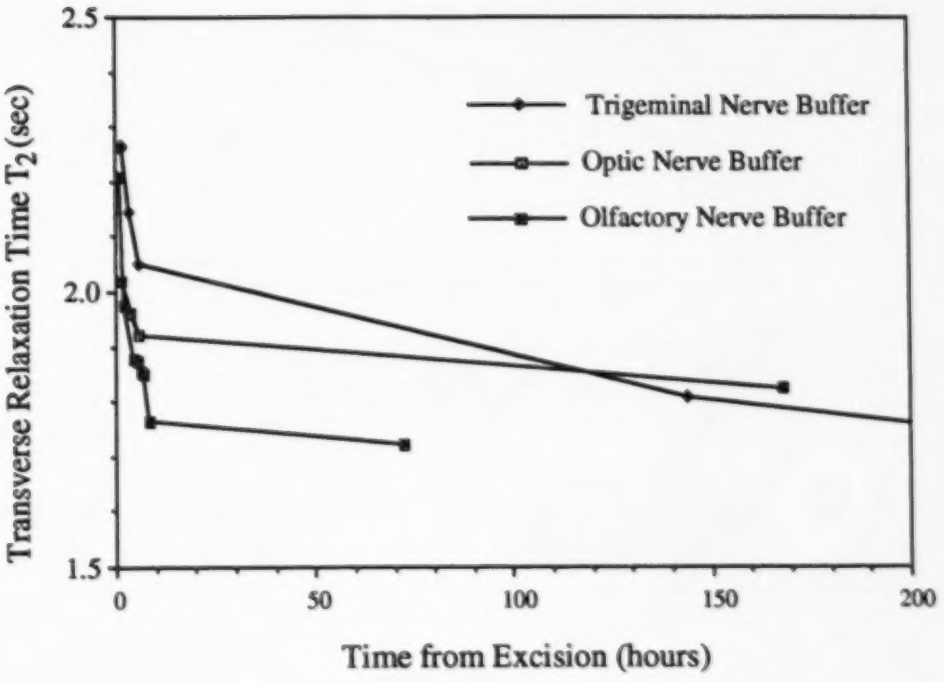

Figure 3.16 Variation of buffer solution T_2 as a funcion of time from excision for all nerve types.

3.9 References and Selected Bibliography

1. R. S. Menon, M. S. Rusinko, and P. S. Allen, Multiexponential proton relaxation in a model cellular system, *Magn. Reson. Med.* **20**(2), 196 (1991).

2. R. S. Menon, M. S. Rusinko, and P. S. Allen, Proton relaxation studies of water compartmentalization in a model neurological system, *Magn. Reson. Med.* in press.

3. V. Vasilescu, Eva Katona, V. Simplaceanu, and D. Demco, Water compartments in the myelinated nerve. III. Pulsed NMR results. *Experientia* **34**, 1443 (1978).

4. R. S. Menon and P. S. Allen, Application of continuous relaxation time distributions to the fitting of data from model systems and excised tissue, *Magn. Reson. Med.* **20**(2), 214 (1991).

5. W. A. Stewart, K. P. Whittall, D. W. Paty, Analysis of CPMG data from CNS tissue: a potential method for detecting demyelination in Multiple Sclerosis, 10th SMRM, 85, (1991).

6. A. L. MacKay, K. P. Whittall, K. S. Cover, D. K. B. Li, D. W. Paty, Invivo T_2 relaxation measurements of brain may provide myelin concentration, 10th SMRM, 917, (1991).

7. D. S. Lee et al., "Atlas of North American Freshwater Fishes", North Carolina Biological Survey, pg. 48 (1980).

8. D. M. Easton, Garfish olfactory nerve: easily accessible source of numerous long, homogeneous, nonmyelinated axons, *Science* **172**, 952 (1971).

9. J. B. Holton and D. M. Easton, Major lipids of non-myelinated (olfactory) and myelinated (trigeminal) nerve of garfish, Lepisosteus osseus, *Biochim. Biophys. Acta.* **239**, 61 (1971).

10. P. Cancalon, Proximodistal degeneration of C-fibres detached from their perikarya, *J. Cell Biol.* **97**, 6 (1983).

11. P. Cancalon, Axonal transport in the garfish optic nerve: comparison with the olfactory system, *J. Neurochem.* **51**, 266 (1988).

12. D. M. Easton, Impulses at the artifactual nerve end, *Cold Spring Harbor Symp. Quant. Biol.* **30**, 15 (1965).

13. F. A. Jolesz, J. F. Polak, D. F. Adams, P. W. Ruenzel. Myelinated and nonmyelinated nerves: comparison of proton MR properties *Radiology* **164**, 89 (1987).

14. G. A. Hansen, ed., "Connective Tissue in Health and Disease", Ejnar Munksgaard Publisher, Copenhagen, pg. 25 (1954).

15. D. C. Chang, and C. F. Hazlewood, A nuclear magnetic resonance study of squid giant axon, *Bioch. Biophys. Acta* **630**, 131 (1980).

16. S. H. Koenig, R. D. Brown, M. Spiller, and N. Lundbom, Relaxometry of brain: why white matter appears bright in MRI, *Magn. Res. Med.* **14**, 482 (1990).

17. A. Finkelstein, "Water Movement Through Lipid Bilayers, Pores, and Plasma Membranes: Theory and Reality", Wiley, New York, (1987).

18. H. Y. Carr and E. M. Purcell, Effects of diffusion on free precession in nuclear magnetic resonance experiments, *Phys. Rev.* **94**, 630 (1954).

19. S. Meiboom and D. Gill, Modified spin-echo method for measuring nuclear relaxation times, *Rev. Sci. Instrum.* **29**, 688 (1958).

20. D. G. Hughes and L. Lindblom, Baseline drift in the Carr-Purcell-Meiboom-Gill pulsed NMR experiment, *J. Magn. Reson.* **26**, 469 (1977).

21. C. L. Lawson and R. J. Hanson, "Solving Least Squares Problems", Prentice-Hall, Englewood Cliffs N.J., (1974).

22. K. P. Whittall and A. L. Mackay, Quantitative interpretation of NMR relaxation data, *J. Magn. Reson.* **84**, 134 (1989).

23. D. A. Hill and M. N. Sherebrin, *Can. J. Physiol. Pharmacol.* **54**, 485 (1976).

24. W. F. Ganong, "Review of Medical Physiology", 14th ed., Appleton and Lange, Norwalk, Connecticut, pg. 47 (1989).

25. S. Peto and P. Gillis, Fiber-to field angle dependence of proton nuclear magnetic relaxation in collagen, *Magn. Reson. Imag.* **8**, 705, (1990).

26. R. R. Myers, H. M. Heckman and H. C. Powell, Endoneurial fluid is hypertonic, *J. Neuropath. and Exp. Neurol.* **42**, 217 (1983).

27. H. C. Powell and M. L. Costello, Endoneurial fluid pressure in Wallerian degeneration, *Annals of Neurol.* **5**, 550 (1978).

28. W. T. Norton in "The Nervous System", D. B. Tower, ed., Raven Press, New York, vol.1, pg. 467, (1975).

29. D. A. Kirschner, A. L. Gansen, D. L. D. Caspar, Diffraction studies of molecular organization and membrane interactions in Myelin, in "Myelin", 2nd ed., P. Morell ed., Plenum Press, New York, pg. 74, (1974).

30. A. Ruggeri and P. M. Motta, eds. "Ultrastructure of the Connective Tissue", Martinus Nijhoff Publishers, Boston, pg. 39, (1984).

31. H. W. Fischer, Y. V. Haverbeke, I. Schmitz-Feuerhake, and R. N. Muller, The uncommon longitudinal relaxation dispersion of human brain white matter, *Magn. Reson. Med.* **9**, 441 (1989).

Chapter 4

Conclusion

4.1 Discussion and Conclusions

The goal of this thesis was two-fold: first, to evaluate the capabilities of an algorithm, T2LIN, for calculating the continuous multi-component transverse relaxation time distributions under in-vivo and in-vitro experimental conditions; and second to determine if the multiple transverse relaxation time components of myelinated and nonmyelinated cranial nerves can be identified with water protons in specific anatomical compartments, the most important of these being the myelin compartment.

In Chapter 2, the first of these goals was achieved through a computer simulation study of T2LIN. The effects of limitations in experimental NMR variables such as SNR, data acquisition windows, and number of data points, were evaluated. It was found that SNR was the greatest limiting factor for the resolution of multiple Gaussian relaxation time components. As an example, a SNR of 100 can resolve at best two peaks separated by a factor of ~6. To decrease this factor to ~2 the SNR must be increased to ~2000. Decreasing the number of data points did not have a major effect upon the T2LIN spectra, with 16 data points being the minimum acceptable, since any fewer than this had a tendency to cause the T2LIN algorithm to break down. However, accompanying the decrease in the number of data points was a noticeable increase in T2LIN's sensitivity to differences in the noise representations. This is an important point which has been overlooked in previous evaluations of linear inverse techniques (1,2,3). Finally, the simulation tests limiting the data acquisition window as a function of SNR indicated that a minimum data window edge positioned at half the relaxation time of the shortest component and a maximum data window edge positioned at twice the relaxation time of the longest component yielded the best possible spectra attainable at a given SNR. An expansion of this data time window did not yield any significant improvement in component precision, while a contraction reduced precision. In this final simulation test it was also found that SNR had a major effect upon component precision. As the SNR decreased component precision decreased as well. The results of this simulation study provided the justification for the quantitative interpretations made on the transverse relaxation time spectra measured in Chapter 3.

In Chapter 3, the measurements of the multi-component transverse relaxation characteristics of a white matter tissue model are reported. The white matter model chosen consisted of both myelinated and nonmyelinated cranial nerves of the spotted garfish. The in-vitro measurements of the multiexponential transverse magnetization decay of water protons in these nerves provided a data base for T2LIN which, based on the results reported in Chapter 2, clearly had very few experimental limitations. The SNR was typically around 3000 with no significant restrictions in the data acquisition window nor the number of data points. Utilizing the results of the simulation tests of T2LIN, confidence was gained in the resulting continuous transverse relaxation time distributions. The reproducibility of component relaxation times and amplitudes added further support to the results.

The most convincing result supporting the assignment of the myelin water was the fact that the short T_2 component, identified as myelin water, was only present in the T_2 spectra of both myelinated nerves. It was not seen in the nonmyelinated nerve. The assignments were achieved primarily through comparisons of the NMR component populations to populations derived from EM and optical microscopy. The assignments were further supported by time course measurements of the transverse relaxation times which highlighted the differential sensitivity of transverse relaxation components to the physiological state of the tissue. The other water compartments which were successfully identified were the connective tissue spaces, intracellular and axonal water.

Together, the results of Chapters 2 and 3 can provide valuable insights into the potential use of the multi-component transverse relaxation time analysis in-vivo. The multi-component nature of transverse relaxation in a white matter tissue model reported in Chapter 3 can be used as an indicator for the characteristics of water in white matter in-vivo. As in the nerve, the exchange of water across white matter myelin should be slow enough to yield a separate slow transverse relaxation time component for myelin. However, the exchange across single cellular membranes is fast, and therefore the extracellular spaces and glial cell cytoplasm external to myelin will constitute a single component. The similarity of the axoplasm's transverse relaxation time to that of the extra-myelinic compartment should render these two compartments indistinguishable and therefore white matter will have a transverse relaxation time distribution consisting of a short myelin component and a long component corresponding predominantly to intracellular water. This type of transverse relaxation time distribution has been seen in-vitro in cat (4) and guinea pig (5) white matter as well as in-vivo in human white matter (6).

The T_2 spectra of the nerves also showed sensitivity to physiological change, however, such changes are very different from the type of degeneration which occurs in-vivo during disease. Nevertheless, the T_2 distributions corresponding to in-vivo white matter should be sensitive to the pathophysiological changes brought about by disease. For example, in the demyelinating disease Multiple Sclerosis, myelin breaks down and is removed by surrounding glial cells while the axon remains intact. Such a diseased state should be characterized by a decrease or complete loss of the short relaxation time component corresponding to myelin. This is in fact the situation documented in a recent in-vivo transverse relaxation time study done on Multiple Sclerosis patients (6). Edema is another example and one in which fluid accumulates either in the extracellular (vasogenic edema) or intracellular spaces (cytotoxic edema) of the white matter. In this pathological state, the T_2 spectra may show an extra long time component corresponding to the extracellular fluid accumulation. Some in-vivo measurements of transverse relaxation on animal models have shown the emergence of a long time component in edematous white matter (7,8). However, since intra- and extracellular spaces are indistinguishable in the normal state, vasogenic and cytotoxic edema will be difficult to distinguish.

Although the results of the in-vitro study of Chapter 3 show promise for the use of transverse relaxation in-vivo, the results of Chapter 2 bring to light the limitations encountered in the in-vivo experiment, limitations which will have a profound effect upon the usefulness of this technique in-vivo. The dominant limiting factor is the decreased SNR achievable in-vivo. It is typically on the order of 100, only allowing T2LIN to distinguish components separated in time by a minimum factor of ~6. In white matter in-vivo, it will therefore be very difficult to distinguish myelin from intracellular water since their relaxation times are at most a factor of 4 apart. In the T_2 study of MS patients (6) discrete rather than a continuous distribution analysis was used, the discrete analysis resolves components at lower SNRs, but the solutions are very susceptible to noise errors and confidence can only be gained through reproducibility. Another limiting factor in-vivo, which is not as significant as SNR but which may still have some adverse effects, is the position in time of the minimum edge of the data window. Currently, in imaging this minimum edge is typically around 20ms therefore allowing only peaks at 40ms and greater to be successfully identified. With these current limitations of the in-vivo experiment, it is clear that not only must SNRs be improved but eddy current limitations on the minimum echo times must also be removed before the continuous multi-component relaxation technique will find routine application

in the diagnosis of diseases in white matter as well as other tissues. Thus the task remains to develop this technique in-vivo.

Regardless of its potential in-vivo, the continuous distribution multi-component relaxation analysis will always be useful in-vitro for improving the understanding of water proton relaxation mechanisms in biological tissues, a subject which is not fully understood. Water proton NMR relaxation affects all NMR measurements where water protons are the nuclear species of interest. Therefore, it is important to understand water proton relaxation mechanisms and know their relaxation characteristics in specific tissue types. In-vitro measurements of transverse relaxation time distributions usually provide a good first approximation to the situation in-vivo. With this thesis we have successfully improved our understanding of transverse relaxation in nerve tissue and have evaluated the potential of the transverse relaxation time analysis in-vivo. In so doing we have laid the ground work for further NMR investigation of nerve tissue both in-vitro and in-vivo.

4.2 References and Selected Bibliography

1. R. M. Kroeker and R. M. Henkelman, Analysis of biological NMR relaxation data with continuous distributions of relaxation times, *J. Magn. Reson.* **69**, 218 (1986).

2. R. J. S. Brown, Information available and unavailable from multiexponential relaxation data, *J. Magn. Reson.* **82**, 539 (1989).

3. K. P. Whittall, M. J. Bronskill, and R. M. Henkelman, Investigaiton of analysis technique for complicated NMR relaxation data, *J. Magn. Res.* **95**, 221 (1991).

4. R. S. Menon and P. S. Allen, Application of continuous relaxation time distributions to the fitting of data from model systems and excised tissue, *Magn. Reson. Med.* **20**(2), 214 (1991).

5. W. A. Stewart, K. P. Whittall, D. W. Paty, Analysis of CPMG data from CNS tissue: a potential method for detecting demyelination in Multiple Sclerosis, 10th SMRM, 85, (1991).

6. A. L. MacKay, K. P. Whittall, K. S. Cover, D. K. B. Li, D. W. Paty, Invivo T_2 relaxation measurements of brain may provide myelin concentration, 10th SMRM, 917, (1991).

7. S. Naruse, Y. Horikawa, T. Chuzo, K. Hirakawa, N. Nishikawa and K. Yoshizakai, Proton nuclear magnetic resonance studies on brain edema, *J. Neurosurg.* **56**, 747 (1982).

8. M. E. Castro, "Experimental brain edema studied with proton NMR", Ph.D. Thesis: University of Alberta (1986).